The University of Osaka
Institutional Knowledge Archive

Title	Laboratory study on outflow jet formation via semi-relativistic magnetic reconnection with high-intensity laser
Author(s)	Law, King Fai Farley
Citation	大阪大学, 2019, 博士論文
Version Type	VoR
URL	https://doi.org/10.18910/73513
rights	
Note	

The University of Osaka Institutional Knowledge Archive : OUKA

https://ir.library.osaka-u.ac.jp/

The University of Osaka

OSAKA UNIVERSITY

DOCTORAL THESIS

Laboratory study on outflow jet formation via semi-relativistic magnetic reconnection with high-intensity laser

Author:
King Fai Farley LAW

Supervisor:
Prof. Shinsuke FUJIOKA

A thesis submitted in fulfillment of the requirements for the degree of Ph.D. in Science

in the

Laser-Produced High-Field Sciences Group, Institute of Laser Engineering
International Physics Course, Department of Physics
Graduate School of Science

August 2, 2019

OSAKA UNIVERSITY

Abstract

Graduate School of Science
International Physics Course, Department of Physics

Ph.D. in Science

Laboratory study on outflow jet formation via semi-relativistic magnetic reconnection with high-intensity laser

by King Fai Farley LAW

Magnetic reconnection is a rearrangement of magnetic field topology in plasmas, also known as an energy conversion process from magnetic field energy to the kinetic energy of charged particles in the plasma. This phenomenon is accounted for a wide range of energetic astronomical phenomena, for example, solar coronal mass ejection, high energy photon emission from black hole systems and formation of stars.

The main scope of this study is on magnetic reconnection outflow from plasma in a semirelativistic magnetization regime, where the magnetic field energy density exceeds the electron rest mass density but below that of the ion. The accretion disk corona of black hole systems lies in this regime, while the mechanism behind its high energy photon emission is still unsure. One of the proposed emission mechanism is magnetic reconnection, which provides energetic particles as a power source through the outflow jet. In this study, the magnetic reconnection of a magnetic field in kilotesla order is produced by using an intense laser with pulse duration in picosecond (10^{-12} s) order to study outflow jet in semi-relativistic reconnection.

In the first part of this study, proton deflectometry is developed to directly probe the intense magnetic field generated in a laser platform. By injecting a proton beam with a wide energy spectrum, time-resolved magnetic field probing was also achieved. The second part of this study is about a magnetic reconnection experiment performed by the LFEX laser facility. The reconnection magnetic field of 2.1 kT is generated by the microcoil scheme and measured by time-resolved proton deflectometry. Electron magnetization comparable to accretion disk corona of Cygnus X-1, a typical black hole binary system, was obtained. The particle energy spectrum of the reconnection outflow jet was measured, which possesses significant power-law component. This result supports magnetic reconnection models for powering hard-state X-ray emission from accreting black hole systems.

Acknowledgements

Thanks to the support from many people this thesis could be completed. I would like to express my gratitude to them here. First of all, I would like to express my appreciation and thanks to my supervisor, Prof. S. Fujioka, for his support of my Ph.D. related research and his guidance helping me in writing this thesis. I would like to thank the committee members of this thesis, Prof. T. Yamanaka, Prof. Y. Sentoku, Dr. Y. Arikawa and Dr. T. Sano, for the comments and suggestions during the defense. Also, I would like to thank Prof. H. Azechi, as my supervisor during the first two years in graduate school, when I was in the master course. I am glad that I could do my research in the Institute of Laser Engineering (ILE), a facility with state-of-the-art intense lasers LFEX and GEKKO-XII. I would like to give special thanks to Prof. R. Kodama and Prof. Azechi, as director and former director of ILE.

The first part of this work obtained support and supervision from members in the FIREX project. Therefore I would like to express my gratitude to all of the colleagues and collaborators contributing to the FIREX project. It is my pleasure to contribute, even only a tiny contribution, in the fast ignition inertial confinement fusion research.

The second part of this work was supported by the Japan Society for the Promotion of Science (JSPS), which I would like to thanks for getting financial support from JSPS as a Research Fellowship for Young Scientists. I would like to thank Prof. J. J. Santos and Mr. M. Bailly-Grandvaux for their support and advice on magnetic field detection and analysis during and after the proton deflectometry experiment. I would like to express my appreciation to Dr. A. Morace for any advice given to me about laser-accelerated proton beam generation and PIC simulations. I am also thankful to Dr. K. Kondo, our collaborator of the magnetic field generation research, for his support and advice during the proton deflectometry experiment.

I would like to thank Prof. Ph. Korneev for his support and advice on the magnetic reconnection experiment. I would like to thank Dr. Y. Abe for working together on many aspects of the magnetic reconnection experiment. My thanks also go to Prof. A. Yogo, Mr. K. Koga, Mr. K. Okamoto, and their colleagues, for their support on ion energy spectrum measurements in magnetic reconnection experiment. I would like to thank Prof. T. Ozaki for his support on electron diagnostics.

I would like to express my gratitude to members and former members of the Laser-Produced High-Field Sciences Group (previously Laser Fusion Group) of ILE, Osaka University. I am thankful to Dr. Y. Arikawa, Dr. N. Tanaka, Dr. S. Sakata, Dr. S. Kojima, Dr. B. Zhu, Dr. S. Lee, Mr. K. Matsuo, Mr. H. Morita, Mr. C. Liu, Mr. H. Kishimoto, Mr. S. Kambayashi, Ms. A.

Oshima, Mr. J. Nishibata, Mr. R. Takizawa, Ms. M. Takemura and Mr. S. Guo for their friendliness and kindness.

In such a large scale laser facility, any experiment could not be performed properly without the great efforts of technical staff in ILE, for laser operation, target fabrication and plasma diagnostics. Here I express my gratitude to them for their support. I especially appreciate Mr. K. Kawabata and Mr. K. Takahashi's effort to maintaining close communication between technical staff and scientists participating in experiments in ILE. Also, I would like to thank Ms. H. Hosokawa for her support on target fabrication and Mr. O. Maegawa for his support on experimental diagnostics fabrication.

Finally, I would like to thank everyone who supported me spiritually in these years: My parents; Best friends in my hometown, Hong Kong; New friends from all over Japan; μ's; and Aqours.

Contents

List of Figures

List of Tables

List of Abbreviations

AGN	Active Galactic Nuclei
GSI	GSI Helmholtz Centre for Heavy Ion Research
ICF	Inertial Confinement Fusion
ILE	Institute of Laser Engineering
LLE	Laboratory for Laser Energetics
MHD	Magnetohydrodynamics
PHELIX	The Petawatt High-Energy Laser for Heavy Ion EXperiments
RCF	Radiochromic film
TCC	Target Chamber Centre
TNSA	Target Normal Sheath Acceleration

Chapter 1

Motivation and Introduction

Magnetic reconnection, visually presented as "reconnection" of magnetic field lines in highly conducting plasmas, was recently recognized as a physical phenomenon that is necessary to be further understood. In terms of magnetic field lines, it is a rearrangement of the magnetic field geometry; In terms of energy, it is an energy conversion process from magnetic energy to the kinetic energy carried by charged particles in the plasma, as both thermal energy and anisotropic flow of the charged particle populations.

The interest in magnetic reconnection came from the fact that it is accounted for the energy conversion in a range of magnetized plasmas. The first theoretical study on magnetic reconnection by Sweet was presented to reproduce the order of magnitude of total energy radiation and time duration of solar flares[1]. Further studies suggested magnetic reconnection occurs in solar corona, Earth's magnetosphere and active galactic nuclei(AGN), accounts for phenomena including coronal mass ejection[2], energetic particle acceleration[3], powering of photon emission[4] and star formation[5].

Besides astronomical plasma, magnetic reconnection is also important to nuclear fusion physics. In magnetic confinement plasma, magnetic reconnection tends to dissipate energy from the designated magnetic field configuration[6, 7], which is usually considered as an unfavorable effect. In contrast to considering magnetic reconnection as a potentially destructive effect, recent studies have also suggested adopting magnetic reconnection as the heating mechanism in magnetic confinement plasma, such as the work on merging experiments recently performed in spherical torus devices[8].

It is very straight forward to study magnetic reconnection phenomena in astronomical plasmas with telescopic observations on those astronomical objects. However, "experiments" from astronomical plasmas is limited by the number of observable targets. Therefore, studies on astronomical magnetic reconnection related phenomena have to heavily depend on theoretical and numerical studies.

With the historical reason that having a common need to understand magnetic reconnection as a fundamental physical process in plasma, experimental studies in the laboratory were performed in many fusion devices. Magnetic reconnection was studied in magnetic confinement plasmas, generated in spherical torus devices[8, 9], MRX[10], VTF[11], and recently constructed facilities such as TREX[12].

An alternative scheme to study magnetic reconnection in the laboratory was developed, as laser technology had been rapidly developed since its invention in the 1950s. Plasma under extreme conditions could be produced in laser facilities, with their capability of ultra-high intensity ($> 10^{14}$ W/cm^2). Magnetic reconnection situation of a loop-top X-ray source in solar flare is simulated in laboratory, by a scheme of bringing a pair of expanding magnetized plasma "bubbles" to collide, produced from a pair of focusing laser[13]. Instead of making use of the spontaneously generated magnetic field from laser irradiation, a more controllable magnetic field generation scheme was also developed in the laser platform. The most representative example is "laser-driven capacitor coil"[14], which is also introduced to produce magnetic reconnection as an alternative scheme[15].

In this work, a novel approach that generates magnetic reconnection with magnetic field amplitude in kilo-tesla order was demonstrated in an experiment. Magnetic reconnection in plasma with such intense magnetic field is in the semirelativistic magnetization scheme, which is directly comparable to the coronae of accretion disks in black hole systems. Reconnection outflow jets and its particle energy spectra were measured in the experiment, which provided experimental verification of magnetic reconnection contribution, on high energy photon emission mechanism in those black hole systems.

It is essential to properly characterize the magnetic field generated in the experiment, while it is not easy for amplitude in order of kilo-tesla, in the scale of laser-produced plasma. The author had worked on the development of the magnetic field characterization by proton probing method and demonstrated this method on the above-mentioned laser-driven capacitor coil. Details of these works would be mentioned before the sections about the magnetic reconnection experiment.

The author had contributed to experiments at the Institute of Laser Engineering (ILE) in Osaka University, PHELIX laser facility at GSI Helmholtz Centre for Heavy Ion Research (GSI) in Darmstadt, Germany and OMEGA EP laser facility at Laboratory for Laser Energetics (LLE) in Rochester, US. In ILE experiments, the author had contributions to performing the experiments including the design of the whole experimental setup, design, preparation of proton detection diagnostics, setting up and operation of other experimental diagnostics and most of the data analysis. A Monte-Carlo particle tracing code was constructed by the author for the data analysis. In the PHELIX experiment, the author mainly contributed to the preparation of proton detection diagnostics and other experimental diagnostics. In the OMEGA EP experiment, the author contributed to the design of proton detection diagnostics and data analysis. Experiments performed in ILE, PHELIX and OMEGA EP were supervised by Prof. Shinsuke Fujioka, Prof. Joao Jorge Santos, and Dr. John Moody respectively. The analysis in this work was assisted by the usage of radiochromic film calibration data provided by Dr. Yuki Abe.

Details of different sections related to this work are described in different chapters, summarized below:

- Chapter 2 gives details of the laser systems, detectors, and magnetic field generation schemes that were used in this work. GEKKO XII and LFEX laser systems would be introduced in the first section. Main diagnostics in this work include differential magnetic probe and radiochromic film (RCF) stacks, described in the second section. Magnetic field generation schemes in this work, laser-driven capacitor-coil targets and snail-shaped targets, is described in this section.

- Chapter 3 provides a brief description of magnetic reconnection which is highly related to this work. Firstly, earlier models of magnetic reconnection are presented to illustrate the basic concept of magnetic reconnection. Recent studies from non-relativistic to ultrarelativistic schemes are then introduced, and the importance of semirelativistic reconnection is discussed in terms of Hall effect and two-fluid effects.

- Chapter 4 presents the author's work on the development of proton deflectometry, as a direct characterization method on the kilotesla magnetic field in the laboratory. Some typical magnetic field measurement techniques are first introduced. Then, details of an experiment for demonstration of proton deflectometry as a direct characterization method on kilotesla order magnetic field are shown.

- Chapter 5 shows the details of the magnetic reconnection experiment, which is the main scope of this work. Micro-coil target irradiation, the generation scheme of magnetic reconnection in this work, is first explained. Then, the design, configuration, experimental results, and analysis are reported in detail in this chapter.

- Chapter 6 gives further discussions on the experimental result. These include the physical parameters in the magnetic reconnection experiment, which were directly measured or indirectly estimated numerically, and also the energy spectrum of the accelerated particles in magnetic reconnection outflow. Discussions about the semi-relativistic regime of magnetic reconnection and power-law particle acceleration are shown in this chapter.

- Chapter 7 briefly summarizes the results of this thesis to conclude this work.

Chapter 2

Laser Systems, Detectors and Magnetic Field Generation Schemes

In the first section, the specifications of the high power laser systems are presented. After that, the details of the detectors and diagnostics in experiments are presented, including the specifications of the diagnostics, details and design concept of the diagnostics configuration. In the last section, magnetic field generation schemes as the application of intense lasers, used in this work, are introduced.

2.1 High Power Laser Systems

2.1.1 GEKKO XII

GEKKO XII laser system provides 12 synchronized laser beams with wavelength 1.053 μm, maximum output energy 24 kJ when the pulse duration is 1 ns. The seed pulse generated by the oscillator is of pulse duration from 100 ps to 1 ns and energy 10 μJ. The seed pulse is then amplified by four 25 mm rod amplifiers in series, with three optical shutters placed between the rod amplifiers. The seed pulse is then split into 12 laser beams and separately amplified by the main amplifier array consists of 12 rows of amplifiers, as shown in the left-hand side of Figure 2.1.

Each row of the amplifier array consists of two rod amplifiers, five disk amplifiers, one optical shutter, and two Faraday rotators. The diameter of rod amplifiers is 50 mm, while two disk amplifiers are in diameter 100 mm and the other three are in diameter 200 mm. The final laser beams each of diameter 350 mm are then guided to the target chamber room. According to the requirement of the final output wavelength, KDP crystals are used for the second and third harmonic generation before the final laser beams are guided into the target chamber room, while it is also the reason for choosing 350 mm as the beam diameter, to prevent damage on crystals. By focusing on f/3 focusing optics (for Target Chamber I in this experiment),

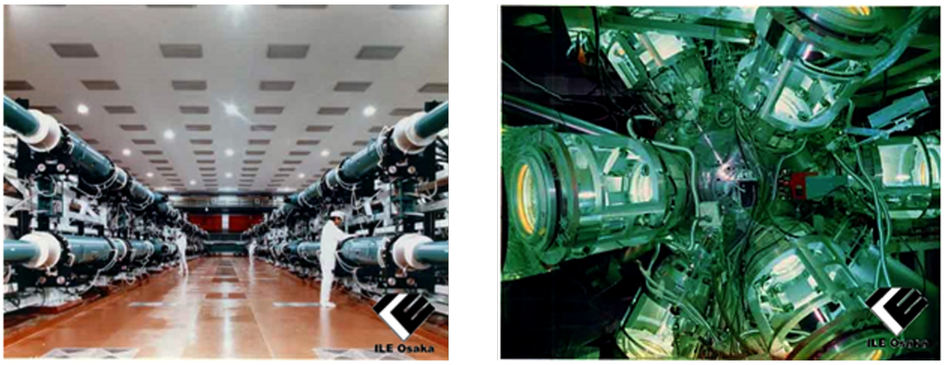

FIGURE 2.1: [16] (Left) A photo of the main amplifier array consists of rod and disk amplifiers. 4 of the 12 rows are shown in this photo. (Right) A photo of Target Chamber I of the GEKKO XII laser system. 12 laser beams are configured in spherical symmetric geometry, mainly for inertial confinement fusion experiments.

the peak intensity is about 3×10^{15} W/cm^2 per beam, by assuming 30% energy deposited in the circle of 100 μm diameter focus spot on target. On-target diagnosis showed the pulse duration of the GEKKO XII laser to be 1.3 μm in the Gaussian profile.

The GEKKO XII laser system has two target chamber, with different experiment capabilities. In Target Chamber I the 12 laser beams are configured in spherical symmetric geometry, mainly for inertial confinement fusion (ICF) experiments. The right-hand side of Figure 2.1 is a photo of the Target Chamber I. In Target Chamber II all of the 12 laser beams are bundled to enter the chamber from one direction, which allows higher on-target intensity for a wide range of experiments from fundamental ICF experiments to laboratory astrophysics experiments. Target Chamber I is used for the experiment in this work.

Currently, the GEKKO XII laser system is operated with restricted output energy to minimize damages on optics, with a maximum 1 kJ per beam in wavelength 1.053 μm. Between two target shots, a minimum time of 1.5 hours is required for cooling.

2.1.2 LFEX

LFEX laser system provides 4 synchronized laser beams with wavelength 1.05 μm, specification maximum output energy 10 kJ and pulse duration from 1 to 10 ps. Seed pulse is generated by a femtosecond fiber oscillator with pulse duration 90 fs, frequency 100 MHz. The seed pulse is first amplified by three Optical Parametric Chirped-pulse Amplification (OPCPA) in series, to a 6 Hz chirped-pulse output with 40 mJ, spectral width 6 nm. The chirped pulse is then amplified with two 50 mm diameter glass rod amplifier in four passes. The laser beam is then split into four beams, with each

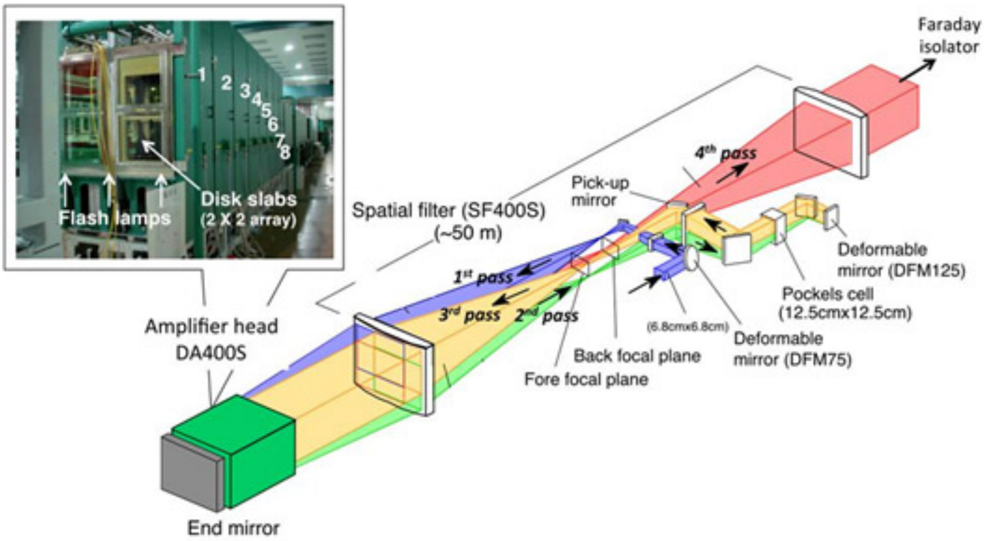

FIGURE 2.2: [17] A schematic diagram of the LFEX laser four pass main amplifier array, consists of 8 sets of disk amplifiers.

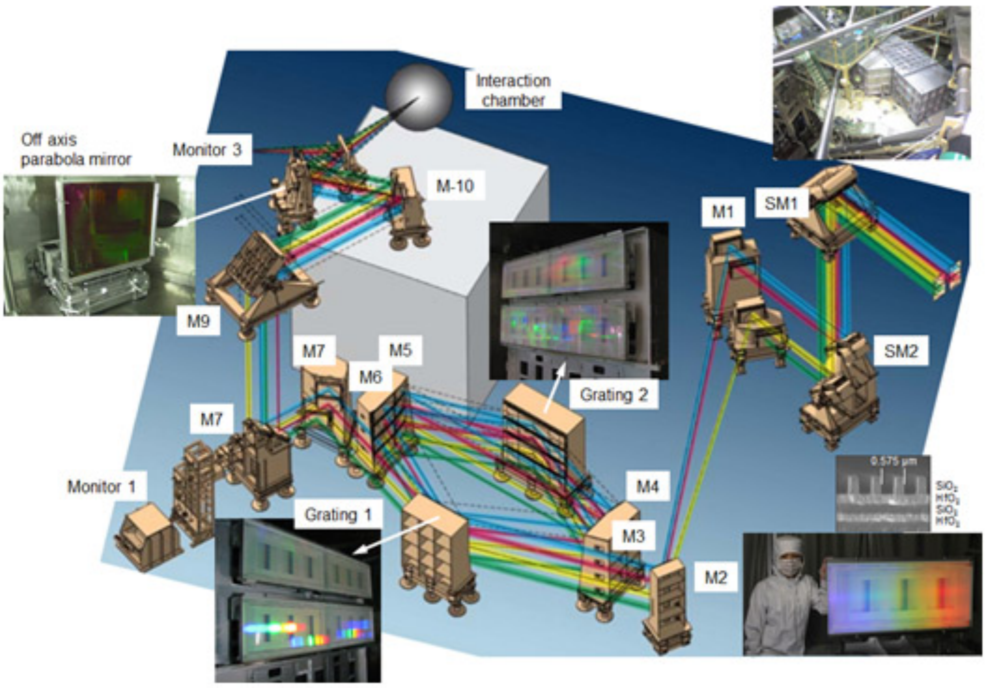

FIGURE 2.3: [17] A schematic diagram of the LFEX laser pulse compressor. In the pulse compressor, the chirped laser beam is recompressed by two diffraction gratings and then focused by Off-Axis Parabolic Mirror into the target chamber.

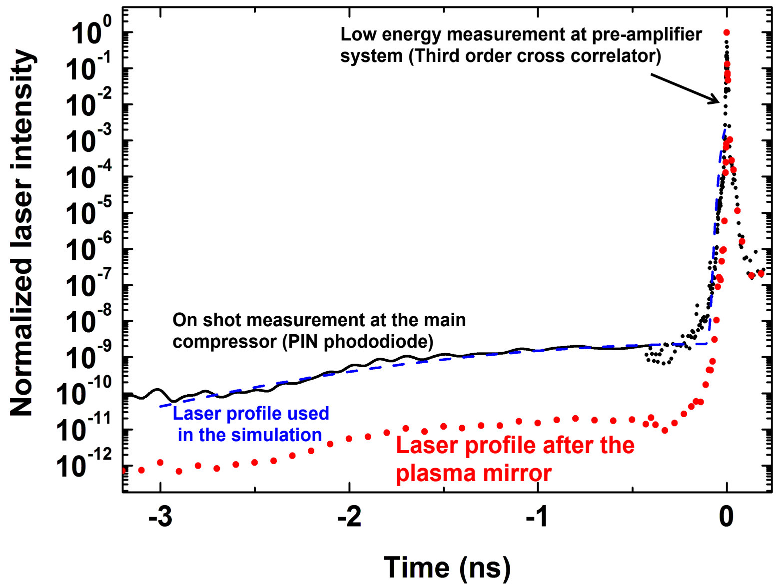

FIGURE 2.4: (Produced by Y. Arikawa) The black line is the laser temporal profile of LFEX laser, measured by a photodiode (before -0.4 ns) and third-order cross-correlator (after -0.4 ns). It gives a temporal contrast measurement result of at least 10^{-9}. The red dotted line indicated much better contrast level after introducing a plasma mirror, which is not used in this work.

beam separately amplified by two rod amplifiers. Finally, the laser beam is amplified by a 2×2 array, four pass main amplifier, with 8 disk amplifiers in series on each beam, as shown in the left-hand side of Figure 2.2.

After the amplification process, the amplified chirped beam is recompressed by a pulse compressor. For each beam, two 42×91 cm diffraction gratings with 1740 grooves/mm are used for pulse recompression. The 35×35 cm beam is then focused by an Off-Axis Parabolic Mirror (OAP) with about f/5. The schematic diagram is shown in the right-hand side of Figure 2.3.

Also by the output energy restriction, the maximum energy is limited to 500 J per beam, giving total maximum output energy of 2 kJ in 1 ps pulse duration. Despite the output limit, the maximum power 2 PW makes LFEX the world's highest power laser. As the result of using all four beams, the spot diameter on target is about 70 μm, with the same assumption 30% energy deposited in-circle the maximum intensity is about 1.6×10^{19} W/cm^2, when output energy is in the maximum value of 2 kJ.

LFEX laser is designed as a heating laser for the Fast Ignition scheme of ICF. However, such an intense laser is also capable of MeV proton beam generation by TNSA mechanism. A remarkable feature of LFEX, a good contrast level within similar lasers delivering kJ class energy, is beneficial for TNSA. Experimental measurements on Figure 2.4 showed the contrast

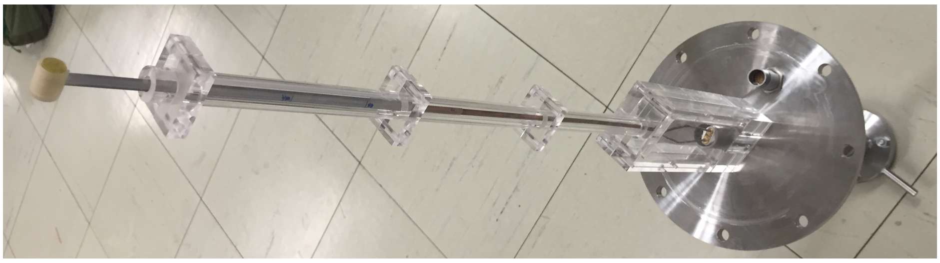

FIGURE 2.5: Photo of B-Dot probe RB-230, together with the device for the installation to the vacuum chamber.

level of LFEX is at least 10^{-9}, possibly reaches 10^{-10}. With this good contrast, up to 35 MeV protons are generated in the experiment of this work.

The LFEX laser is available in Target Chamber I of GEKKO XII laser system and is available to have joint shots with GEKKO XII. Somehow similar to the GEKKO XII laser system, LFEX laser requires a minimum time of 2 hours for cooling.

2.2 Experiment Detectors and Diagnostics

As a common feature of laser facilities, different diagnostics are installed through windows of the vacuum chamber (Figure 2.1) or aligned together with the targets before every laser shot. In this section, B-Dot probe and Radiochromic Film (RCF) stack are described. B-Dot probe was installed through one window of the chamber, and the RCF stacks were aligned with the targets before every laser shot.

2.2.1 B-Dot Probe

The working principle of the B-Dot probe is explained in Section 4.1.1, while the actual parameters would be listed in this subsection.

The model of the B-Dot probe used in this work is RB-230, a product of Prodyn Technologies.(Figure 2.5) It is a radiation-hardened model specialized in radiation environments such as laser-plasma experiments, for example, most of the output cables are protected by an aluminum shield tube. The parameter A_{eq}, the equivalent area of the probe coil, is 2×10^{-5} m^2, with less than $\pm1\%$ tolerances on sensor equivalent area claimed by Prodyn Technologies. The detection direction is along the axis of the probe cylinder, which means that it could measure the magnetic field tangentially (in normal to the unit position vector of the probe, from the center of target chamber), but not in the radial direction. A balun (model BIB-100G) is required to connect with the probe, which gives 8 dB of attenuation. Other connecting cables gave approximately 2 dB attenuation, so the total attenuation of electronic components was 10 dB. The maximum output voltage of the B-Dot probe (which is determined by that of the balun) is 1000 V and the bandwidth is from 250 KHz to 10 GHz.

The signal from the B-Dot probe was detected and recorded by an oscilloscope of bandwidth up to 4 GHz and a sampling rate of 20 GHz. It is sufficient for the required 1.5 GHz low pass frequency, which would be explained in Section 4.2.3.1.

2.2.2 Radiochromic Film (RCF) Stacks

As its naming, Radiochromic Film (RCF) are films that change its color when exposed to ionizing radiation. In this work, three types of Gafchromic films were used: HD-V2, MD-V3, and EBT-3 in ascending order of sensitivity.

2.2.2.1 Sensitivity of RCF

In the laser-plasma experiment environment, diagnostics always suffer from different sources of background signals, including X-ray which also has ionizing power on RCF films. Fast electrons generated during the TNSA proton acceleration process have similar flight paths with the proton beam, which also produces background signal on RCF films. Since different type of RCF have different detection limits in both upper limit and lower limit, it is important to understand the possible background level, or to cover most of the detectable ranges of different types of RCF, otherwise the RCF would simply be saturated by excess background signals, or see nothing because of the lower detection limit is even larger than the proton flux.

The dynamic dose range is listed as below [18]:

- HD-V2 : From 10 to 1000 Gray
- MD-V3 : From 1 to 100 Gray
- EBT-3 : From 0 to 40 Gray

Although the dose range seems to be enough for one only using HD-V2 and EBT-3 for detections, practically MD-V3 is still important for its corresponding dose range. It is because proton deflectometry requires a good quality of image, which is not likely to be obtained for marginal dose ranges, for example, 10-20 Gray in HD-V2. In such a case, MD-V3 would be a good choice, but practically only a small amount of MD-V3 is used because of the relatively high cost.

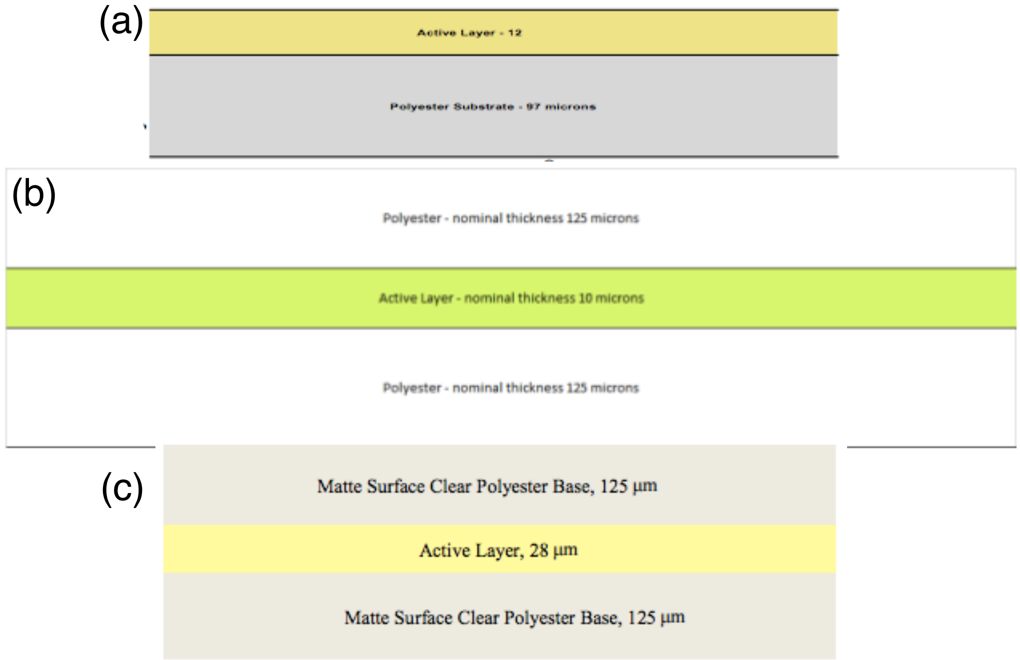

FIGURE 2.6: [18] Structure of three types of RCF: (a)HD-V2, (b)MD-V3, (c)EBT3. HD-V2 is asymmetric and the other two are symmetric.

2.2.2.2 Structure of RCF

To design the RCF stacks by calculating proton stopping distance, which will be described in the next section, the structure of the RCF have to be known. Figure 2.6 gives the structure of the three types of RCF.

2.2.2.3 Design of RCF Stacks by SRIM Code

When a charged particle passes through matter, it deposits energy through ionization. The energy deposition is usually represented by plotting the energy loss against traveling distance, which is called the Bragg curve. There is a common feature in such a Bragg curve that a sharp peak of energy deposition per unit distance always appears, which is called the Bragg peak. Since RCF only detects the ionization energy deposition on the thin active layer, because of the sharp Bragg peak most of the energy deposition being detected on a single RCF would be in a small energy range, in terms of the initial particle energy.

For proton deflectometry, it is a common practice to stack a large number of RCF (with metal filters between them when necessary), to record patterns of different energy within a proton beam. By using simulation codes calculating the stopping range of particles in the material, different proton initial energy corresponded to each layer of RCF could be determined.

In this work, the author used SRIM (Stopping and Range of Ions in Matter) code for this purpose. SRIM is a Monte Carlo simulation code, which

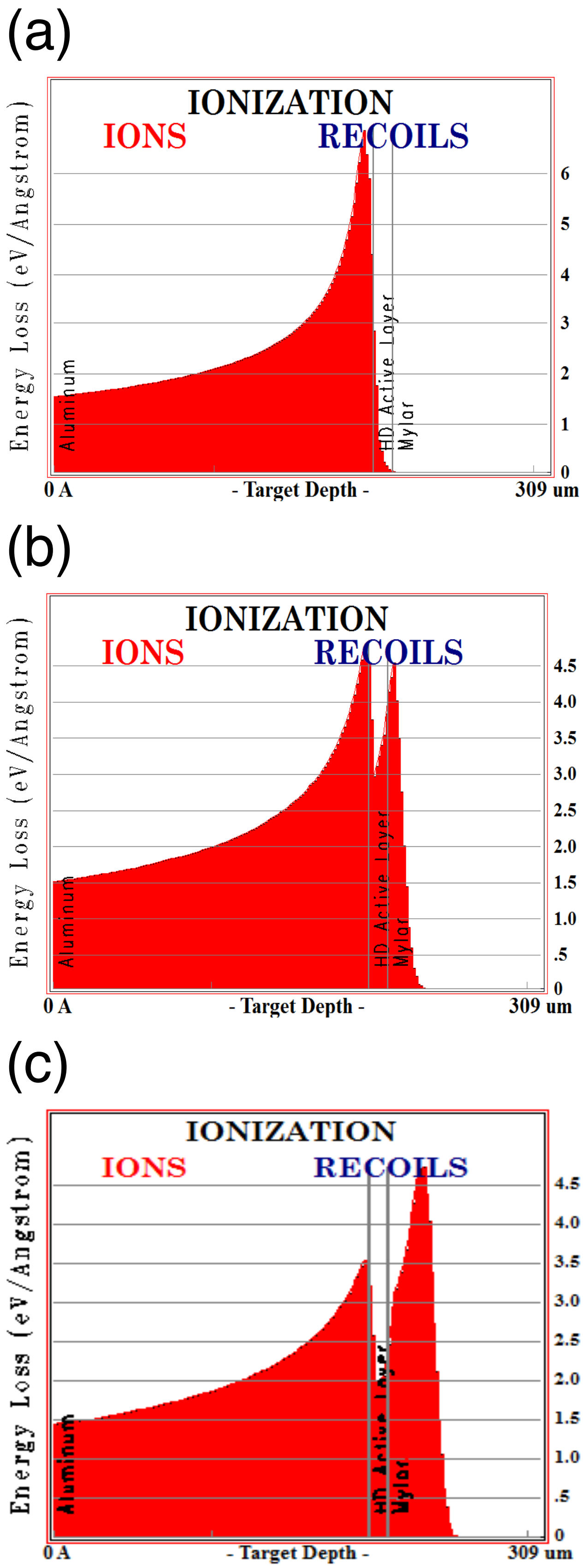

FIGURE 2.7: Calculation results of proton energy deposition by ionization from the SRIM code. 5000 (a) 5.1 MeV, (b) 5.3 MeV and (c) 5.5 MeV protons are injected in the simulation, where HD-V2 film is placed behind a 200 μm thick aluminum filter. Simulation results showed that the Bragg peak position is very sensitive to the initial proton energy, while the HD-V2 film mostly recorded 5.3 MeV in this case.

provides an output of ionization energy deposition in the material. It allows multi-layer simulation which fits the need of RCF stack design. One simple case of such calculation is shown in Figure 2.7, which consists of two layers, one piece of HD-V2 with its active layer faced towards proton incoming direction placed behind an aluminum filter of thickness 200 μm. It shows that the Bragg peak position is very sensitive to the initial proton energy. Since the active layer of RCF is very thin (12 μm for HD-V2), the range of proton energy recorded by RCF would be small. For example, the RCF in Figure 2.7 recorded 5.3 MeV in this case.

2.3 Magnetic Field Generation Schemes in Laser Laboratories

In this section, two magnetic field generation schemes powered by intense laser is introduced. The first one is laser-driven capacitor-coil, which is used in the proton deflectometry experiment. The second one is the laser-driven snail target, which is afterward modified and used in the magnetic reconnection experiment.

2.3.1 Laser-driven Capacitor-coil

Among different designs of the device for kilo-tesla magnetic field generation in the laser-plasma experiment platform, laser-driven capacitor-coil is one of the schemes that already being studied and practically used by a wide range of researches. A fabricated laser-driven capacitor-coil used in this work is shown in Figure 2.8. It could be observed from Figure 2.8 that the capacitor-coil consists of two plates connected by a wire. The two plates, with one of them having a hole on it, acts as a pair of capacitor plates. The magnetic field generation scheme is shown in Figure 2.9. By laser irradiation, an electric potential difference is constructed between the two capacitor plates and form a current along the connecting wire between the plates. The single-turn coil on the connecting wire generates the magnetic field, which is the major function of the capacitor-coil target.

In the demonstration described by [14], a CO_2 laser is used for driving the capacitor-coil target, which delivered total energy 100 J within 1 ns to the target. To drive the capacitor-coil target, such an intense laser beam passes through the hole of the front plate and irradiate on the rear plate, as shown in Figure 2.10.

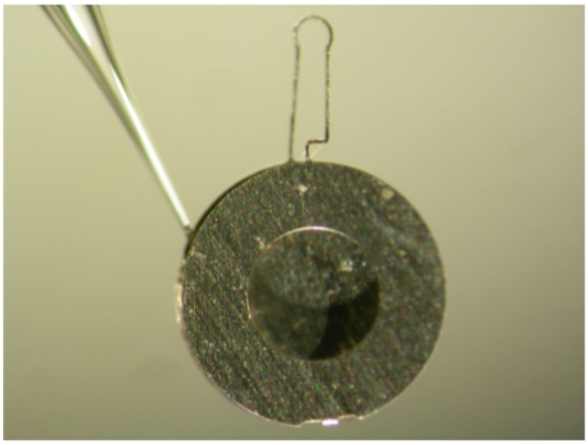

FIGURE 2.8: A photograph of a capacitor-coil target used in the experiment performed in ILE. Two capacitor plates, with a hole at the "front" plate for the laser beam incidence. The two plates are connected by wires to the small coil, which generates the magnetic field.

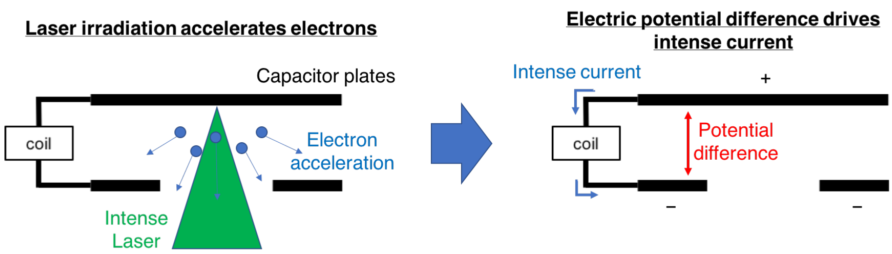

FIGURE 2.9: Schematic diagram of the magnetic field generation scheme in a capacitor-coil target. Electrons are accelerated away from the laser-irradiated capacitor plate by laser-plasma interaction. An electric potential difference between two capacitor plates is developed, which drives an intense current across the coil. The magnetic field in the coil is generated by this current.

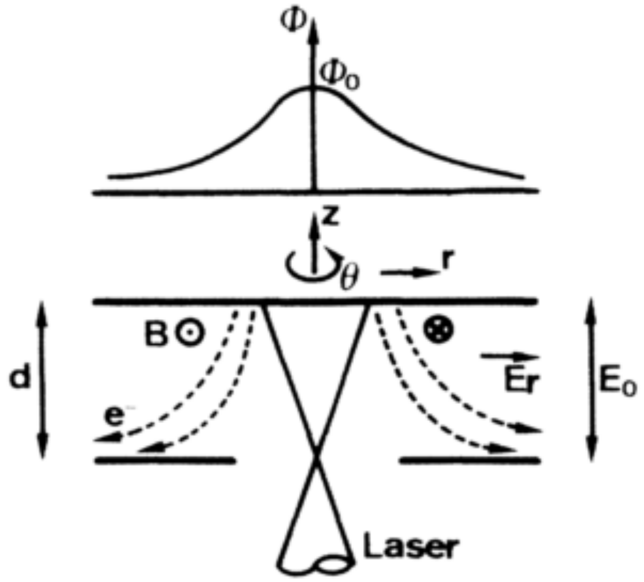

FIGURE 2.10: Schematic diagram of electrical potential development between two capacitor plates. Driving laser beam focus at the center of the hole in the front plate, and irradiated on the rear plate. By expansion and drifting motion, hot electrons create an electrical potential between the two plates and drive a large current across the coil. From [14].

The theoretical description could be found in the same work, where the essence would be explained here. By the irradiation of intense driving laser with intensity over 10^{14} W/cm^2, hot electrons with a temperature of order 10 keV are generated by resonance absorption within laser-plasma interaction [19]. Besides the isothermal expansion of the hot electrons, a toroidal magnetic field is generated between the two plates during the laser-plasma interaction, which has to be considered in the capacitor-coil design. The self-generated toroidal magnetic field from the laser indicated in Figure 2.10, produces an outward drift of the expanding electrons [20, 21], which determines the optimal design of capacitor-coil. The critical separation distance Z_c is determined by the equation (where the detailed derivation could be found in [14]):

$$Z_c = C_{sh}\tau_L \tag{2.1}$$

where C_{sh} is the hot electron sound velocity and τ_L is the driving laser pulse duration. From the study in [14], the relation of magnetic field amplitude and the plate separation is shown in Figure 2.11.

In that study, the predicted value of Z_c was 600 μm, which had a good agreement with the experimental result. By fitting the experimental result, a linear relationship was observed. It was explained by the increase of the shorting time by increasing the gap separation, without loss of hot electrons

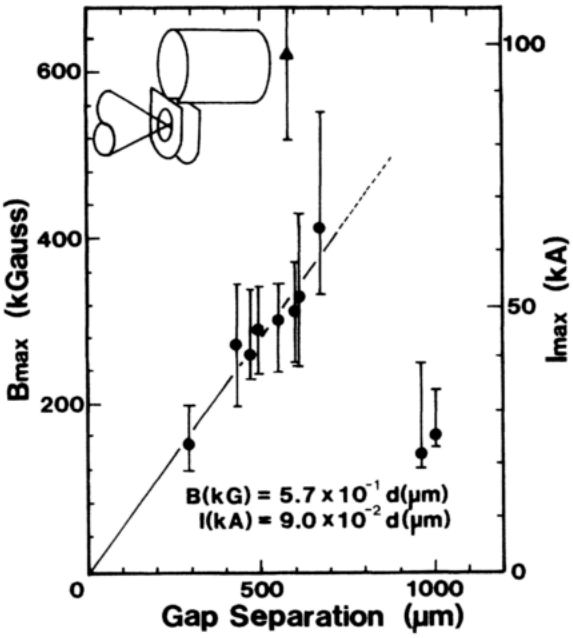

FIGURE 2.11: [14] Experimental result of the relation between capacitor plate separation and measured maximum magnetic field amplitude. It showed a linear relationship when the separation is smaller than 700 μm, and the magnetic field amplitude dropped significantly when the separation is about 1 mm.

as long as the separation is below Z_c. When the separation is larger than Z_c, a large proportion of the expanding hot electrons could not reach the front plate and the magnetic field amplitude greatly decreases. It is due to the hot-electron being outward drifted by the $\boldsymbol{E} \times \boldsymbol{B}$ motion as indicated in Figure 2.10.

In the experiment in this work, the capacitor-coil target design was based on the original design in [14], with several changes came from experimental needs. The diameter of the coil was changed from 2 mm to 500 μm to achieve larger field amplitude by a tradeoff of shrinking the magnetic field region. Also, in recent years the emission lines of copper, especially the K-α emission lines, are powerful tools for diagnosis during laser-plasma experiments [22]. To avoid the generation of copper X-ray emission during such kind of experiments, material other than copper is preferable. Therefore, instead of copper, nickel capacitor-coil was chosen in this work.

The material dependency of the magnetic field generated by the capacitor-coil was studied experimentally [23]. Magnetic field amplitudes generated by copper, nickel, and aluminum capacitor-coil were measured by differential magnetic probe, and the result is shown in Figure 2.12. The maximum magnetic field amplitude generated by nickel capacitor-coil is about 70% of that of copper capacitor-coil, which still can achieve a kilo-tesla magnetic field with the advantage of free from copper X-ray emission by the

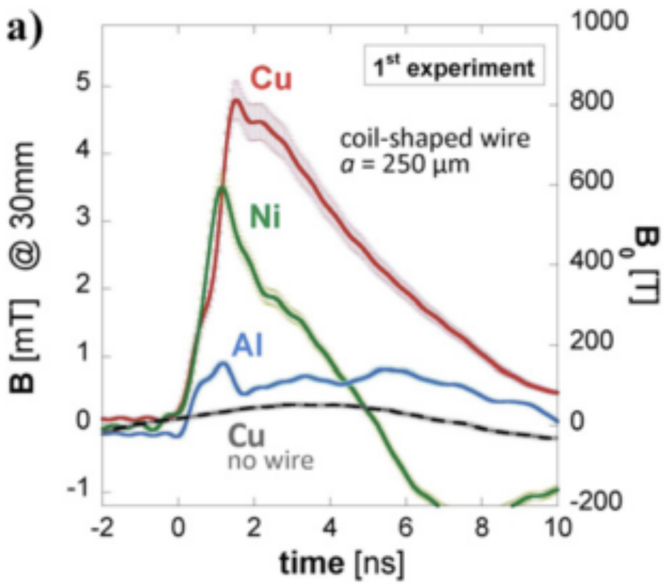

FIGURE 2.12: [23] The plot of the magnetic field amplitude generated by capacitor-coils of different materials over time. Copper (red), nickel (green) and aluminum (blue) are compared by this result. Also, the detected field by irradiating capacitor plates without any connecting wire is plotted as a reference.

capacitor-coil itself.

2.3.2 Laser-driven Snail Target

The laser-driven capacitor-coil scheme introduced in the previous section was proposed 30 years ago [14], while both the driving laser beam and generated magnetic field are in nanosecond order time durations. There is also a historical reason for the intense laser construction that such lasers are mainly developed and constructed at large-scale facilities in such years. By the recent development and construction of ultra-intense lasers that could deliver kilojoule energy within a picosecond, new schemes of intense magnetic field generation could be tested by those laser systems such as LFEX laser.

One scheme of using such ultra-intense, high power laser system for magnetic field generation is the concept of "Escargot target", or in English "snail target". A three-dimensional model of the target is shown in Figure 2.13, where the incident intense laser is also indicated. In [24] the concept of snail target is explained in detail, which is a combination of different physical phenomena: Laser pulse reflection by plasma, electron surface guiding effect and return current generation. Figure 2.14 shows the simulation result in that work, for electron density and magnetic field amplitude of snail target at different times. From the simulation, the magnetic field

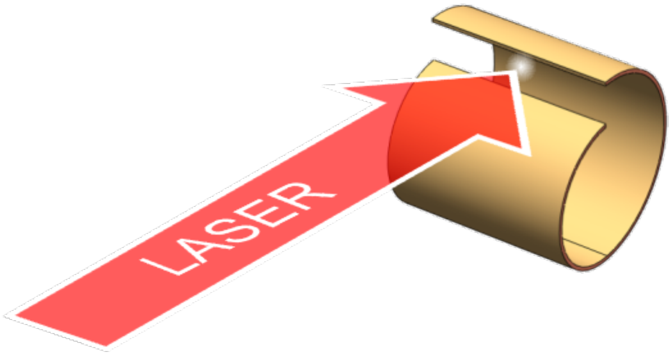

FIGURE 2.13: A three-dimensional model of an Escargot target. The direction of laser incidence is indicated as a red arrow.

shows dynamics in the picosecond scale, which is comparable to the laser pulse duration as other laser-driven targets scheme.

Ultra intense laser beam, with intensity 5×10^{19} $\mathrm{W/cm^2}$ in the simulation, passes through the open of the snail target and irradiates on its inner surface. Arrows in the diagram indicate the flow of electrons inside the snail target, which is driven by both electron surface guiding effect and return current generation. Along the target surface which is in the shape of a snail, the dashed arrow indicates surface guided electrons and the solid arrow corresponds to the return current electrons. These electron flows generated a magnetic field with amplitude exceed 20 kT as shown in the simulation results. Since plasma generated on the target inner surface reflects a portion of the laser beam as well as absorbing it, the snail-like shape of the Escargot target allows multiple reflections of the laser beam inside the target instead of escaping away from the interior of the target.

As there are multiple current flows located at the inner and outer surface of the targets, the situation appears complicated, but the current driving mechanism is indeed simple. The current component $\boldsymbol{j}_s$, in dashed arrow, was the effect of direct acceleration by intense laser irradiation [25]. Then, as the consequence of laser irradiation, electrons are accelerated away from the laser irradiation site, in a time scale that is much shorter than that of the ions. This results in an electron vacancy around the laser irradiation site, which builds up an electric potential that tends to attract electrons towards the irradiation site. It drives another layer of current $\boldsymbol{j}_r$, which is the return current that flows to neutralize the net charge built up by the escaped electrons. This effect determines the overall net-current in the target $\boldsymbol{j}_s + \boldsymbol{j}_r$, therefore the current system could be practically considered as an electric potential driven coil, with the negative electric potential generated by the laser irradiation which accelerated the electrons.

From Figure 2.14 (C2), one can observe from the in-plane magnetic field

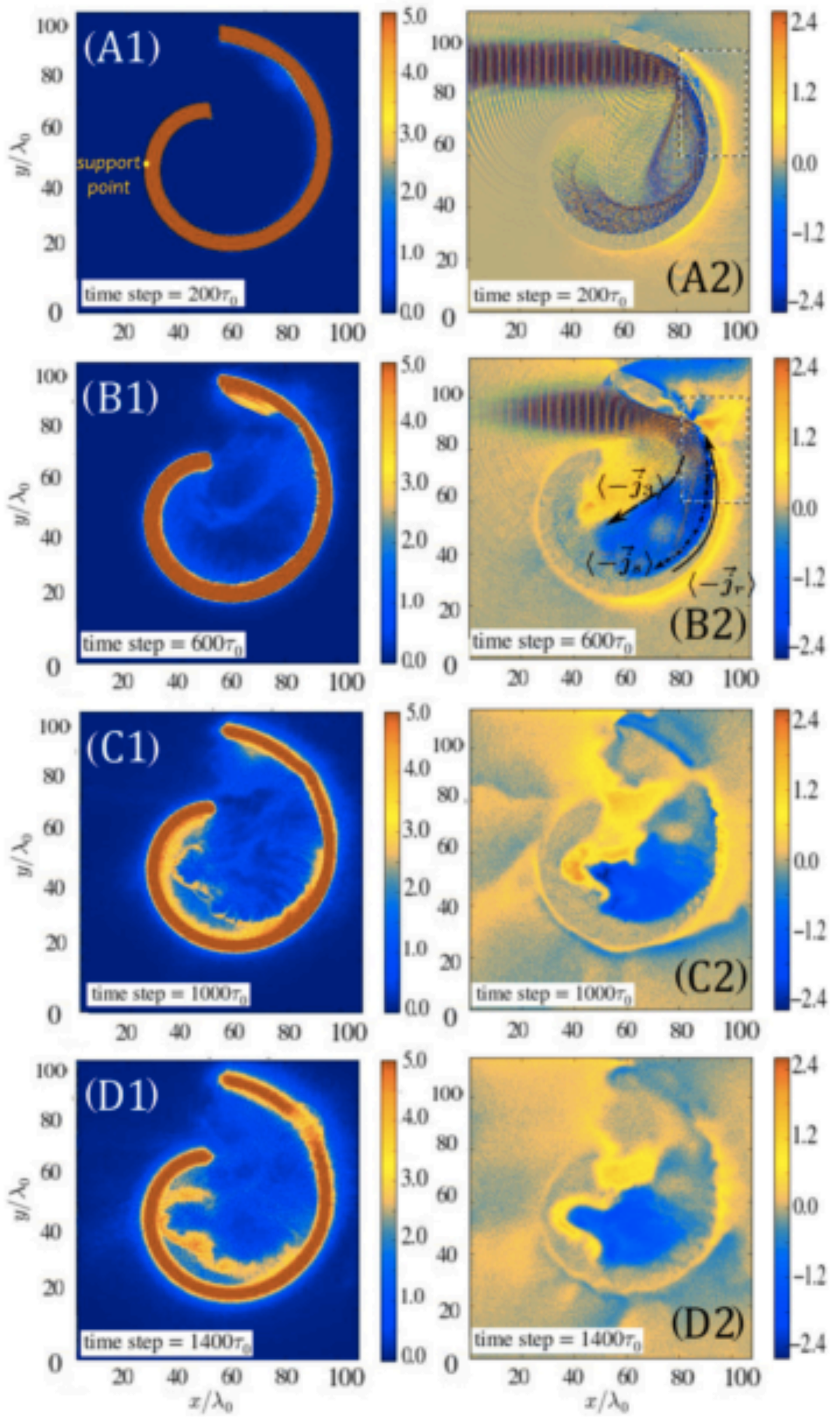

FIGURE 2.14: [24] Simulation result of the magnetic field generation by irradiating laser into an Escargot target. The left column is the electron density normalized by critical density, the right column is axial magnetic field amplitude in a unit of 1.16×10^4 T. Row (A) - (D) show result at time 0.62, 1.9, 3.1, 4.3 ps. Arrows in (B2) indicate the flow of electrons inside the Escargot target which drives the magnetic field.

around the snail target that the current flow along the target is indeed towards one location: the laser irradiation site. This is trivially insufficient to produce the in-plane direction magnetic field in the interior. This is also the consequence of the laser-plasma interaction, which accelerates electrons escaping from the irradiated surface in a much shorter time scale compared to ions. The accelerated electrons then encountered the localized, kilo-tesla magnetic field which confines them to flow along the center region of the snail target. This electron flow induces the "third current" $\boldsymbol{j}_3$ which produces the two-direction in-plane magnetic field that appeared in Figure 2.14 (B2-D2).

From the two-directional in-plane magnetic field geometry observed in Figure 2.14 (B2-D2), one might consider the possibility of magnetic reconnection in such a system. However, from the magnetic field generation principle, one would realize that the two-directional in-plane magnetic field is simply dominated by the geometry of the magnetic field generated by a single direction current flow ($\boldsymbol{j}_3$). Although magnetic reconnection might still be performed between the azimuthal magnetic field (in $+z$ direction) and the weaker $-z$ magnetic field generated at the opposite side ($-x$ side) of the snail target, it is well far away from the majority of dynamics happening in the whole system.

Chapter 3

Magnetic Reconnection

The main focus of this work is related to the study of magnetic reconnection. In this chapter, some basic concepts of magnetic reconnection are introduced.

In highly conductive plasmas, the magnetic field is frozen into the plasma and forced to move together with the plasma. In terms of the concept of field lines, the magnetic field lines are frozen into and move together with highly conductive plasma. The schematic of magnetic reconnection is shown in Figure 3.1, when plasmas carrying magnetic field lines in different directions approaches each other: Magnetic field lines should reorganize, break apart and reconnects by some process which involves violation of the frozen-in condition. As a consequence, the reorganized magnetic field lines will act a magnetic tension force on the plasma carrying the curved component of magnetic field lines.

In the following section, the early theoretical models of magnetic reconnection study are introduced. Although they are not complete in the modern point of view, they provided the basis of some physical pictures for the developing magnetic reconnection studies.

3.1 Early theoretical models of magnetic reconnection study

The concept of magnetic reconnection probably originated in the discussions about the heating mechanism of the solar corona and the "rapid" (of course, in terms of solar activity) energy release in solar flares. It started from the study of the correlation between the location of solar flare occurrence and sunspots where a significant magnetic field is observed[27, 28]. Then one would try to connect them in terms of energy: Magnetic field stores energy which its energy density u_B could be written as $u_B = B^2/2\mu_0$, where B is the magnetic field in space of permeability μ_0. With the magnetic field in order of kilogauss around such sunspots, a large quantity of energy is contained.

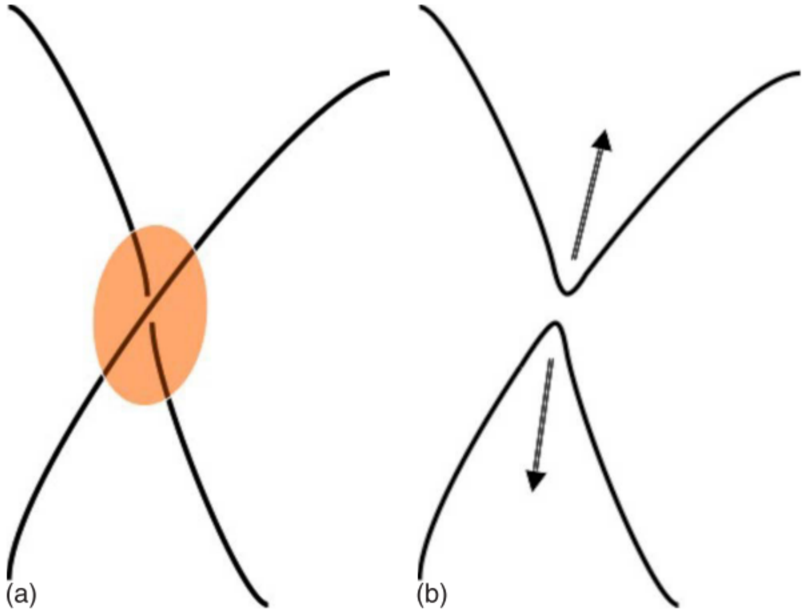

FIGURE 3.1: Schematic diagram of magnetic reconnection. After the reorganization of magnetic field lines, magnetic tension force acts on the plasma carrying the curved component of magnetic field lines, indicated by the arrows. From [26].

Is there exist a mechanism to convert this energy into the form of energy release in a solar flare, i.e. heat, photon radiation, and particle kinetic energy? In the first instance, one would consider the resistive diffusion between magnetic field domains pointing in opposite directions, which results in a decrease of magnetic field energy in the whole system, that has to be converted to any other form of energy according to the law of energy conservation. A rough estimation of typical diffusion time τ could be estimated by:

$$\tau = \mu\sigma L^2 \tag{3.1}$$

where μ is the permeability of plasma, σ is the conductivity of plasma and L is the diffusion length.

Some typical values of solar flares are obtained from [1] for rough estimation: Plasma temperature $T = 10^4$ K, $L = 10^7$ m taken from the length of the collision layer. σ could be estimated from Spitzer conductivity[29, 30]:

$$\sigma = [\frac{\pi Z e^2 m_e^{1/2} ln\ \Lambda}{(4\pi\epsilon_0)^2 (k_B T)^{3/2}}]^{-1} \tag{3.2}$$

where Z is the ionization degree, e is the electron charge, m_e is electron mass, $ln\ \Lambda$ is Coulomb logarithm, ϵ_0 is electric permittivity in the vacuum and k_B is Boltzmann's constant. Because of the majority of the hydrogen constitution, Z could be estimated by $Z \sim N_e/N_{total}$, which is in order of 10^{-4} (from Table I of [31]) in the chromosphere. For order of magnitude estimation, it is sufficient to let $ln\ \Lambda = 10$. From equation 3.2, we get $\sigma = 8.25 \times 10^6$ S. Let $\mu \sim \mu_0$ (permeability of typical plasma is not largely deviated from vacuum), from equation 3.1 we get $\tau = 1.03 \times 10^{15}$ s, which is obviously an unrealistic value compared to both time scales of solar flare activities (10^4 s[1]) and the cycle of solar surface magnetic flux replacement (5×10^4 s[32]). Even an order of magnitude estimation is sufficient to show that resistive diffusion is far too slow to be accounted for the energy conversion process.

The above result showed the relaxation of magnetic field geometry requires a time scale which proportional to the conductivity, recalls the property of a perfect conductor that magnetic field lines will be "frozen" in it. In most plasma that the conductivity is sufficiently high, this condition holds and the magnetic field lines are tied to the surrounding fluid motion. Being more precise, this is the situation that the magnetic Reynolds number $R_m = \sigma v L \gg 1$ (where v is a typical velocity of the fluid flow), or described as the value of τ is sufficiently large as shown in above example. This is referred to the scheme of ideal magnetohydrodynamics (MHD), that in Ohm's law,

$$\boldsymbol{E} + \boldsymbol{v} \times \boldsymbol{B}/c = \eta \boldsymbol{j} \tag{3.3}$$

the last term $\eta \boldsymbol{j}$ representing the effect of resistivity is negligible. The concept of magnetic reconnection enters when one question about what would happen in the case of the scheme of ideal MHD is broken. In the following subsections, two widely known MHD models of magnetic reconnection are described: Sweet–Parker model and Petschek model.

3.1.1 Sweet–Parker model

Most of the concepts of the Sweet–Parker model is shown in Sweet's proceedings[1], and most of the analytical derivation is shown in Parker's work[33]. In this subsection, a brief description will be given.

The construction of Sweet–Parker model started from a potential field of two approaching current systems, representing two approaching sunspots. Then, two situations are considered: The case of potential field in vacuum, and the case of potential field in a perfectly conducting medium. By derivations considering the difference between the potential fields in two situations, Sweet proved that the hydrostatic pressure must exceed a value in order $O(B^2)$ at some point in the system, in order to balance out the magnetic force acting on the induced current and maintain the hydrostatic equilibrium.

The physical meaning of this statement is that even in the majority of the system the ideal MHD holds, when two systems of dipole fields approached sufficiently close together, there exists a region between them that the force acting on the induced current is comparable to the fluid pressure. This means that $\eta \boldsymbol{j}$ term, the last term in equation 3.3, is no longer negligible and the ideal MHD no longer holds in this region. Practically, this is the situation that when the magnetic field systems are forced to approach, the induced current will be eventually large enough to break the ideal MHD approximation. The breaking of the ideal MHD allows the violence of the frozen-in of magnetic field lines, which is necessary for any topological rearrangement of magnetic field geometry.

In Figure 3.2 (a), the magnetic field line configuration in Sweet–Parker model is shown. The region that induced current flows and breaks the ideal MHD approximation is indicated by the red dotted lines.

The following part of the Sweet–Parker model was treated in pure hydrodynamics, demonstrated by an analogy of a thin gas layer between two parallel rigid plates. When the rigid plates are forced together, some gas will expel from the two ends of the region. This "ejected gas" is an analogy of the outflow jets in magnetic reconnection. In the situation of magnetic reconnection, the approaching magnetic field systems eventually reach their hydrostatic equilibrium, when the excess hydrostatic pressure is balanced by the magnetic pressure $B^2/2\mu_0$. Parker's work showed that this will eject mass from the current sheet layer, in the order of Alfvén velocity v_A:

$$v_A = \frac{B}{\sqrt{\mu_0 \rho}} \tag{3.4}$$

where ρ is the plasma mass density.

Another result of Sweet's work is that the rate of conversion from inflowing field lines to outflowing field lines, which is called reconnection rate in recent studies, is equal to the electric field E_N at the neutral point. From the Sweet–Parker model, the total time t_R for the reconnection process is estimated as:

$$t_R = \sqrt{S}(L/v_A) \tag{3.5}$$

where $S = Lv_A/\eta$ is the Lundquist number.

With this result, the value of t_R is estimated to be $\sim 10^7$ s [26]. Compared with the extremely slow resistive diffusion, it is much closer, yet still orders of magnitude away from the observed value in a solar flare ($\sim 10^4$ s).

In the scope of the work in this thesis, some discussion on Sweet–Parker model follows in terms of reconnection outflow jets. Like the analogy of gas layer and rigid plates, the description of the model focused and restricted in the region of the "gas layer", which is an extremely thin layer that the ideality of MHD is broken. In this model, the outflow is only allowed to

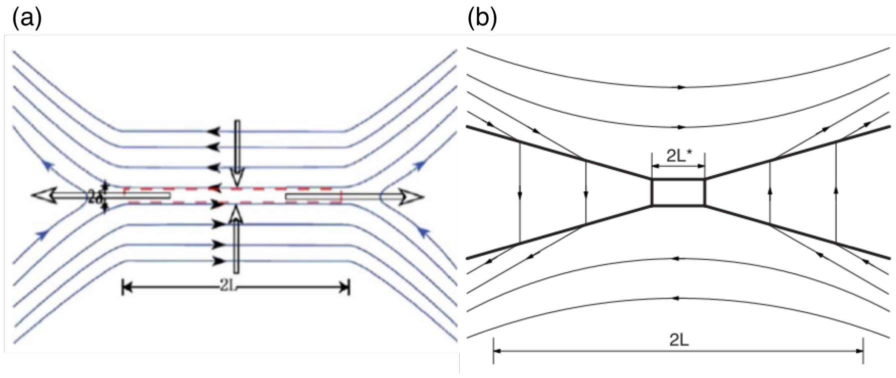

FIGURE 3.2: Schematic diagram of magnetic reconnection in Sweet–Parker model and Petschek model. From [26].

expel within the thickness δ of the layer, so the reconnection velocity (the plate velocity in the analogy) $v_r = (\delta/L)v_A$ would then be restricted to be slow. After the interpenetration of the magnetic field lines occurred in the region that ideal MHD is invalid, they flow into ideal MHD region and the largely curved reconnected field lines simply rearrange themselves by the magnetic tension force acted on plasma, in the Sweet–Parker model. This rearrangement corresponds to the outflow boundary condition in the model, which restricts the outflow layer from being too thick during the acceleration process. The layer has to be thin until the outflow is accelerated to order of v_A, otherwise the magnetic force is no longer sufficient, or in terms of Sweet–Parker model, the pressure balance could not be maintained.

From such limitations, the time scale provided by Sweet–Parker model was yet too large. As the first picture of magnetic reconnection, it is still remarked as an important work in the history of magnetic reconnection study.

3.1.2 Petschek model

Under the framework of MHD, efforts were made by Petschek in his work[34], and large effort of research has followed it. In this subsection, the modified version of Sweet–Parker model by Petschek, also called the Petschek model, is briefly described.

As mentioned in the previous subsection, the most serious limitation of Sweet–Parker model was the outflow limited in a very thin layer, that limited the reconnection velocity to a small value. Petschek modified the Sweet–Parker model in a sense that, the thinnest part of reconnection region (also called Sweet–Parker layer) is no longer extending along the whole length L, but a significantly shorter length L^*. At distance L^*, an outward slow shock is launched in the Petschek model, with an angle v_R/v_A and shock velocity v_R so that the shock appears stationary.

By this treatment, the outer part of "rigid plates" in Sweet–Parker model is no longer necessary to be in parallel to each other, but with an open angle which allows a larger mass to be accelerated as outflow, with the additional source of force by the slow shock. The difference between pictures of the Petschek model and Sweet–Parker model is shown in Figure 3.2. With the existence of slow shock in Petschek's work, MHD conditions are satisfied for an arbitrary selection of L^*. Similar to the result of Sweet–Parker model, the reconnection rate still depends on δ/L^*, the geometry of the Sweet–Parker layer. Petschek showed that the limit of this length is,

$$L^* > L\frac{(ln\ S)^2}{S} \tag{3.6}$$

from the length that current in shock affects the upstream flow into the Sweet–Parker layer. This gives the total reconnection time,

$$t_R = \frac{8}{\pi} ln\ S(L/v_A) \tag{3.7}$$

depends on $ln\ S$ instead of $\sqrt{S}$.

In terms of reconnection rate $R = v_R/v_A$, Petschek model speeds up the reconnection rate from $S^{-1/2}$ to $\pi/8ln\ S$. For solar plasma, $S \sim 10^{12}$. The Petschek's treatment speeds up the reconnection time in a factor of $\pi\sqrt{S}/8ln\ S \sim 10^4$.

The speedup of reconnection shown in the Petschek model brought the predicted order of reconnection time very close to the observed value, made it very powerful and attractive as a target to study. Therefore, it was historically extremely important in magnetic reconnection study. In terms of reconnection outflow, although limited in the MHD framework, the concept of energy transfer at the "X-line" gave a great influence on recent studies.

3.2 Recent picture of magnetic reconnection

3.2.1 Two-fluid description of magnetic reconnection

With the mainstream of two theoretical models mentioned above, early numerical simulations were performed in the MHD scheme, worked on reproducing results of such theoretical models. By imposing artificial conditions such as anomalous resistivity[35, 36] or modified upstream boundary conditions[37], fast reconnection as Petschek model was generated. Numerous efforts were made on verifying the Petschek model, but Biskamp's work showed that it could not be reproduced under uniform resistivity and the reconnection rate given by Sweet–Parker model was more consistent[38].

Then, these numerical simulations for magnetic reconnection revealed that the Sweet–Parker layer thickness δ is comparable or shorter than the

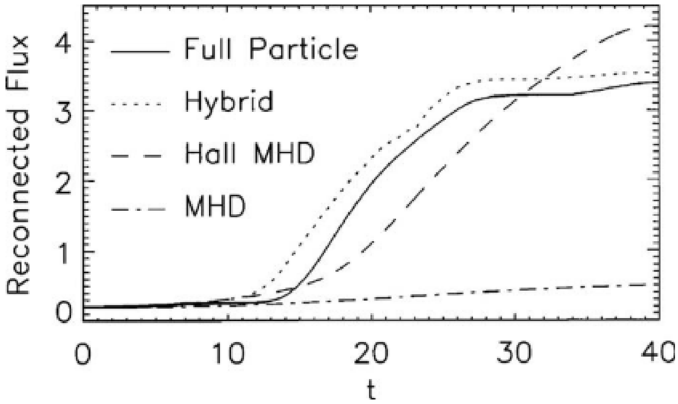

FIGURE 3.3: A comparison of the time rate of reconnected magnetic flux under different simulation schemes. All models except the MHD model show enhanced reconnection rates, despite the difference in their approaches on treating the two-fluid effect. From [39].

ion inertial length, in contrast to the condition of the ideality of MHD that the interested length scale should be sufficiently larger than ion inertial length. Therefore the MHD treatment is not sufficient, and the dynamics of electrons and ions had to be considered separately as two fluids.

In the 1990s, the development of computer technology opened the freedom for such separated treatment. Under the two-fluid effects, the traditional picture of Sweet–Parker layer changed into a region that ions and electrons decoupled, with thickness in the order of ion skin depth. Under this situation, a sufficiently thin electron current layer near the neutral point (Also called X-point) is still permitted because of the decoupling from ion motions. The two layers are usually known as ion diffusion region and electron diffusion region respectively, with thicknesses in order of ion skin depth and electron skin depth.

Although the validity of the Petschek model was questioned, two-fluid effects allowed some significant speedup in reconnection rates obtained in numerical simulations. As seen in Figure 3.3, the magnetic reconnection rate is found significantly higher when the two-fluid effect is considered, no matter whether the dynamic of ions and electrons are described in simulation as fluid or particles[39].

The physics behind is the effect of much thicker ion diffusion region allows a larger outflow rate, therefore speed up the reconnection rate. Although the speedup of this effect is not powerful as the Petschek model, other effects such as enhancement of plasma resistivity by instabilities[40, 41], shorten of the length of a single current layer by turbulent[42] or current layer internal physics[43]. These discussions about reconnection rate are out of the scope of this work, so the details would be omitted.

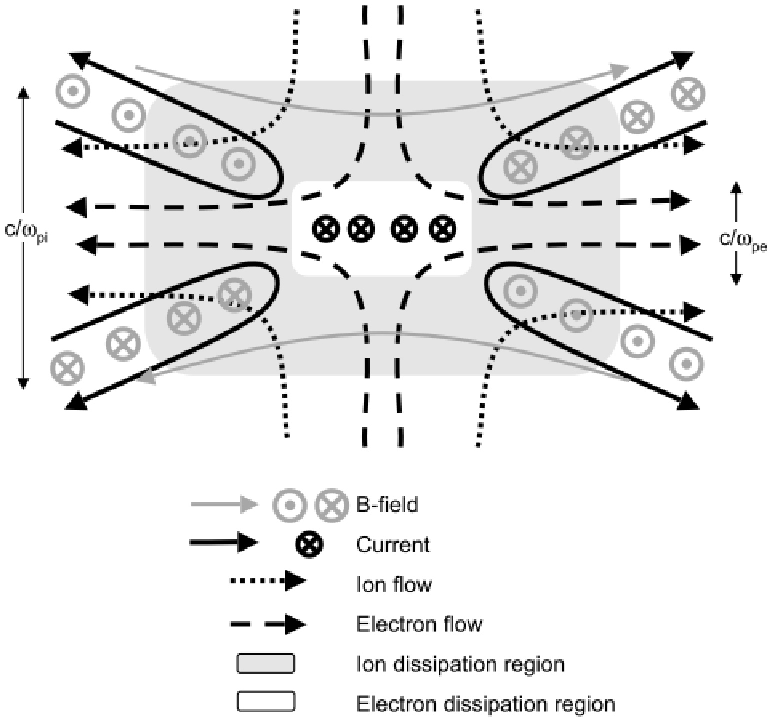

FIGURE 3.4: Schematic diagram of two-fluid dynamics in the reconnection layer. From [26].

3.2.2 Hall effect

The numerical studies with two-fluid description had changed the common picture of magnetic reconnection. Figure 3.4 shows a schematic for the magnetic reconnection system and the dynamics of ions and electrons. A more detailed plot of ion and electron flow in the simulation study is shown in Figure 3.5. Ions are not magnetized after crossing the reconnection "X line", or separatrix, and turn into the exit direction as reconnection outflow. However, electrons maintain their inflow towards the X point and then ejected from a much smaller region around the X point. Because of the difference in the flow between ions and electrons, net circular currents are formed and create quadrupole out-of-plane magnetic field, as shown in Figure 3.4. This is the signature of the Hall effect, which could be observed when ions and electrons are treated as two-fluid.

Such an electron flow pattern and reversal of the out-of-plane magnetic field are observed in space in-situ observation. For example, in observation in the magnetosheath, the amplitude of the Hall field is about 0.55 times of the reconnection magnetic field[44].

3.2.3 Relativistic effect on magnetic reconnection

In magnetic reconnection under high-energy astrophysical environments, the relativistic effect involves when a significant population of particles is

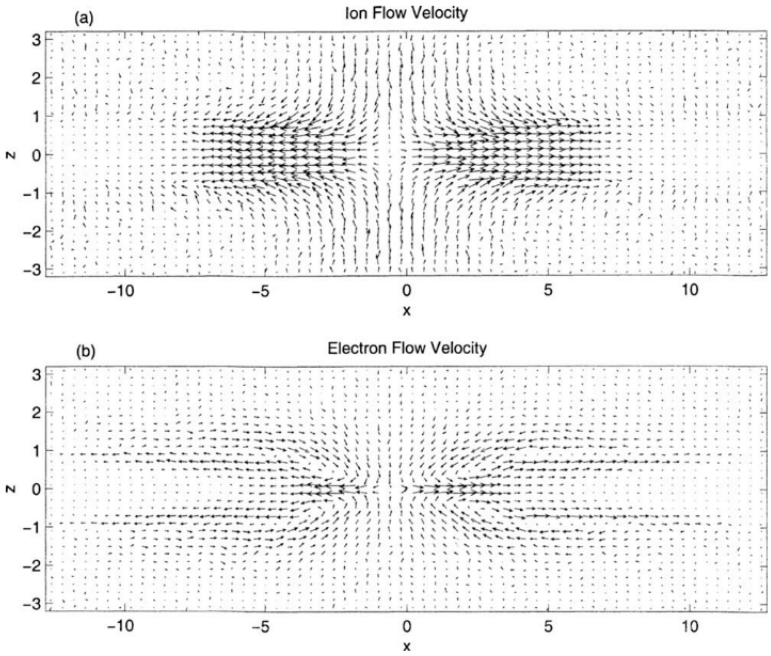

FIGURE 3.5: Patterns of ion and electron flows in . From [45].

accelerated to relativistic energy. Since the energy conversion efficiency from magnetic energy to particle kinetic energy is comparable to unity, the magnetization parameter σ_s (for particle species s) is adopted to characterize the magnetic reconnection condition:

$$\sigma_s = \frac{B^2}{2\mu_0 m_s n_s c^2} \tag{3.8}$$

where m_s, n_s are the mass and number density of particle species s and c is the speed of light. σ_s is the ratio between magnetic field energy density and particle rest-mass density, with an assumption of efficient energy conversion $\sigma_s > 1$ represents the situation that a significant portion of the particle population is accelerated to relativistic energy as the result of magnetic reconnection.

Similarly through numerical simulations, particle-in-cell (PIC) simulation scheme is usually adopted for studying such kinetic plasma processes, which is the powerful computational tool rapidly developed in recent years. Because of the numerical simplicity, the early studies involved pair plasmas, which consist of electrons and positrons (instead of ions). Also, as there are many applicable astrophysical environments for pair plasma in high-σ such as pulsars[46, 47], and gamma-ray bursts[4, 48], those numerical studies had their motivation to explore the understandings about relativistic magnetic reconnection. Many of these astronomical examples are observed to emit radiation which could not be explained by simple thermal models, with its spectrum extend to very high photon energy. Such radiation is thought to be produced by energetic electrons (and positrons in pair plasma), through synchrotron radiation and inverse Compton scattering mechanisms.

Early works of numerical simulations on magnetic reconnection had shown that the non-thermal, power-law distributed ($f(E) \sim E^{-p}$, E is particle energy and p is power-law index) high energy component would appear in the accelerated particle spectrum, even through test particle tracking in MHD simulations[49, 50]. However, PIC simulation includes the effect of such a non-thermal component of particle population back into the electromagnetic "background" field, which is a more self-consistent treatment than the MHD simulations. From recent PIC simulation works, particle energy distributions with power-law indices $p < 2$ was found in pair plasma with $\sigma \gg 1$, also called the ultrarelativistic regime[51–53]. Such a range of power-law indices is sometimes called "hard", because of its significance of powering high energy emission.

Pair plasmas are relatively easier to study, because of the absence of the difference between inertial lengths and Lamour radii of two species. Separation of diffusion (or dissipation) regions and Hall effect are therefore not observed in pair plasma simulations. However, electron-ion reconnection in the relativistic regime is also important in many astrophysical plasmas, such as emission from accretion disk coronae in black hole systems, astronomical jets from AGN and the electron-ion predominant case of gamma-ray bursts. Numerical studies on electron-ion plasma were limited due to the much heavier calculation cost, that the grid has to be fine enough to resolve the electron inertial length and the simulation box has to be large enough to contain the ion dissipation region. Improvement of computation power and numerical techniques (such as using a smaller m_i/m_e instead of real value ~ 1836) allows numerical studies of electron-ion plasma by PIC simulation scheme in recent years.

The ultrarelativistic regime in electron-ion plasma, defined by $\sigma_i \gg 1$, is relatively simple. This is because the inertial lengths and Lamour radii of electrons and ions are no longer depending on their rest mass but instead depend on their average particle energy when the majority of both electrons and ions are relativistic. The inertial lengths and Lamour radii of electrons and ions are approximately the same in this regime, and therefore the separation of dissipation regions and quadrupole field structure by Hall effect are excepted not to be observed. In 2016, Guo's recent study confirmed that most features of ultrarelativistic magnetic reconnection in electron-ion plasma is similar to that in pair plasma, including the hard ($p < 2$) power-law component for both electron and ion energy spectra[54].

The problem comes in when we consider what happens between the non-relativistic ($\sigma_e < 1$) and ultrarelativistic conditions. (In this work the ion represents proton except specifications,) With an electron-ion mass ratio ~ 1836 this is actually an intermediate regime with a wide range of magnetization spanning 3 orders of magnitude. This scheme is called semirelativistic, from its nature of relativistic electron magnetization $\sigma_e > 1$ but non-relativistic ion magnetization $\sigma_i < 1$. One can expect a transition between the two different limits, while the electron diffusion region thickness increases as the electron inertial length increase by the relativistic effect of higher average electron energy, approaching the ion diffusion region scale until both diffusion region overlaps and the Hall effect becomes eventually negligible. Also, one important question on semirelativistic reconnection would be: Would hard power-law component still produced in the electron population, even if the ions are not relativistically magnetized?

Earlier PIC simulation study[55] by using reduced electron-ion mass ratio (from 1 to 50) showed that in the range of $0.4 < \sigma_i < 14$, only non-thermal component with a steep slope ($p > 3.5$) could be found in the ion energy spectrum, or even no such component could be found. In contrast, the non-thermal component in the electron energy spectrum always has a smaller value of p, which is different from the ultrarelativistic regime. A more recent PIC study with real electron-ion mass ratio[56] then made a confirmation on the above expected transition between non-relativistic regime to ultrarelativistic regime, as well as providing findings on how important parameters change during this transition: Reconnection rate, ion-electron energy partition ratio, power-law index and cutoff energy of non-thermal component in reconnection outflow. In that work, an empirical formula for the power-law index was given as:

$$p(\sigma_i) \approx 1.9 + 0.7/\sqrt{\sigma_i} \tag{3.9}$$

for the range of $0.03 < \sigma_i < 10^4$ that was studied in [56]. This is quite higher than some results in [55] that have shown $p = 1.5$ for electrons, because of the limited "hot" magnetization $\sigma_{hot} \sim 25$ which take account of the particle kinetic energy and plasma pressure. Without this limitation, p would approach 1, instead of 2.

Even though it became possible to perform PIC simulation in real ion-electron mass ratio, the results are not yet conclusive since they are affected by various numerical reasons. Also, there is a lack of experimental work on this regime, despite its importance as reconnection rate, particle energy partition and high energy cutoff could not be simply estimated from the non-relativistic or ultrarelativistic limit. The particle acceleration in a semirelativistic regime would be the main focus of this work.

Chapter 4

Development of Kilotesla Magnetic Field Characterization Method

4.1 Measurement Techniques of Intense Magnetic Field

In this section, two methods that were widely used for magnetic field measurement would be briefly introduced in the first two subsections. The first one is a differential magnetic probe (also called B-Dot probe), which could record a long scale time evolution of the magnetic field at its position, though far away from the magnetic field region because of the detection limit. The second one is the Faraday effect (also known as Faraday rotation), which is used for magnetic field diagnosis through optical probing. Despite not being performed in this work, the Faraday effect is introduced in this section, as an alternative method of magnetic field characterization. By using different techniques, measurements with a wide range of time resolution could be performed, but the detection limit is affected by many different factors.

The last subsection of this section describes the concept of proton deflectometry, which is developed by the author and most related to this work. Practically it is performed in the same way as proton radiography (imaging), therefore the principle and some previous examples of proton radiography are introduced. After that, two methods of generating proton source in laser-plasma experiments are described in the subsection.

4.1.1 Differential Magnetic Probe (B-Dot Probe)

The differential magnetic probe is a type of probe coil, which is a direct application of Faraday's law. Faraday's law gives the relation between electromotive force and the magnetic flux through a coil:

$$\mathcal{E} = -N\frac{d\Phi_B}{dt} \tag{4.1}$$

where $\mathcal{E}$ is the electromotive force, N is the number of turn of the coil, $\boldsymbol{\Phi_B}$ is the magnetic flux through one loop of the coil. Practically, a differential magnetic probe is a combination of such coils, which induce the electromotive force with the relation of equation 4.1. By measuring the voltage across the probe coil, the rate of change of the magnetic field could be determined, which gives it the name "B-Dot probe" by its nature of measuring $\dot{\boldsymbol{B}}$.

Because of the complicated structure of B-Dot probe, the equation 4.1 is rewritten to combine several constants:

$$V_{out} = A_{eq}\frac{dB_\perp}{dt} \tag{4.2}$$

where V_{out} is the output voltage of the B-Dot probe, $B_\perp$ is the magnetic field perpendicular to the coil cross-section and A_{eq} is a parameter called "equivalent sensor area" (in m^2) which is sensor dependent.

The Φ_B in equation 4.1 is represented in terms of $B_\perp$ by the relation

$$\Phi_B = \boldsymbol{B}\cdot\boldsymbol{S} = B_\perp A \tag{4.3}$$

where $\boldsymbol{B}$ is the magnetic field, $\boldsymbol{S}$ is the area of coil cross-section in vector, A is the area of coil cross-section.

From the above derivations, one could interpret the parameter A_{eq} as a combination of N and A that both depend on the B-Dot probe design. Practically, the A_{eq} is confirmed by calibration in high precision using a uniform magnetic field source, performed by the manufacturer.

By using high-frequency oscilloscopes, measurements for time resolution up to a sub-ns scale could be performed. It is practically possible for all electronic instruments, oscilloscopes and B-dot probe itself compatible with several GHz frequencies for such time resolution.

One restriction of the B-Dot probe measurement is the maximum output voltage of V_{max}, which is the safety limit for the coil itself and other electronic components. With typical values of V_{max} and A_{eq} to be 1 kV and $10^{-5}\ m^2$, then the detection limit would be

$$\left(\frac{dB_\perp}{dt}\right)_{max} = \frac{V_{out}}{A_{eq}} = 10^9\ T\cdot s^{-1} \tag{4.4}$$

in order of magnitude. For the laser-generated kilo-tesla magnetic field, the pulse duration of the magnetic field is in order of ns ($10^{-9}\ s$). With maximum field amplitude in order of 1 kT ($10^3\ T$) and the rising time in order of 1 ns, the value of dB/dt is in order of $10^{12}\ T\cdot s^{-1}$, which is in factor 10^3 larger than the detection limit.

Because of the detection limit and safety measures, the B-dot probe cannot directly measure the laser-generated kilo-tesla magnetic field at the maximum position. Instead, the B-dot probe is usually placed a few centimeters away from the maximum position (a long distance in contrast to 1 mm^3 spatial scale), where the magnetic field peak amplitude is in 10^{-3} T (mT) order. To obtain the maximum magnetic field amplitude, one has to compute the magnetic field spatial profile analytically or numerically, and scale-up the measured magnetic field amplitude to the maximum amplitude by the calculated field profile. Such an extrapolation method bases on the accurate calculation of magnetic field profile, which limits the method for characterization with simple geometries, such as single-turn coils.

4.1.2 Faraday Effect (Faraday Rotation)

Faraday effect is a phenomenon originating from the small difference of refractive index inside a medium, between the left-handed and right-handed circularly polarized wave (L-mode and R-mode). From the fact that linearly-polarized transverse wave can be decomposed into a pair of L-mode and R-mode, the small difference of refractive index brings a small difference in phase speed between two modes under an external magnetic field along the propagation direction. It thus produces a rotation of the plane of polarization, when a linearly-polarized electromagnetic wave passes through a medium along the direction of the external magnetic field, which is also called Faraday rotation.

The detailed derivation could be found from [57], where the rotation of the plane of polarization in the plasma medium is given by

$$\alpha(L) \approx \frac{\omega_{pe}^2 \omega_{ce} L}{2c\,\omega^2} \tag{4.5}$$

where L is the length of medium with constant magnetic field along the wave propagation direction, ω_{pe} and ω_{ce} are the plasma frequency and cyclotron frequency of electrons in plasma respectively.

The ω_{pe} and ω_{ce} can be found by the relations

$$\omega_{pe} = \left(\frac{n_e e^2}{\epsilon_0 m_e}\right)^{1/2} \tag{4.6}$$

and

$$\omega_{ce} = \frac{e|\boldsymbol{B}|}{m_e} \tag{4.7}$$

where n_e is the electron density of the plasma, e is the charge of an electron, ϵ_0 is the vacuum permittivity, m_e is the electron mass and $\boldsymbol{B}$ is the magnetic field.

By these relations, the equation 4.5 could be rewritten as

$$\alpha \approx \frac{e^3}{8\pi\epsilon_0^2 c^3 m_e^2} n_e B_{\parallel} L \lambda^2 \tag{4.8}$$

where λ is the wavelength of the electromagnetic wave being rotated and $B_{\parallel}$ is the magnetic field component parallel to the electromagnetic wave propagation direction.

One has to note that the plasma is usually inhomogeneous, which the n_e and $\boldsymbol{B}$ (or $B_{\parallel}$) are not uniform for the whole medium, so the local $n_e B_{\parallel}$ have to be integrated along the whole path. Despite such a problem exists, the Faraday rotation is widely used to study the galactic magnetic field.

The same relation is also applicable in laboratory-produced plasma, so the magnetic field integrated along the plasma could be measured by using optical diagnostics together with a linearly-polarized probe laser, as long as the plasma is transparent. Instead of directly passing light through dense plasmas that eventually blocks the optical probe, an alternative approach is to use a solid crystal as the Faraday rotation medium. In a crystal, instead of plasma, the rotation of polarization is represented as:

$$\alpha = \mathcal{V} B_{\parallel} L \tag{4.9}$$

where $\mathcal{V}$ is a wavelength-dependent constant of the crystal, called Verdet constant.

Such an approach was adopted in different magnetic field generation experiments [58][23], in which the experimental setup in the experiments was of similar design, as one example shown in Figure 4.1. In both experiments, the crystal was placed at a position that is in a distance of 1 mm order from the coil center. It is not possible to make a measurement at the coil center, because the signal would blackout "quasi-synchronous with the laser irradiation", due to the crystal ionization by the hard x-rays and fast particles. Although this distance is 1-2 order closer compared to the B-Dot probe, extrapolation is still necessary to determine the maximum magnetic field amplitude.

4.1.3 Proton Deflectometry

By B-Dot probe or Faraday Rotation method, magnetic field amplitude in laser-plasma experiment could be measured with a detection limit much lower than kilo-tesla order, that is one of the goals of intense magnetic field generation. Therefore, for magnetic fields in kilo-tesla order, extrapolation with simulations is necessary to obtain the maximum magnetic field amplitude. It means that these methods could hold their validity only in the case that the magnetic field profile could be modeled with very high accuracy. These methods are still promising when they are applied onto the magnetic field generated by laser-driven capacitor-coil since a single-turn coil generated field is close to the dipole limit. However, for magnetic field

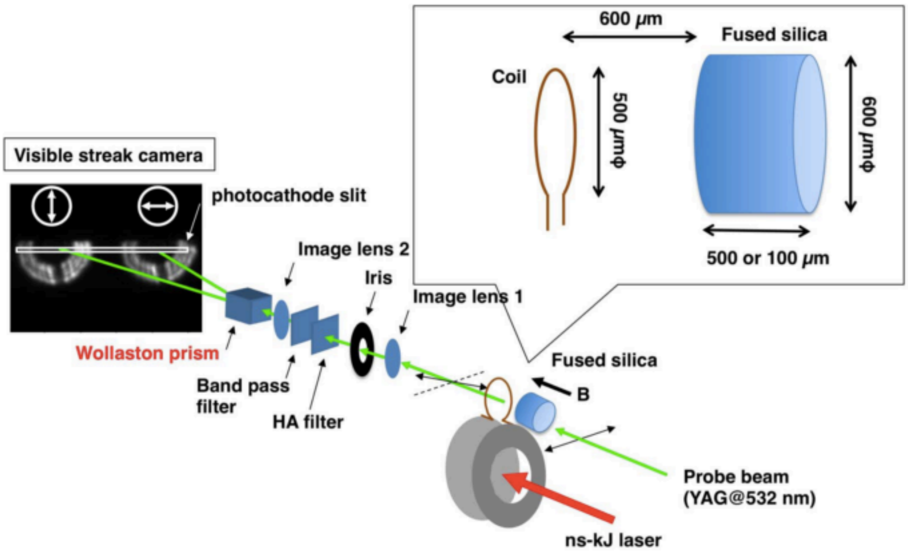

FIGURE 4.1: [23] A previous setup of an experiment performed in the GEKKO XII facility. An Nd:YAG laser was used as a probe beam, with its polarization plane being rotated when it passes through the medium. The probe was split by Wollaston prism according to their polarization, and being swept by a streak camera, which is a common instrument in laser-plasma experiments for time-resolved measurement.

amplification by flux compression, which could be achieved by compression of dense plasmas, measurements far away from the compression region are not likely to give information about the compression. Therefore, direct probing of a kilo-tesla order (or even larger) magnetic field has to be developed to make a proper evaluation of such a magnetic field generation scheme.

With this background, an approach of using charged particle beams as magnetic field probing was developed. Proton is usually used as the probing particle, while a detailed explanation would be shown in the following subsections.

4.1.3.1 Principle of Proton Deflectometry

Using particle beams for probing or imaging is certainly not a completely new idea. An electron beam is commonly used as conventional imaging, by instruments such as electron microscopes. Proton beam also has its potential for imaging because of its stopping range that could be suitable for applications such as proton medical imaging, besides its usual application for proton therapy treatment.

In the laser-plasma experiment, proton radiography is one of the powerful tools for imaging. The capability of obtaining a high-resolution image is demonstrated experimentally [59], which gives evidence of the potential of using MeV protons as an imaging tool. One of the applications of proton radiography is to probe a laser-driven implosion since the density distribution within the compressed dense plasma could be easily visualized by their effects on MeV energy protons. In the previous experiment, the asymmetric compression due to asymmetric laser irradiation from mistimed laser beams was successfully probed by proton radiography [60].

Besides probing the density distribution by the energy loss of protons, the property of being charge carriers allows protons as a tool for electromagnetic field probing. Under the electromagnetic field, Lorentz force $\boldsymbol{F} = q\boldsymbol{E} + q\boldsymbol{v} \times \boldsymbol{B}$ acts on protons, so that deflection patterns of protons could be used to probe electromagnetic field. In several experiments, proton radiography was used for probing electromagnetic fields generated by different types of laser-driven plasmas, including simple foil targets [61], hohlraums [62] and ICF implosion capsules [63].

In the above experiments, the motions of the proton are complicated that the effects of scattering, electric field, and magnetic field have to be considered, which requires large-scale numerical calculations to interpret the experimental result. However, if some of these effects could be neglected, the interpretation could be simplified and provide better quantification of an electric field or magnetic field.

In this work, the magnetic field generated by laser-driven capacitor-coil is probed by protons, at the time range when the coil region remains vacuum and not filled by plasma. In such situations, scattering and electric field effects could be neglected, that proton radiography could be a powerful tool in probing the magnetic field, directly in the field generation region. Since this method relies on the deflection of protons, it is called proton deflectometry in this work to distinguish it from the ordinary imaging objectives.

To correctly interpret the result, the Lamour radius has to be sufficiently larger than the magnetic field scale. As typical values, Lamour radius of a 15 MeV proton in 1 kT magnetic field is $m_p v/eB \approx 550\mu$m. For a laser-plasma experiment within a 1 mm^3 scale, it would be sufficient value in many cases. For electrons with the same energy, the Lamour radius is 1.7 μm, which means that the electrons are likely to be trapped by the too intense magnetic field. It is one reason that proton was chosen as the probing particle.

Proton deflectometry in the laser-plasma experiment uses a proton source (usually with a small size of source) for probing, proton then travels along the field region and deflects to a certain angle, finally detected by tracker materials or radiochromic films. To generate proton sources, two different schemes using intense lasers are commonly used in the laboratory, which would be introduced from the next subsections.

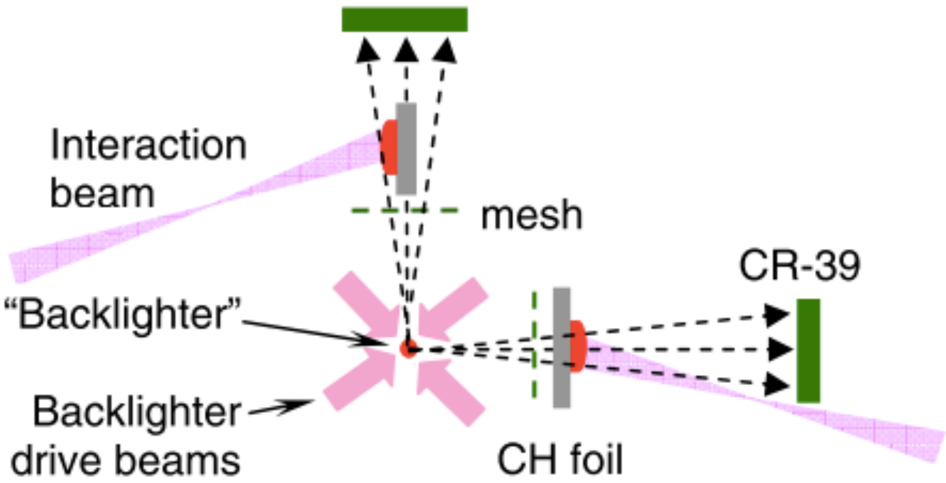

FIGURE 4.2: Experimental setup in [61]. Monoenergetic protons are generated by fusion products with only a small thermal broadening in energy, are used for proton deflectometry. A remarkable advantage is that fusion reaction proton source is isotropic, which allows more than one measurement by a single laser shot.

4.1.3.2 Proton Source with Fusion Reaction

One type of proton source generated by intense lasers is using protons from fusion reaction products. In [61], reaction $D + {}^3He \rightarrow \alpha + p$ generates protons around $E_p = 14.7$ MeV, by spherical implosion of D^3He capsules driven by nanosecond laser pulses, which are commonly used for compressions in ICF experiments. By such implosion, the center of capsule reaches temperature and pressure that required for such fusion reaction to occur in a short time. The temporal width of proton beam generation is in 0.1 ns order (0.15 ns in [61]), which is suitable for probing phenomenons during the implosion.

A remarkable feature of generating protons from fusion reaction is that the proton source is isotropic, together with a small source size (full-width half-maximum (FWHM) 45 μm in [61]). It allows multiple measurements within a single laser shot, with all the measurements having a quasi-point proton source. Figure 4.2 shows one example of making two measurements together in the same shot [61]. In many cases, it is important because of the limited number of available shots in large scale laser-plasma experiments.

4.1.3.3 Proton Source by Target Normal Sheath Acceleration (TNSA) Mechanism

The second scheme of proton generation in a laser-plasma experiment based on a particle acceleration mechanism called Target Normal Sheath Acceleration (TNSA)[64, 65]. When an ultra-intense ($> 10^{18}$ W/cm^2) laser pulse

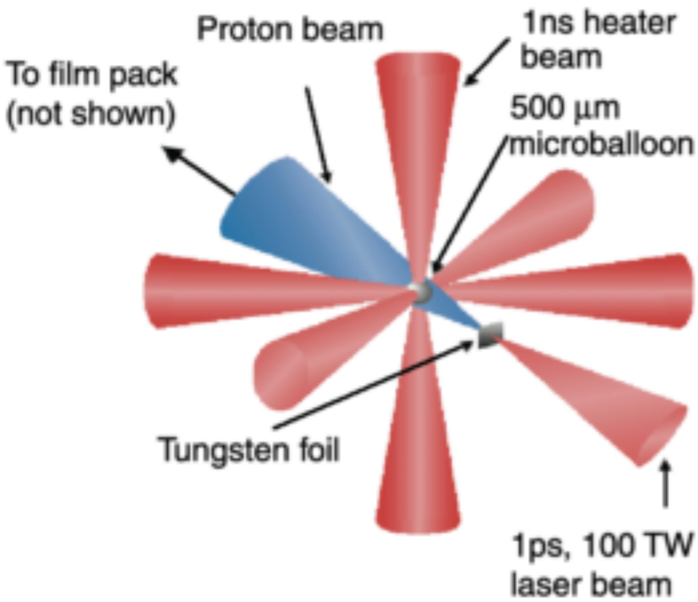

FIGURE 4.3: Experimental setup in [60]. An ultra-intense laser beam was irradiated on a 25 μm thick tungsten target to generate protons by TNSA, with a wide spectrum of energy up to 15MeV for proton radiography of a 6 beam implosion experiment. Proton generated by TNSA had small spread from target normal axis, which differs from the isotropic nature of fusion generated protons.

irradiates a thin solid target, ions (mostly protons, because of the smallest ion-to-electron mass ratio) can be effectively accelerated. Ions are accelerated by intense electric fields by strong charge separations. In the TNSA process, a relativistically hot electron population is produced and recirculate through the thin solid target, form a cloud of relativistic electrons at the rear surface with a length of several Debye lengths, which is also called Debye sheath. The strong charge separation over the Debye sheath responsible to the intense electric field for ion acceleration.

The experiment in [60] is one example of using TNSA thin foils as a proton source of proton radiography, as shown in Figure 4.3. In that experiment, laser with 1 ps pulse duration, 50 J energy, peak intensity 5×10^{19} W/cm^2 was used to produce a proton beam with maximum energy 15 MeV. TNSA produced protons were generated within time interval that is comparable with the laser pulse duration (which is in ps order), so that the measurement time precision is no longer limited by the proton source generation time.

Most of the TNSA protons are accelerated towards the normal direction of the plane of thin foil, with a relatively small spread leads to a large proton flux. Although the protons are not generated in an isotropic way, these properties of target normal acceleration (which is not sensitive to laser incidence angle) relieve the difficulties in experimental design, which would be shown in this work.

In this thesis, the development of proton deflectometry measurements using the TNSA scheme on thin foils as proton source was performed. It is because of the short generation time of proton beam from the TNSA acceleration scheme. For the magnetic reconnection experiment in Chapter 5, the 0.1 ns temporal pulse of proton source from fusion reaction is much longer than the predicted lifetime of the magnetic field duration itself.

4.2 Experiment of Applying Proton Deflectometry Under Kilo-tesla Magnetic Field

This experiment was performed to investigate the validity of proton deflectometry for direct measurement of a kilo-tesla magnetic field, by comparing its measurement result on laser-driven capacitor-coil with B-Dot probe measurement, which is still reliable under a simple and modellable current structure. The experiment was carried out at ILE, with GEKKO XII and LFEX laser.

The concept of the experiment is as follows; A magnetic field in kilo-tesla order, as well as satisfying the requirement that the spatial distribution could be precisely modeled, had to be generated and properly characterized by the B-Dot probe. Then, proton deflectometry measurement was performed and the magnetic field profile was individually estimated. Finally, the two measurements were compared to conclude if the proton deflectometry method is appropriate for the direct measurement of a kilo-tesla magnetic field.

In this experiment, the required kilo-tesla magnetic field was generated by laser irradiation of capacitor-coil targets. The principle of the magnetic field generation scheme is described in the next subsection.

4.2.1 Target Design

In laser-plasma experiments, objects to be focused on and irradiated by intense lasers are essential, which are usually called "target". In this section, two types of target irradiated by laser shots in this experiment are described in detail, before describing the experimental setup: The first one is the capacitor-coil target, which its principle was described in the previous chapters. The second one is the proton backlighter target, which is essentially a thin foil for laser irradiation to perform TNSA ion acceleration.

4.2.1.1 Capacitor-coil Target

By the mechanism described in Section 2.3.1, laser-driven capacitor-coil targets were used to generate an intense magnetic field in this work. In this

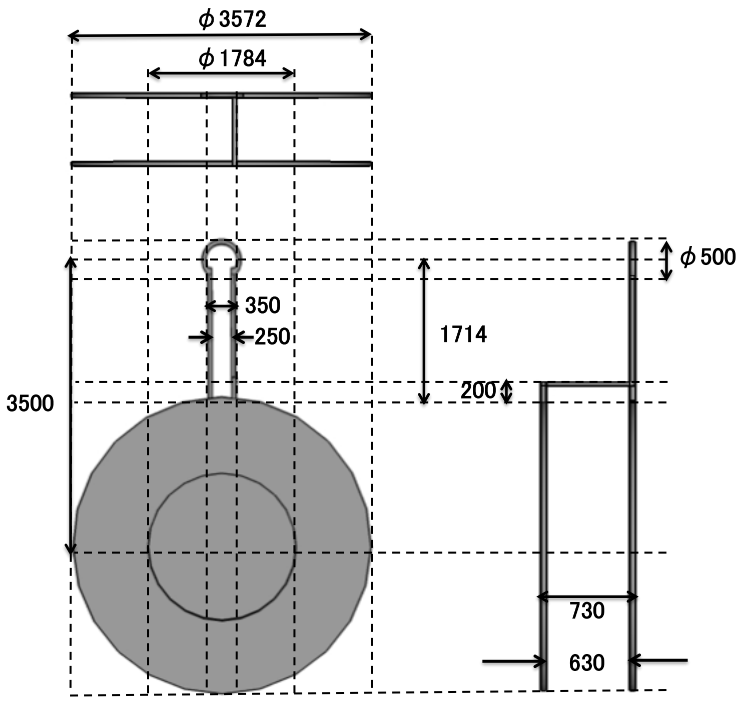

FIGURE 4.4: Detailed dimension of the capacitor-coil target being used in this work. (Unit: μm)

work, this target was irradiated by one beam within 12 beams of GEKKO XII laser, which have a maximum intensity of 3×10^{15} W/cm^2 in wavelength 1.053 μm. The details of the capacitor-coil in the experiment is given as follows:

Nickel is used as the material of capacitor-coil targets, where the material dependency is studied in [23]. The dimension of the capacitor-coil targets is shown in Figure 4.4. The diameter of the two capacitor plates is 3572 μm, while the hole diameter of the front plate is 1784 μm. The separation distance between two capacitor plates is 680 μm. The distance between the center of the capacitor plate and coil center is 3500 μm. The thickness of the connection wires and the coil section is both 50 μm, and the separation between connection wires is 300 μm. The coil is in diameter 500 μm, with a half open-angle 36.9° for the connection wires to the capacitor plates.

In a similar experiment, a hypothesis was given that the proton deflection was strongly affected by the electric field generated by the plasma expanding from the capacitor plates and accumulating around the coil, therefore only up to 100 T of the magnetic field was successfully measured [23]. To keep the volume surrounding the coil center free of such expansion plasma, a 50 μm thick tantalum plate was placed between the capacitor plates and the coil. The configuration of these different components would be shown in the later subsection.

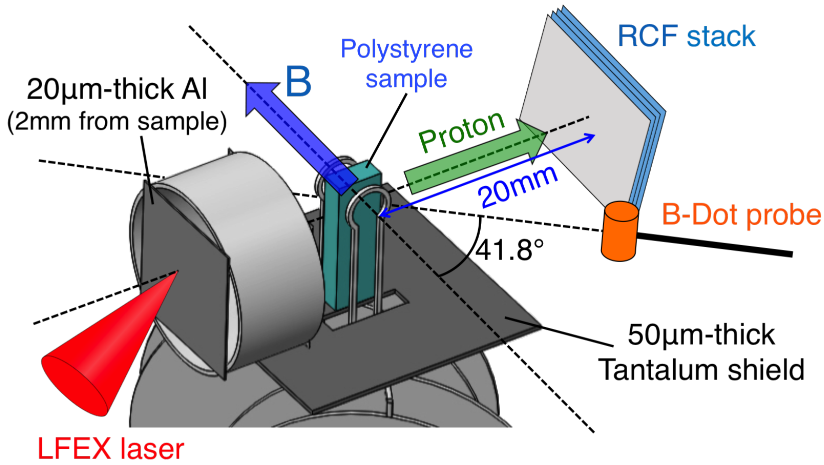

FIGURE 4.5: [67] Experimental configuration inside the target chamber. For simplicity, the proton backlighter, RCF stack, and the B-Dot probe are shown in the same diagram, but in this work, the two measurements are performed separately. A polystyrene sample was placed between two capacitor-coils to investigate magnetic field diffusion in the plastic medium.

4.2.1.2 Proton Backlighter Target

In proton deflectometry measurements in this work, protons were generated by targets which are called "proton backlighter" in this thesis. TNSA scheme (Section 4.1.3.3) for proton generation is adopted, where the proton backlighter is irradiated by all four beams of LFEX laser, having maximum intensity 1.6×10^{19} W/cm^2 which is sufficient for TNSA mechanism. The details of the proton backlighter are given as follows:

The main feature for TNSA proton acceleration is a solid thin foil, where an aluminum foil with thickness 20 μm is chosen. It is because TNSA protons from such a thickness and material were demonstrated in other experiments by the same LFEX laser. Although the good contrast of LFEX allows acceleration from much thinner foils, using too thin foils increases the risk of the thin foil surface break-out before the protons are sufficiently accelerated by the sheath electric field.

To protect the thin foil from the plasma emanated from the capacitor-coil target, the foil was mounted on an Al_2O_3 cylinder, with outer and inner diameter 2000 μm and 1000 μm respectively. A tantalum plate of thickness 50 μm was mounted on the other side of the cylinder, to shield the foil from the direct radiation from the coil component. Some main ideas of the backlighter design refer to [66].

4.2.2 Diagnostics Configuration in Target Chamber

The experiment configuration in the target chamber during a laser shot is shown in Figure 4.5. Since the configurations were almost identical between two types of shots, for simplicity they are shown in one schematic diagram.

Two capacitor-coil targets with coil diameter 500 μm were aligned in parallel to each other, with separation 500 μm and their midpoint at target chamber center (TCC), to produce a region of a relatively uniform magnetic field. The coil was aligned such that they generate the same direction of the magnetic field along the coil axis direction as indicated by the blue arrow in the diagram. As mentioned in Section 4.2.1.1, a tantalum plate of 50 μm was used for shielding purposes. Two holes of 100×600 μm were opened on the plate, which allows the coil and the connecting wires to pass through and aligned. Each of the capacitor-coil targets was irradiated by one beam of GEKKO XII laser in wavelength of 1.053 μm, without second or third harmonic generation. Also, between the two coils, a 250 μm thick polystyrene sample was placed to investigate magnetic field diffusion. Those mentioned above were the common setup of both types of shots.

For B-Dot probe measurement, the B-Dot probe was placed inside the chamber through one of the port on the Target Chamber I. From this port, the B-Dot probe was located at distance 10 cm from TCC. The B-Dot probe position was on the equatorial plane of the target chamber, which means the vertical displacement from TCC $z = 0$. The line joining TCC and B-Dot probe position makes an angle of 41.8° with the coil axis. Since the B-Dot probe only measures one direction of the magnetic field, in separate shots it was rotated 90° so that both vertical and horizontal components of the magnetic field are measured.

In this experiment, B-Dot probe measurement shots were separated from proton deflectometry measurement shots. It was because the signal produced by the real magnetic field was approximately one order smaller than the noise signal produced by the electromagnetic pulse generated by the LFEX laser shot. Therefore only GEKKO XII laser was used during the B-Dot probe measurements.

Instead of the B-Dot probe, a proton backlighter target and an RCF stack were aligned during the proton deflectometry shots. Proton backlighter was aligned such that the aluminum foil was 2 mm away from TCC, while the RCF stack was 2 cm away from TCC on the opposite side. Because of considering the remaining zero-order light feature of LFEX laser, the aluminum foil was not irradiated directly in normal, but in 41.8° instead. Nevertheless, benefited from the nature of the TNSA mechanism, the proton beam still propagates along the normal of the aluminum foil rear surface which faced toward TCC and the RCF stack behind. The deflected proton beam was then detected by the RCF stack.

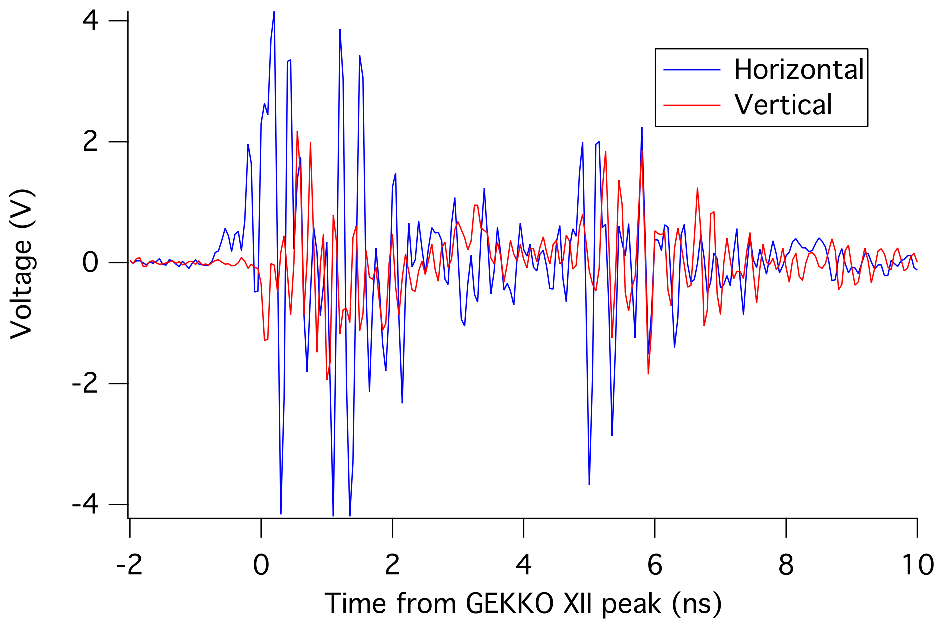

FIGURE 4.6: The raw signal collected by oscilloscope from the B-Dot probe, with the horizontal axis converted to timing relative to the GEKKO XII driving laser peak timing.

4.2.3 Experimental Results and Analysis

4.2.3.1 B-Dot Probe Measurement

B-Dot Probe measurement is a delicate process since a typical oscilloscope only allows a maximum input of r.m.s. 5 V and the maximum output voltage of the B-Dot probe is high as 1000 V. Also, the output signal has to be integrated to obtain the magnetic field amplitude, which means that a high signal-to-noise ratio is required on the oscilloscope.

The intrinsic attenuation of the experimental setup was 10 dB, that the input voltage into oscilloscope was still large. To reduce it, additional attenuators were connected to the cables. As a safety consideration, a large attenuation was added in the first try, which was 26 dB so the total initial attenuation was 36 dB. Then this value was gradually reduced and finally, the total attenuation of 23 dB was found suitable for measurement in the condition of this experiment. Under this condition, a complete set of both vertical and horizontal measurement was obtained. The raw signals collected by oscilloscope in this set of measurements are shown in Figure 4.6, with its horizontal axis converted to the timing relative to the GEKKO XII driving laser peak timing, plotted in Figure 4.7.

By inverse operation, the original output by the B-Dot probe coil is $V_{out} = 10^{(L/20)}V$, where V is signal on the oscilloscope, L is the attenuation in dB and V_{out} is the original output.

After that, the signal was being processed by a bandpass filter of 10 MHz

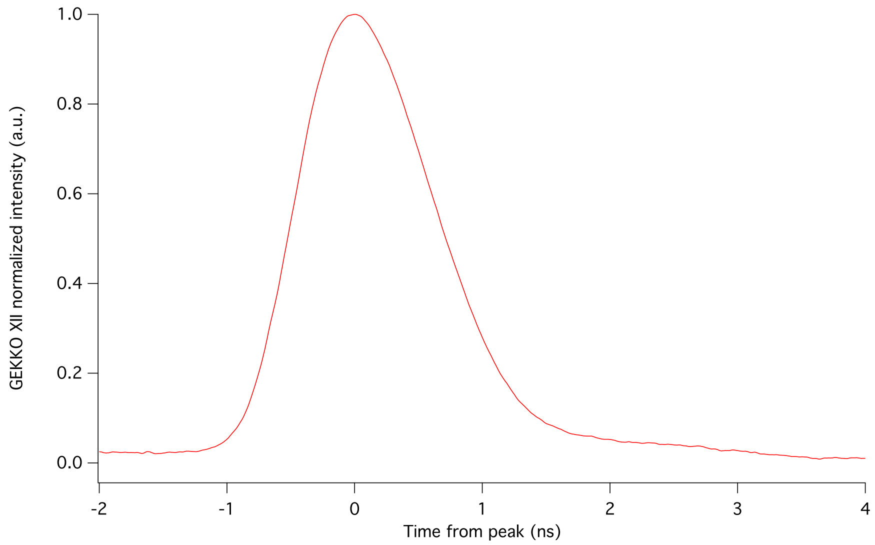

FIGURE 4.7: Time evolution of GEKKO XII intensity. Since the maximum intensity varies together with the output energy for different laser shots, the intensity is normalized.

to 1.5 GHz (3 dB point), while the loss (in dB) is plotted in Figure 4.8. The processed signal is then integrated over time. The reason for choosing 10 MHz and 1.5 GHz as parameters of the bandpass filter was the result in [23], where the lowpass filter of 1.5 GHz gave larger influence to the integrated waveform. An example of the effect by using lowpass filters of a different frequency is shown in Figure 4.9, from the horizontal signal in Figure 4.6. The peak value was almost the same, while the one using 4 GHz lowpass filter suffered from high-frequency noise by the EMP emission.

From the integrated signals, the magnetic field amplitudes at the B-Dot probe position both directions were calculated by Equation 4.2, plotted as Figure 4.10.

By 3-D magnetostatic code RADIA [68], all of the connection wires on the capacitor-coil are modeled. They were modeled precisely in the simulation, which is the key to the accurate extrapolation of the generated magnetic field. The difference between simply assuming a single circle current loop and modeling the actual capacitor-coil target was being studied in [23], in that case, the simple circle loop would extrapolate an unrealistic 25 times larger magnetic field.

By RADIA the magnetic field amplitude at the B-Dot probe position was calculated. In RADIA a current flow along the wire was modeled, which is directly proportional to the generated magnetic field at the whole space. The current could be determined by the measurement result of the B-Dot probe, and so the maximum magnetic field amplitude at the most intense magnetic field region.

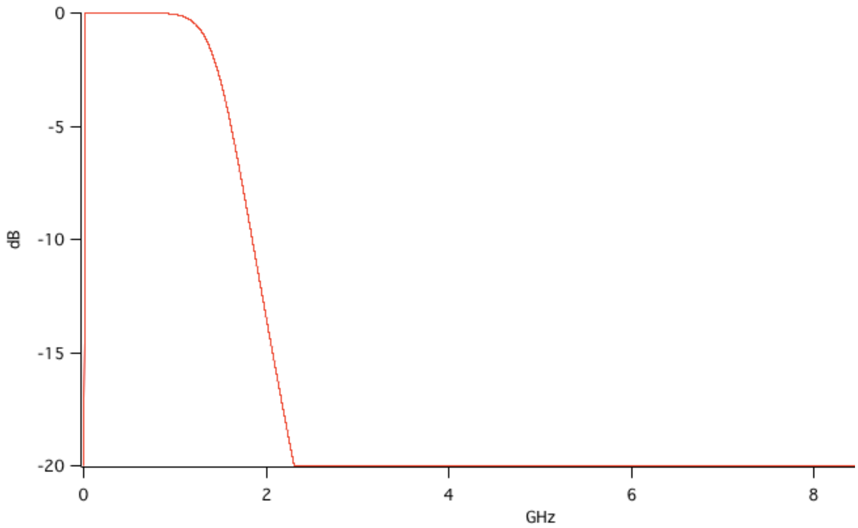

FIGURE 4.8: Plot of loss by the bandpass filter, with 3 dB points at 10 MHz and 1.5 GHz.

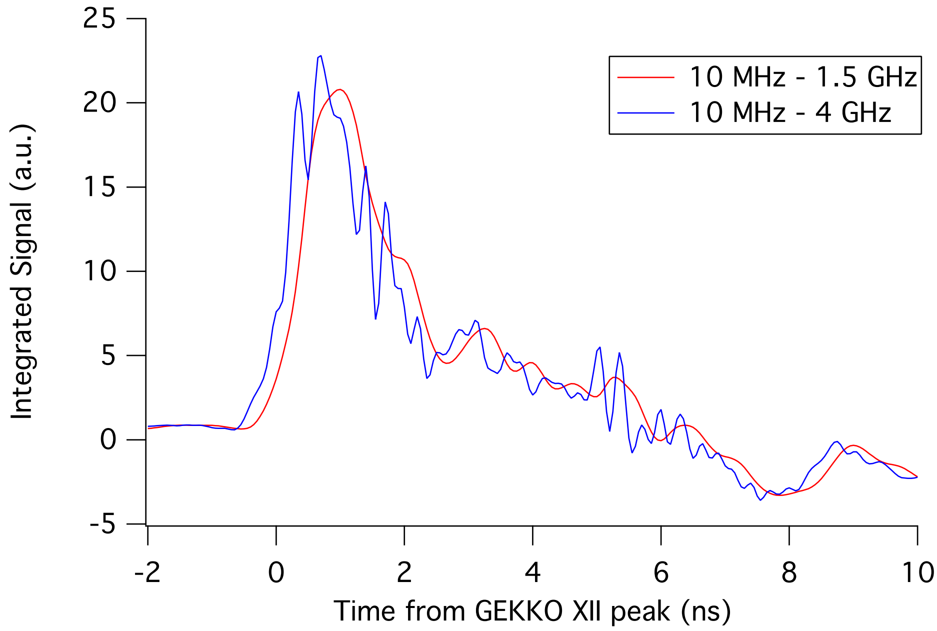

FIGURE 4.9: Integrated signal from the horizontal signal in Figure 4.6, using two different lowpass filters of 1.5 and 4 GHz. The peak value was not significantly modified, but the integrated signal of the 1.5 GHz case is free from the high-frequency noise from the EMP emission.

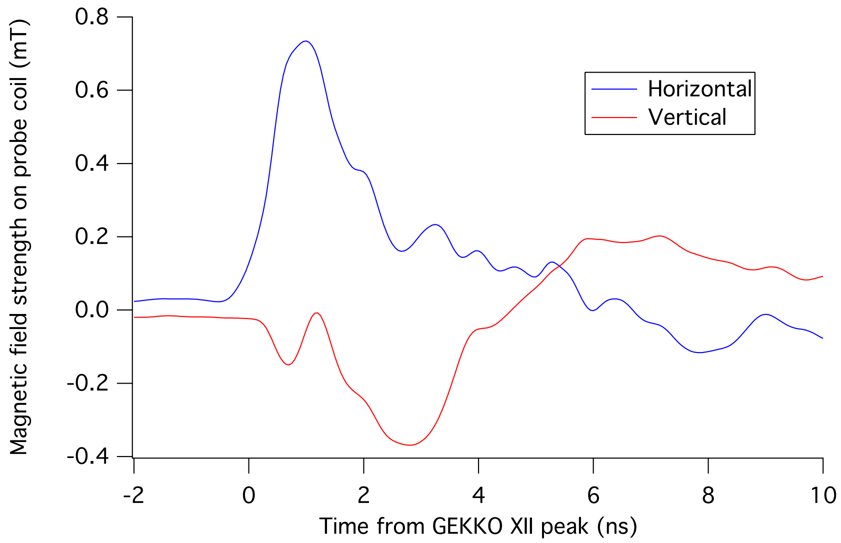

FIGURE 4.10: Time evolution of magnetic field amplitude at B-Dot probe position. Both horizontal and vertical signal of B-Dot probe processed by the bandpass filters was integrated. Magnetic field amplitudes were calculated from the integrated signals.

In this work, for a current flow of 100 kA, the calculated horizontal (tangential) and vertical component of the magnetic field at B-Dot probe were 0.400 and 0.003 mT respectively, and the corresponding magnetic field amplitude and coil center was 240 T. By this ratio, the magnetic field amplitude in the intense region was calculated only from the horizontal component and plotted in Figure 4.11. By this calculation, the estimated peak field is about 470 T, which should be underestimated when one considers also the non-zero vertical component. Because of this reason and the difference in lowpass filter frequency, the waveform was smoothened and so that the maximum value was somehow lower than the result in [67]. From this analysis, the FWHM of the magnetic field was 1.7 ns.

In the B-Dot probe measurement shots, the output energy of GEKKO XII beams for driving the capacitor-coils was 540 ± 100 J, correspond to intensity $(2.1 \pm 0.4) \times 10^{16}$ W/cm^2.

4.2.3.2 Proton Deflectometry Measurement

Before the proton deflectometry measurement, one LFEX laser shot was used to characterize the proton flux and divergence in different energy ranges, since the proton beam was not yet completely characterized by the same condition. A piece of 20 μm thick aluminum foil was placed at the same position and angle as that of the proton deflectometry measurement, irradiated by all four beams of LFEX laser, with total energy 1060 ± 90 J. An RCF stack design for such proton flux characterization was used in the shot, whose details could be referred to Appendix A.

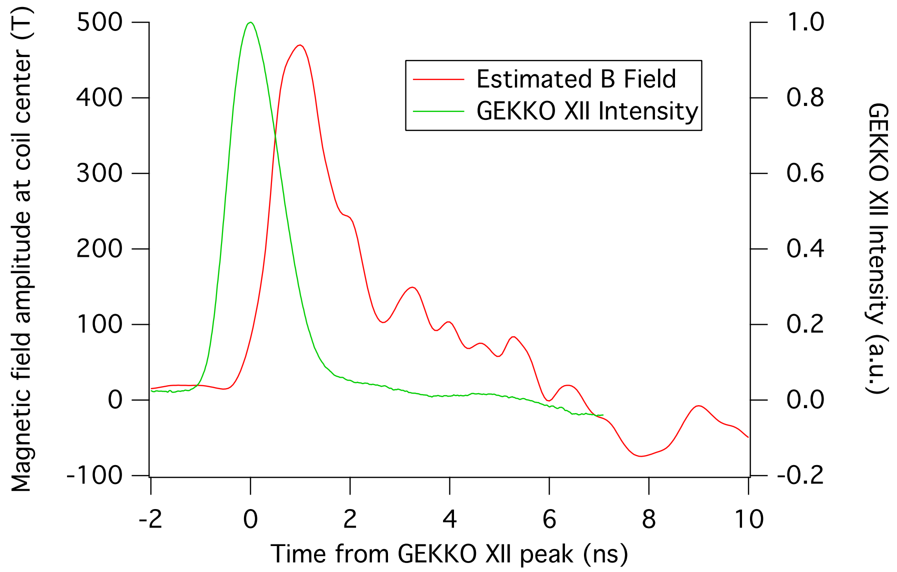

FIGURE 4.11: Time evolution of magnetic field amplitude at the centre of one of the capacitor-coil plotted together with the intensity of GEKKO XII laser intensity. The magnetic field amplitude was calculated only by the horizontal component of the B-Dot probe measurement, which is an underestimation of the magnetic field when we consider also the vertical component. In this plot, the peak is 470 T.

As a result, the maximum energy of the TNSA generated protons was measured to be 34.3 MeV. Proton flux range within different energy was obtained, which is essential for the RCF stack design for the proton deflectometry shot. Also, the divergence of the proton beam was obtained for the analysis of the proton deflectometry result described in the following paragraphs.

In the proton deflectometry measurement shot, the LFEX laser beam was driven at 1.5 ± 0.15 ns after the peak of GEKKO XII laser beam driving the capacitor-coil target. This time delay between LFEX and GEKKO XII laser beams was measured by on-shot measurement using photodiodes, also verified by on-shot scattering light measurement by an X-ray streak camera. In this shot, the energy of each driving GEKKO XII laser beam was 880 ± 50 J, correspond to intensity $(3.4 \pm 0.2) \times 10^{16}\ W/cm^2$, which was higher than that in B-Dot measurement shots.

In the two LFEX laser shots, the pulse duration, energy, and intensity on target were 1.5 ps, 1060 ± 90 J and $(1.1 \pm 0.1) \times 10^{19}\ W/cm^2$ respectively. This should be evidence of good reproductivity of TNSA proton source, that the measurement result would not become suddenly invisible on some of the laser shots as long as the laser is substantially provided stably.

Before interpreting the measurement results as proton signals, the effect of background signals has to be eliminated. Since the RCF detects ionization radiation on its active layer, not only protons but also electrons and

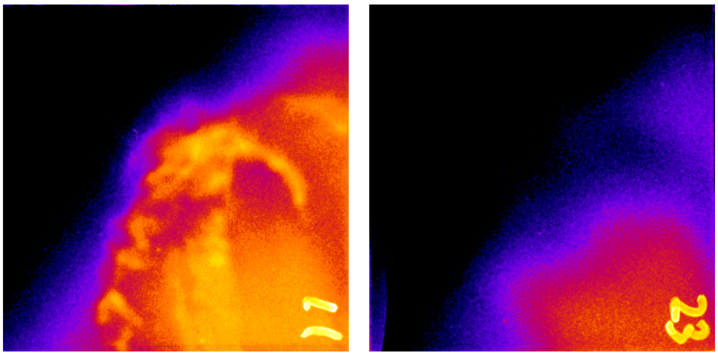

FIGURE 4.12: Signals on two RCF layers of RCF stack used in proton deflectometry shot, showing the effect of background noise produced by fast electrons. The two layers are layer 11 (Left) and 23 (Right), corresponding to the proton energy 22.3 and 28.5 MeV.

x-rays produce signals on it. X-rays generated in laser-plasma experiments are seldom highly collimated, so that background signals generated by X-rays are somehow uniform. However, fast electrons, especially those generated during the TNSA process which accounted for the proton generation, could have a relatively small angle of divergence and produce non-uniform patterns on RCF after being deflected by the intense magnetic field.

In this work, the backward RCF layers corresponding to proton energy larger than the maximum proton energy effectively provides the details of such background signals generated by the x-rays and electrons because, for the fast electrons, all RCF layers have a similar amount of deposition energy by ionization by its long stopping range. In this analysis, layer 11 was used for magnetic field amplitude analysis, while layer 23 provides the background signal for background signal elimination. The two layers correspond to proton energy 22.3 and 28.5 MeV by SRIM calculation, while the maximum detected proton energy in this shot was 23.4 MeV. On layer 11 both proton and electron signals are collected, while only electrons have deposited energy on layer 23, as shown in Figure 4.12.

When choosing the RCF layer for analysis, it is important to notice that different RCF layers correspond to proton patterns of different energy, which differ in velocity. It leads to a different time of flight from the generation point to the intense magnetic field region, which gives a time delay in addition to the delay between laser pulse. For example, in this configuration ($d = 2$ mm), for 5 MeV protons, the time of flight is about 65 ps, and for maximum energy proton 23.4 MeV, it is about 30 ps. The time difference 35 ps is even much shorter than the timing uncertainty of timing measurement, which was negligible in this work. Therefore, in this work, the RCF layer that was in the best quality for analysis could be chosen, which is the layer 11 shown in Figure 4.12. Both proton patterns, with and without the effect of the magnetic field, are shown in Figure 4.13. The electron signal on

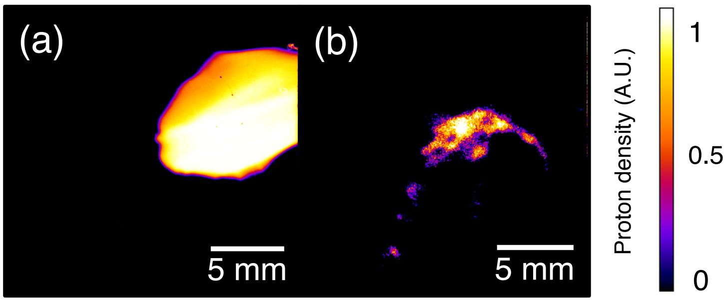

FIGURE 4.13: Proton patterns of both about 23 MeV, (a)without and (b)with the external magnetic field generated by capacitor-coil. (b) was being processed to eliminate background noise, and adjusted to suitable contrast for visibility of proton distributions.

layer 11 was eliminated by subtracting the distribution on layer 23 to obtain the proton pattern deflected by the magnetic field, shown in Figure 4.13.

To determine the magnetic field amplitude by the proton pattern obtained by RCF, Monte-Carlo simulation code combined with 3-D magnetostatic code RADIA [68] was used to simulate the proton pattern on RCF, under a magnetic field of different current strength calculated by RADIA.

In the simulation, the parameter of the probing proton source is listed as follows: Proton energy 22.7 MeV which is calculated by SRIM. The initial divergence half-angle is set 9.6°, determined by the divergence angle of 22.7 MeV protons, obtained from the corresponding RCF layer in the proton characterization shot without applying a magnetic field. Proton source's initial radius was set 25 μm, which was found to make no significant effect on simulation results compared to a point source. The current through the coil and connection wires are varied from 100 kA to 300 kA, corresponded to field amplitudes of 240 T and 730 T at one of the coil centers.

The results of simulations using a different current along the wire are shown in (b)-(e) of Figure 4.14. Also, the original proton pattern is shown in (a) which looks like a circle spot. When the magnetic field amplitude increases, the final pattern shrinks, which could be used to determine the magnetic field amplitude by the inverse approach. Some proton trajectories are plotted in (f), together with the modeled coil structure in RADIA. All protons are deflected in the z-direction indicated in the diagram, which is the effect of the most intense field generated along the coil axis. Besides that, one could observe that the direction of force F_y depends on the z-position of the proton due to the fringing field of the coil, produces the umbrella-like proton pattern.

As a quantitative method to determine the magnetic field strength, the common feature of the two peak density points on the proton pattern is connected by white dotted lines in Figure 4.14. With the integration width

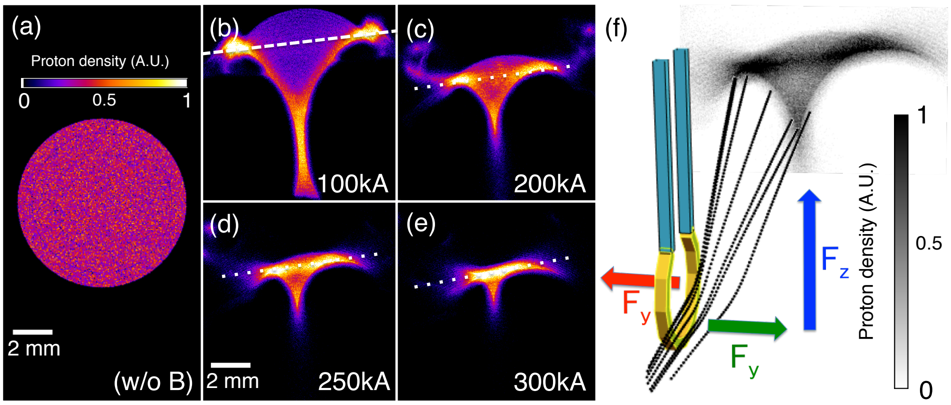

FIGURE 4.14: (From [67], the work of the author.) (a)-(e) Simulation result of proton pattern, with current (a) 0 A (without magnetic field), (b) 100 kA, (c) 200 kA, (d) 250 kA and (e) 300 kA. The white dotted line indicates the line passes through the two maximum points, which would be used in the following analysis. (f) Examples of simulated proton trajectories, drawn together with one of the coil modeled by RADIA.

0.1 mm, the proton signal distributions along the line in each simulation results are plotted in (a) of Figure 4.15, together with the experimental result in (b). From this plot, it is observed that the peak separation depends on the magnetic field amplitude, which could be used to interpret the experimental result. As the first step, from Figure 4.15 we could observe that the experimental result shows good similarity to the simulation result of current 250 kA, both the distribution plot in (a) and the actual proton pattern in (b).

After the simple arguments mentioned above, further analysis was done by plotting the separation distances in the simulation results against the magnetic field at one coil center, in Figure 4.16. It was found that a linear fitting is valid between the range of 100 and 300 kA. The experimental result is plotted in the same graph. The linear fitting equation is $y = -0.10172x + 8.863$, while the experimental separation was 2.58 ± 0.26 mm, corresponded to 618 ± 26 T by this fitting.

By the above quantitative analysis, the magnetic field was determined as 620 ± 30 T, with two significant figures.

4.2.3.3 Error Analysis of B-Dot Probe Measurement

There were some error sources in the B-Dot probe measurement with different level of significance:

- In this work, the main source of uncertainty was the effect of the magnetic field due to the Biermann battery effect at the capacitor-coil,

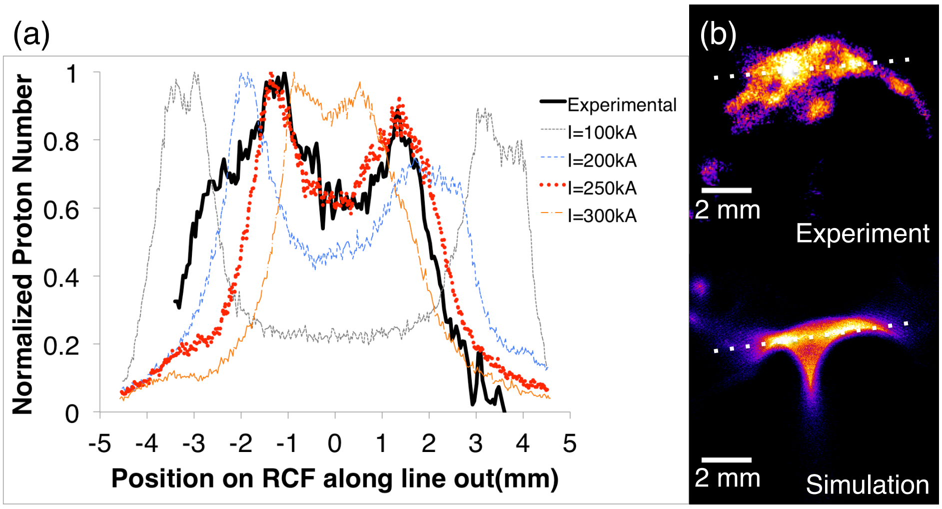

FIGURE 4.15: (From [67], the work of the author.) (a) Plot of proton distribution along the white dotted line in Figure 4.14. Also, the proton distribution in the experimental result is plotted, obtained along the white dotted line in (b). (b) Processed RCF signals obtained from the experiment and the simulation result correspond to the current 250 kA. The white dotted line is indicated on the experimental result by the same definition.

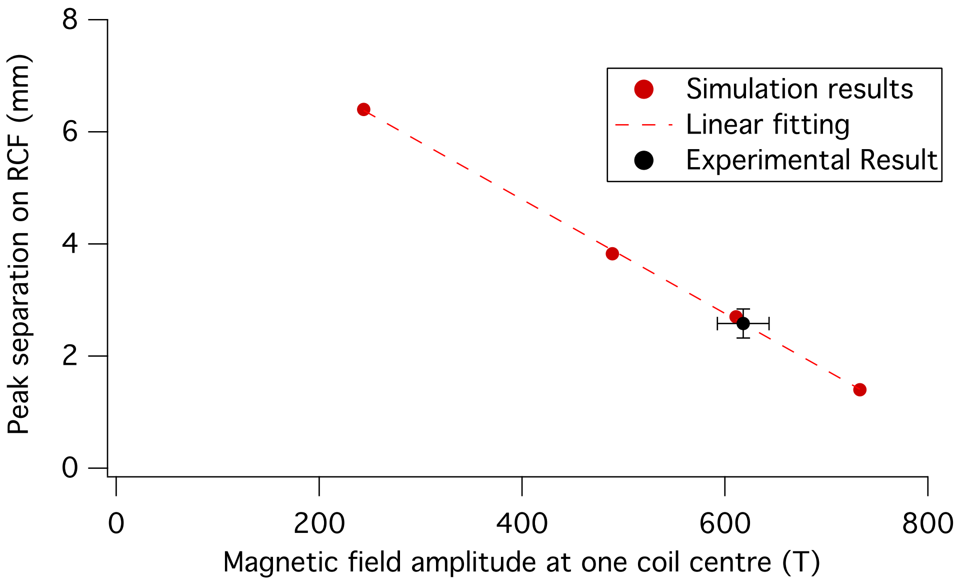

FIGURE 4.16: Plot of peak separation against magnetic field amplitude, as shown in Figure 4.15. The dotted line is the linear fitting, and the black dot indicates the experimental result together with its error bars.

which could not be studied at the same experiment due to the limited laser shots. Therefore the result in [23] was used, which was 15% of the total integrated signal.

- Alignment uncertainty was also one source of error. Practically the coil separation distance was 500 ± 100 μm, where this separation uncertainty brought uncertainty in the RADIA extrapolation process, which was in maximum 5.8% calculated by RADIA.
- Since the B-Dot Probe was inserted into the vacuum chamber externally, there was a relatively large uncertainty of probe position. This distance uncertainty was approximated to be 100 ± 5 mm. Also by RADIA, the effect of averaged magnetic flux within the finite volume of the probe and the effect of distance uncertainty were calculated together, gave an uncertainty of 10.8%.
- Background signal of oscilloscope also could be a source of uncertainty, but in this work, it only gave an uncertainty of 0.9%.
- The uncertainty of the B-Dot probe equivalence area is $< 1\%$, claimed by the manufacturer.

By considering all of the above uncertainties, the overall uncertainty of the B-Dot probe measurement was 19.4%.

4.2.3.4 Error Analysis of Proton Deflectometry Measurement

The main source of uncertainty was the uncertainty of proton energy recorded by the RCF layer, which came from two reasons: Modification of actual stopping ranges due to different incident angle against the RCF stack, and the finite width of Bragg peak that broadens with the increase of proton energy. In this work, the proton energy uncertainty at layer 11 was ± 0.9 MeV, which gave 3.9% uncertainty on proton deflectometry measurement result of magnetic field amplitude.

4.2.3.5 Comparison of the Measurement Results by Two Methods

Since the magnetic field generation scheme was identical in both measurements, it is important to compare the results of both methods. However, the output energy of each GEKKO XII beams in B-Dot probe shots and proton deflectometry shots were 540 ± 100 J and 880 ± 50 J respectively, the factor $880/540 \approx 1.63$ energy ratio have to be considered.

Assuming the same energy conversion efficiency, the magnetic field amplitude scales as the square root of laser output energy. By this simple argument, in Figure 4.17 the B-Dot probe result was scaled by a factor

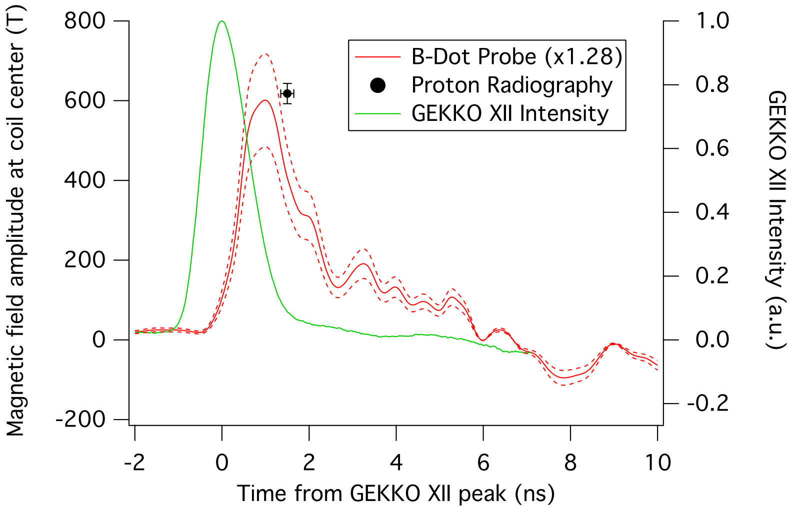

FIGURE 4.17: A plot of scaled B-Dot probe measurement result and proton deflectometry result. Dotted lines indicate the upper and lower limit of B-Dot probe uncertainty. The GEKKO XII laser intensity time evolution is also plotted for reference.

$\sqrt{1.63} \approx 1.28$, together with the proton deflectometry result. Also, the uncertainty of the B-Dot probe is indicated by two dotted lines representing the upper limit and lower limit. After scaling, the two measurements showed quite good consistency.

Chapter 5

Semirelativistic Magnetic Reconnection Experiment

In this chapter, the details of the magnetic reconnection experiment would be described. The experiment was carried out at ILE, by LFEX laser. Target design based on [24] was experimentally demonstrated and modified to produce magnetic reconnection, with magnetization in the semirelativistic regime.

In the first section, the method of producing magnetic reconnection in this experiment is explained. Details of "targets" irradiated by intense laser in the target chamber and diagnostics configuration in the experiment are described. Then the main results of this experiment are reported. The first part of the result is the characterization of the magnetic field produced by micro-coil, which became possible by the development of proton deflectometry mentioned in the previous chapter. This result is essential because magnetic field magnitude is an important parameter for magnetic reconnection, as it determines the magnetization. The second part of the result is about the measurements of the outflow jets produced from magnetic reconnection in this experiment. Spatial distribution measurement and energy distribution measurement were performed and the results are reported.

5.1 Generation of Magnetic Reconnection by Micro-coil Scheme

In this section, the principle of magnetic field generation in this work, which we call the "micro-coil" scheme, is described. The micro-coil scheme is originated by the concept of "snail target" in Korneev's work [24], introduced in Chapter 2.3.2. In this work, the snail target scheme is modified to produce a bi-directional current for magnetic reconnection. This modification was further verified by 3-dimensional PIC simulation and shown in the last part of this section.

5.1.1 Bi-directional Current Generation Scheme

From the working principle of snail target in Chapter 2.3.2, one can observe that in terms of magnetic field generated in the interior of the target, the two current flows along the target $\boldsymbol{j}_s$ and $\boldsymbol{j}_r$ can be approximated by their total effect in terms of net current $\boldsymbol{j}_s + \boldsymbol{j}_r$, which depends on the laser-induced electron vacancy. Therefore its magnetic field geometry is similar to a single-turn coil (or a solenoid for targets with sufficiently large width) when there is only one major site of electron vacancy.

The approach to creating magnetic reconnection plasma is simple: two opposite directions of current flows in the same target are produced simultaneously, by creating two major sites of electron vacancy instead of one. When the two electron vacancy sites are created at the two ends of the target, both of them would build up electric potentials and fields and therefore form net currents in two directions, among two sectors of the target.

A schematic diagram of the approach in this work is shown in Figure 5.1. Although the LFEX laser facility usually has 4 beams capability, in this experiment only two of them were available because of the facility issues. Because of the requirement of using one of the available beams simultaneously as a laser-driven proton source for magnetic field characterization, generation of magnetic reconnection by a single intense laser beam is necessary for this experiment. As the solution, the feature of moderately large focal spot size of LFEX laser was taken as an advantage to irradiate two locations on the same target (where in this work they are named "micro-coil target") at the same time.

In Figure 5.1, arrows indicate the direction of current flow induced at the two irradiation sites, which is opposite to the electron flow direction. The blue arrows indicate the surface current $\boldsymbol{j}_s$ from the direct acceleration of electrons, which always points to the opposite direction from the laser propagation. Yellow arrows indicate the return current $\boldsymbol{j}_r$, which tends to recover the neutrality which is broken by the electron accelerated away from the laser irradiation sites. As the total effect of the two types of current flows, green arrows indicate the net current $\boldsymbol{j}_s + \boldsymbol{j}_r$. As indicated by the two green arrows, two current flows in opposite directions could be generated in a single target by a single laser beam, which is required by our situation for performing a characterizable magnetic reconnection experiment.

In the next subsection, numerical simulation results are shown as verification of this scheme as producing magnetic reconnection plasmas.

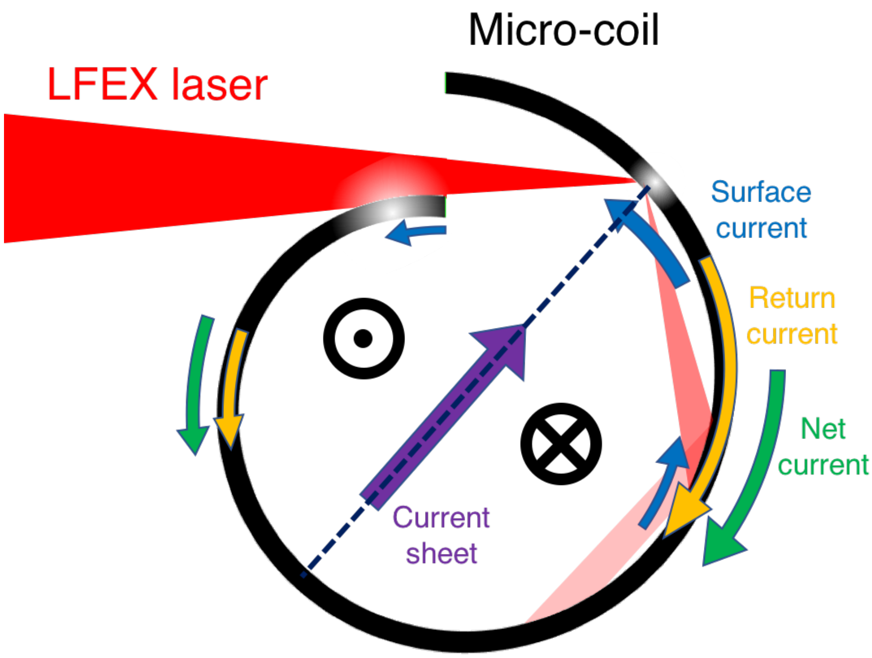

FIGURE 5.1: Schematic diagram of the two-directional current generation in the LFEX experiment. LFEX laser, with a moderately large focus spot which is comparable to the target opening size, entered and was focused on the focus spot, partially absorbed and reflected along the curved surface producing a site of electron vacancy. At the same time, a portion of incident laser irradiated on another end of the target, producing an additional electron vacancy site. As a result, two net current flows (green arrows) in opposite directions were generated in a single target, by a single laser beam.

5.1.2 Verification of Magnetic Reconnection from Bi-directional Current Generation Scheme

As an evaluation between the two schemes mentioned above, 3-dimensional PIC simulations were performed to show the differences, especially for the current generation and the existence of a magnetic reconnection. In the following paragraphs, details of PIC simulations in this work are firstly described, and after that, the comparison follows.

5.1.2.1 Details of PIC Simulations

In this work, simulation covers the detail of laser-plasma interaction, its resulting electromagnetic field, and particle dynamics, by PIC simulation code EPOCH [69]. Because of the limitation of the available computational resources, the target size in the simulation is set $1/30$ of the real target in all 3 dimensions. Also by the same reason, collisional effects are not included in the simulation.

The simulation box is in size of $12 \times 12 \times 50$ μm, corresponds to the number of cells $300 \times 300 \times 1250$ in Cartesian coordinates. Simulation cell size $\delta x = \delta y = \delta z = 40$ nm, with a single time increment $\delta t = 0.059$ fs. The cell size (and thus time resolution) is sufficient to resolve the electron and ion collisionless skin depths c/ω_{pe} and c/ω_{pi} (or plasma frequencies in terms of time resolution), which is estimated as 120 nm and 5 μm under the maximum electron and ion density $n_e = n_i = 2 \times 10^{27}$ m^{-3} obtained around the magnetic reconnection sites in simulations.

The coordinate system is defined as follows: Cross-section of the micro-coil target lie on the x-y plane, with the x-axis set to be the incident laser propagation direction. The polarization of laser is in the y-axis, which is the same as the geometrical relations in the experiment. The z-axis is the axial direction of the micro-coil as well as the main direction of reconnection magnetic field and reconnection outflow direction.

In the simulation, the micro-coil target is represented by a slab of plasma, with its shape analytically defined by the same equation as [24]:

$$r(\theta) = r_0[1 + \frac{\delta r}{r_0}\frac{\theta}{2\pi}] \tag{5.1}$$

where r is the distance on x-$y$plane from coordinates $(x, y) = (5.5, 5.5)$ μm, θ is defined in anti-clockwise direction on x-y plane where $\theta = 0$ at $+y$ direction. In this simulation, $r_0 = 3$ μm and $\delta r = 2$ μm as $1/30$ of real scale.

The cross-section of the initial plasma density profile for a micro-coil target is plotted in Figure 5.2. The plasma slab consists of two layers: An outer layer representing the bulk of the micro-coil target, and an inner layer representing the common experimental fact that practically there is always

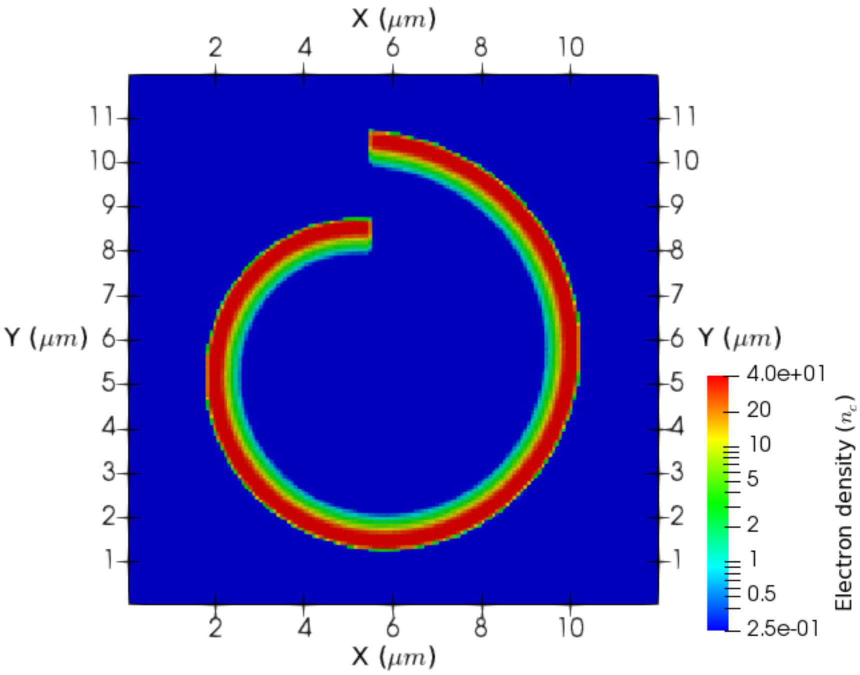

FIGURE 5.2: Cross-section of initial electron density profile in PIC Simulation for micro-coil target case, on the x-y plane. A layer of exponentially decreasing plasma is placed at the inner surface, which is an approximation based on the experimental fact of lower intensity pre-pulse producing a layer of pre-plasma on the inner surface before the main pulse arrives.

a pre-plasma layer created by low intensity, nanosecond-order pre-pulse before the main pulse arrive.

The outer surface is a layer of fully ionized copper plasma in constant density, such that the electron density $n_e = 40n_c$, where $n_c = 1.01 \times 10^{27}$ m^{-3} is the electron critical density for laser wavelength $\lambda_0 = 1.05$ μm. The corresponding ion density $n_i = 1.5 \times 10^{27}$ m^{-3}. In each cell, 1 copper ion and 29 electrons are initially placed. This choice of maximum density $40n_c$ is a conventional setting, which is sufficiently dense such that the particle dynamics does not largely deviate from the case of real solid density, as well as reducing the required computational resources. It is confirmed by the fact that the shape of the outer layer has maintained during the whole simulation.

The inner surface consists of proton plasma, instead of copper plasma, to represent the surface contamination which is the majority of pre-plasma. By numerical reason, the electron density at the boundary between inner and outer surface is set continuous, therefore the density profile of the plasma is $n_p = n_e = 40n_c \cdot e^{d/\tau}$, where d is the distance from the outer layer and $\tau = 0.1$ μm is the pre-plasma scale length. In this layer, 5 protons and 5 electrons are initially placed in each cell.

In this simulation, the real ion-electron mass ratio is used. That is, $m_p/m_e \sim 1836$ and $m_i = 63.546u$. The density profile is uniform along z-direction, with a finite length of 16.7 μm. All of the simulation boundaries ($\pm x, \pm y$ and $\pm z$) are free for outflow, while the $-x$ boundary allows the entrance of incident laser.

The incident laser has a maximum laser intensity $I_0 = 1.0 \times 10^{19}$ W/cm^2 in wavelength $\lambda_0 = 1.05$ μm. The laser intensity is spatially and temporally distributed in Gaussian, with FWHM of 1.33 μm and 1.2 ps. Peak intensity is spatially located at the center of the opening of micro-coil, and temporally $t = 0.75$ ps. Polarization is along y-direction as mentioned, which corresponds to p-polarization. It has to be remarked that the laser intensity FWHM 1.33 μm is comparable to the half-width of the micro-coil opening, which is 1 μm. This represents the scheme of the bi-directional current generation.

5.1.2.2 Comparison Between Original and Bi-direction Current Scheme

Figure 5.3 shows some PIC simulation results of the micro-coil target case. The y component of current density is shown in Figure 5.3 (a), where the bi-directional current generation in the micro-coil target could be observed from the intense currents in $-y$ direction at both ends. At the center of the simulation box an intense current in $+y$ direction has developed, which is a combination of the confined electron flow $\boldsymbol{j}_3$ and the current sheet during the magnetic reconnection process. In-plane component of magnetic field is shown in Figure 5.3 (b). Two regions with opposite directions of magnetic field are separated by the current sheet observed in (a). It is worth to remark that the most intense region of the magnetic field localized near the micro-coil instead of the current sheet, which indicates that the majority of the in-plane magnetic field is generated by the micro-coil current flow rather than the confined electron flow. Magnetic reconnection could only occur when the antiparallel magnetic field is produced by the micro-coil current flow in opposite directions and then brought to interacting with each other by magnetizing the expanding plasma from the inner surface irradiated by the incident laser beam.

As verification of magnetic reconnection occurring in this system, magnetic reconnection was traced by using a reconnection dissipation measure D_e [70]:

$$D_e = \gamma_e[\boldsymbol{j} \cdot (\boldsymbol{E} + \boldsymbol{v}_e \times \boldsymbol{B}) - \rho_c(\boldsymbol{v}_e \cdot \boldsymbol{E})] \tag{5.2}$$

where γ_e is the Lorentz factor of bulk electrons, $\boldsymbol{v}_e$ is the average velocity of electrons and ρ_c is the charge density.

This dissipation measure is a Lorentz-invariant scalar quantity, which is valid even if the bulk electrons dynamic as fluid is relativistic, by taking measurements in the electron rest frame. Although in our case $\gamma_e \sim 1$ at any location, this is a promising evaluation of the energy transfer from the magnetic field to the plasma, with validation in high-energy-density plasmas by Xu's numerical study [71].

The plot of D_e is shown in Figure 5.3 (c). In the plot, D_e is normalized by $v_{A0}B_0j_0$ as [70], with typical values of Alfv́en velocity, magnetic field and current density as $v_{A0} = 0.023c$, $B_0 = 10^4$ T and $j_0 = 10^{16}$ A/m^2 respectively. Two dissipation sites could be observed with values of D_e in order of unity, which is one order larger than the typical value ~ 0.03 in Zenitani's work.

Also, the momentum angular distribution of the outflow protons (with K.E. > 400 keV) escaped from the $-z$ boundary of the simulation box is shown in Figure 5.3 (d). A jet-like distribution centered along z-direction, which is the reconnecting magnetic field and also the expected outflow direction, is observed in this simulation.

For comparison, the shape of the plasma is modified to switch the scheme into a single current generation. The micro-coil is replaced by an "open-cylinder", which is three-quarters of a cylindrical target. In terms of equation 5.1, this is equivalent to $r_0 = 5$ μm and $\delta r = 0$ within the range of $\pi/2 < \theta < 2\pi$. By this setting, the same input laser energy would be injected into the system, while the irradiation on another end of plasma can be sufficiently suppressed.

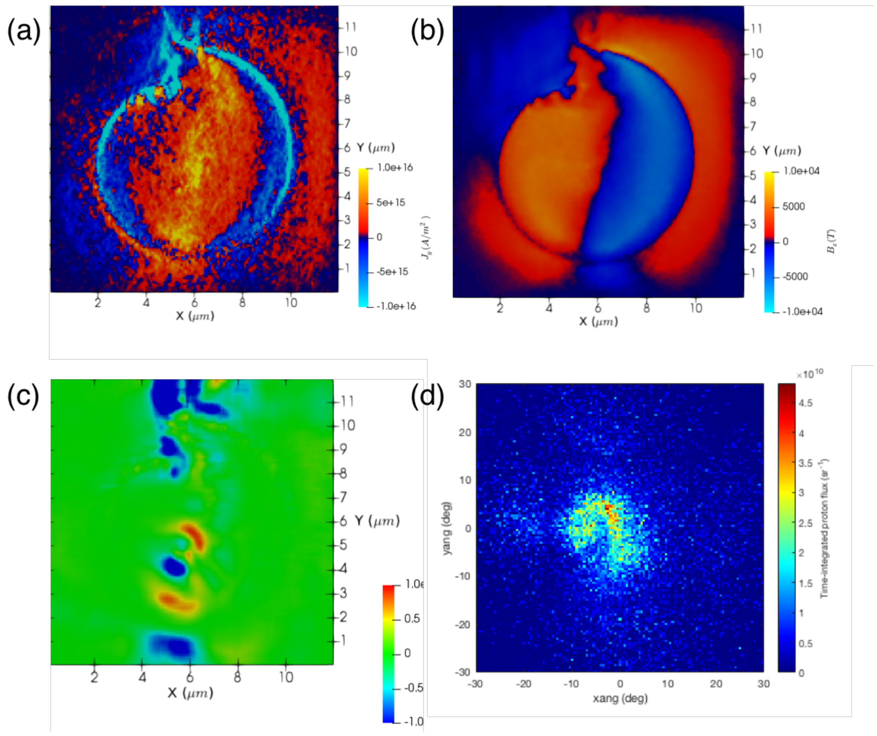

FIGURE 5.3: Simulation results in PIC simulation on micro-coil target, bi-directional current case. (a) A slice of current density J_y at $t = 1.0$ ps, in $x-y$ plane at $z = 0$ (center of simulation box). At both of the two ends of the micro-coil target, intense currents in $-y$ direction can be observed which indicates bi-directional current generation. (b) A slice of the in-plane magnetic field B_z at $t = 1.0$ ps in the same plane. (c) A slice of magnetic reconnection dissipation measure D_e at $t = 1.0$ ps in same plane. (d) A time-integrated reconnection outflow proton angular distribution, for all protons with K.E. > 400 keV. Momentum vector direction distribution of proton escaped from $-z$ boundary is plotted, while $+z$ side showed similar results. To cancel the effect of propagating laser, physical quantities are temporally averaged within a single laser period in (a)-(c). Spatial smoothing by moving average for 10 cells (0.4 μm) is performed in (c), to reduce the effect of numerical noise from PIC simulations.

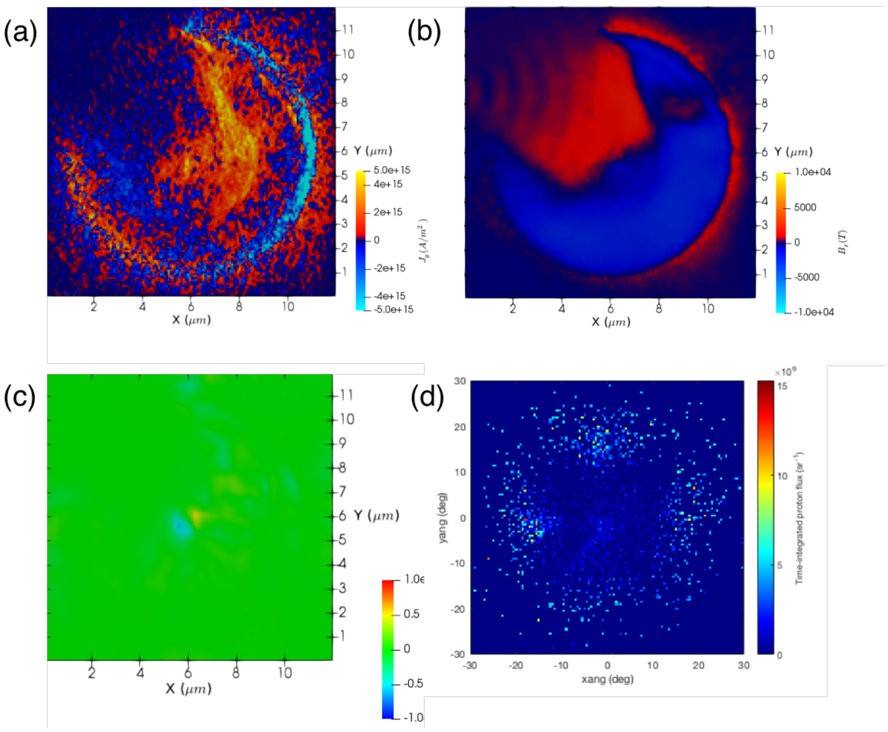

FIGURE 5.4: Simulation results in PIC simulation on the open-cylinder case, correspond to the single current case. (a) A slice of current density J_y at $t = 1.0$ ps, in $x - y$ plane at $z = 0$ (center of simulation box). Along with the bulk plasma, current flow in $-y$ direction is observed at $x > 6$ μm, while $+y$ direction current flow is observed in $x < 6$ μm. It indicates a single direction (clockwise on $x - y$ plane) current generation. (b) A slice of the in-plane magnetic field B_z at $t = 1.0$ ps in the same plane. (c) A slice of magnetic reconnection dissipation measure D_e at $t = 1.0$ ps in same plane. (d) A time-integrated reconnection outflow proton angular distribution, for all protons with K.E. > 400 keV. Simulation data is handled in the same way as Figure 5.3.

The similar simulation results for the open-cylinder case is shown in Figure 5.4. From the y component of current density J_y shown in Figure 5.4 (a), within the bulk plasma a current flow in $-y$ direction is observed at $x > 6\ \mu$m, while a $+y$ direction current flow is observed in $x < 6\ \mu$m. This confirms that a single "net current" would be generated instead of bi-directional current by preventing the irradiation on the opposite side of micro-coil. In-plane magnetic field B_z in both $\pm z$ directions still appears from Figure 5.4 (b), which is consistent with the results reported by [24]. However, without the bi-directional current generation, the $+z$ component of the in-plane magnetic field is likely to be solely generated by the confined electron flow from the irradiation site, which is not a magnetic reconnection configuration.

The lack of magnetic reconnection is confirmed by tracing the signature of a magnetic reconnection by the quantity D_e, plotted in Figure 5.4 (c). Compared with Figure 5.3 (c), the energy conversion from magnetic field energy to particle kinetic energy is greatly suppressed, which means that only the bi-directional current generation scheme could produce efficient magnetic reconnection. This is also confirmed by the reconnection outflow observed in simulation, as plotted in Figure 5.4 (d). Jet-like proton outflow is not observed in this simulation, which means that magnetic reconnection is not likely to occur.

These results confirmed, by modifying the irradiation scheme, micro-coil targets can be a tool to perform magnetic reconnection experiments. From the next section, details of the magnetic reconnection experiment are described.

5.2 Target Design

5.2.1 Micro-coil Target

Micro-coil targets are used to generate kilotesla, anti-parallel magnetic field geometry for reconnection, as the prediction by numerical simulations described in Section 5.1.1. In this work, the micro-coil target was irradiated by one beam of LFEX laser. With the introduction of a deformable mirror on that specific beamline as a facility-side improvement, the incident laser had a peak intensity of 1.4×10^{19} W/cm^2 with average energy 330 J, with a focus spot of FWHM 40 μm.

The micro-coil target was fabricated from a copper foil of thickness 10 μm one-by-one, by a rolling method with the assistance of metal wires with the same radius as the required curvature. Under the large degree of freedom in choosing the material, copper was chosen to remain the possibility to observe hot electron dynamics in the bulk of the target through observation of characteristic X-ray self-emission, because the available diagnostics are mostly specialized on the copper emission wavelength.

In terms of equation 5.1, the micro-coil target used in the experiment was designed as $r_0 = 150$ μm and $\delta r = 100$ μm. Half-width of the opening of the micro-coil target was $\delta r/2 = 50$ μm which is comparable to the FWHM of the laser intensity (40 μm), therefore the irradiation scheme should be the modified bi-directional current generation scheme. Along the rotational axis of the micro-coil target, the length of a typical target was $l = 500$ μm, while $l = 100$ μm targets were also fabricated and used in experiments.

5.2.2 Proton Backlighter Target and Grid Target

As proton deflectometry being developed in Chapter 4 was performed in this experiment, probe proton beams were accelerated by the TNSA acceleration scheme. However, in this experiment, the proton backlighter target was only irradiated by one beam of LFEX laser.

The material of the solid thin foil was chosen by comparing proton patterns produced by thin foils of different materials. Finally, aluminum foil was used in the experiment. By the same procedure, foil size of 1 mm$\times$1 mm was used instead of the smaller size of 200 μm$\times$200 μm. The thickness of the thin foil is 10 μm because the risk of the thin foil surface break-out was proved negligible before this experiment, where thin foil with thickness < 1 μm could still perform TNSA proton acceleration in experiments by LFEX laser.

In this experiment, the thin foil was irradiated before any other laser beam irradiation. Therefore protection from radiation was no longer needed, and the proton backlighter targets were simply square thin foils.

As the purpose of getting more information from the deflected proton pattern, square grids were placed between the proton backlighter target and micro-coil target in the experiment. The grids used in the experiment were G400 specifications produced by Gilder Grids, which is 400 lines per inch. The grid is made of gold, the grid pitch is 62 μm and the bar width is 25 μm, as stated by Gilder Grids.

5.3 Diagnostics Configuration in Target Chamber

5.3.1 Proton Deflectometry Measurement

The experiment configuration in the target chamber during proton deflectometry laser shots is shown in Figure 5.5. "Main target" indicates the micro-coil target, aligned at the center of the target chamber (TCC). "Foil target" indicates the proton source, which is the aluminum thin foil. It had

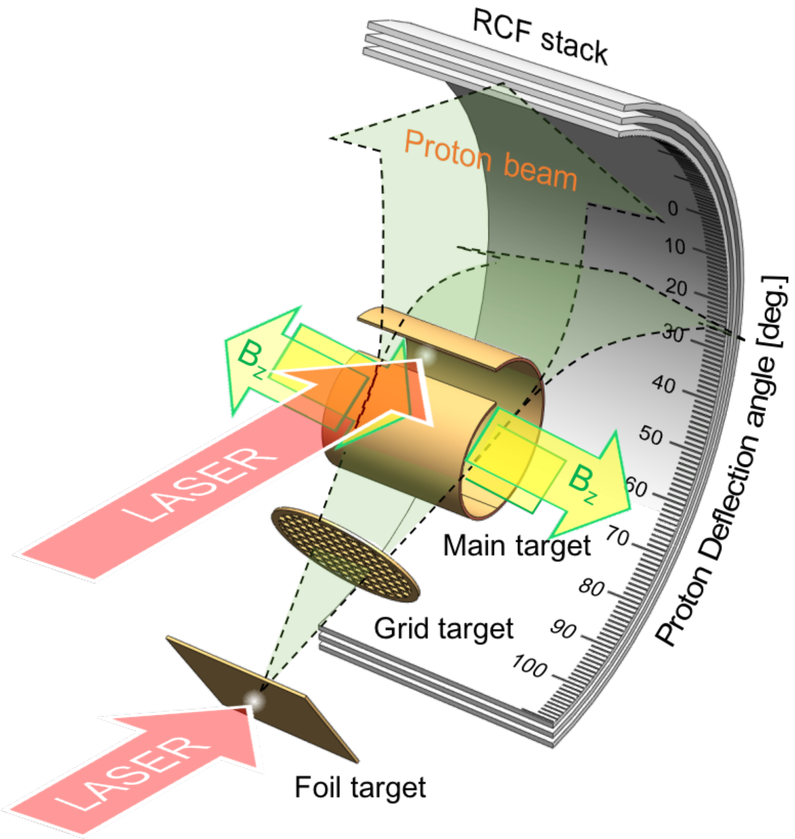

FIGURE 5.5: Experimental configuration of the proton deflectometry for characterizing the magnetic field produced by the micro-coil target.

to be positioned away from the axis of the laser focusing on the micro-coil target, and normal to the plane of the foil points towards the micro-coil target, because of the nature of TNSA that proton beam accelerates toward the normal direction. Distance from the proton backlighter to the micro-coil target was 3 mm, and the normal of the foil was inclined 30° from the horizontal axis. A grid was placed between the proton backlighter and the micro-coil target, with a distance 1 mm from the micro-coil target.

For the detection of the proton beam, RCF was also used in this experiment. Because of the possibility of a large deflection angle by the unknown intense magnetic field, a curved RCF stack with a radius of curvature 34 mm was placed 34 mm from the TCC. The RCF stack was designed to cover a large range of angles, from -100° to 150°, while 0° represents the

$+x$ direction and a positive value indicates clockwise direction on $x - y$ plane. The coordinate system is defined, such that $+x$ represents the direction of laser incidence and $+y$ represents vertically upward. The proton beam deflected by the magnetic field is then detected by the curved RCF stack.

During the laser shots, one beam of the LFEX laser was focused at the TCC, irradiating the micro-coil target to generate magnetic reconnection. Another beam was focused at the center of proton backlighter target for proton generation. The time difference between the two beams was adjustable. Also, without any prevention measures, the proton directly accelerated from the micro-coil target rear surface by TNSA would be a huge noise for proton deflectometry measurements. Very low intensity ($\sim 10^{12}$ W/cm^2) shots from the GXII laser system are irradiated on the outer surface of micro-coil targets to create a long pre-plasma. By the creation of long pre-plasma, the TNSA from micro-coil was almost suppressed and had a negligible effect on the proton deflectometry results.

5.3.2 Reconnection Outflow Jets Measurement

The experiment configuration in the target chamber during measurement of reconnection outflow jets is shown in Figure 5.6. Although two beams of LFEX laser were available, only one beam of LFEX laser was irradiated on the micro-coil target for reproducing the same experimental condition as the magnetic field characterization shots. In some shots, micro-coil targets with $l = 100$ μm were irradiated instead of the $l = 500$ μm micro-coil targets.

Several diagnostics were placed in the target chamber to measure the properties of the magnetic reconnection outflow jet. An electron spectrometer (ESM) and a Thomson parabola spectrometer (TPS) [72] were placed at the two sides of the micro-coil target as indicated. They were right on the rotational axis of the micro-coil target, which is equivalent to the inflow magnetic reconnection field direction and outflow jets direction, and perpendicular to both of the vertical axis and the laser incident direction.

In some shots, flat RCF stack of size 6 cm×5 cm was also placed at the sideway of the micro-coil target, at distance 3 cm from the micro-coil. Although in these shots the ESM or TPS behind RCF stack was not removed, they usually cannot detect any signal of particles because of the large stopping power of the RCF stack, including the supporting components.

Also in some shots, the curved RCF stack was placed to record the direct proton acceleration by the TNSA mechanism, as well as other accelerated protons from the magnetic reconnection in the radial direction (in respect of cross-section of micro-coil target). This is found essential for the characterization of the magnetic field in this work.

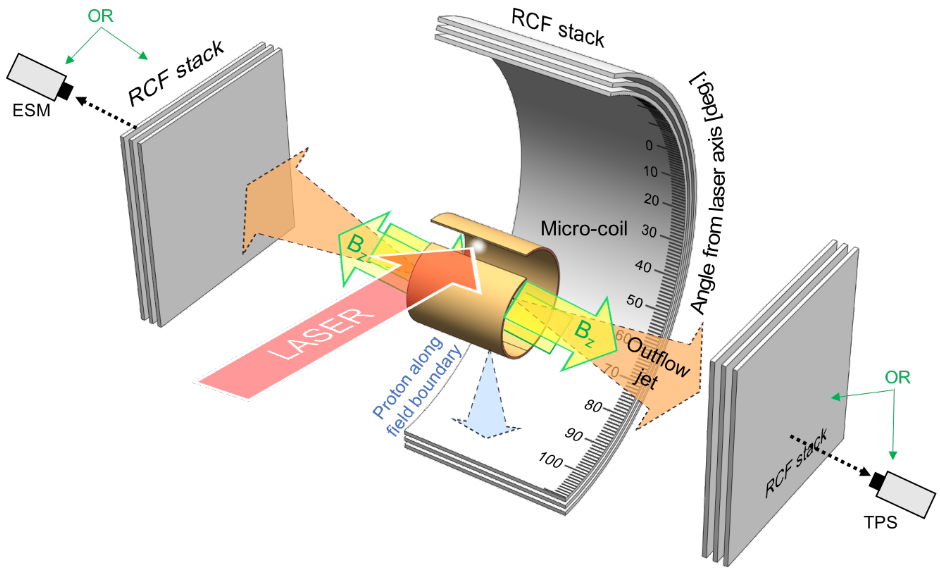

FIGURE 5.6: Experimental configuration for the measurement of outflow jets, accelerated by magnetic reconnection inside the micro-coil target.

5.4 Characterization of Magnetic Field Produced by Micro-coil Target

The magnetic field involved has to be properly characterized when performing any experimental study on magnetic reconnection. Therefore the first objective of this experiment was to characterize the magnetic field produced by the micro-coil target. In this section, the results of proton deflectometry are reported. Also, as important experimental evidence for magnetic field modeling, the measurement result of the current sheet involved in magnetic reconnection is then reported. After that, the analysis process including the modeling of magnetic field geometry is described and then the final result of magnetic field characterization is presented.

5.4.1 Measurement Result of Proton Beam Deflection

In Section 4.2.3.2 the difference of time of flight between different energy protons is mentioned, though it was negligible in that case. It is because the magnetic field duration generated by a capacitor-coil target by nanosecond order "long" pulse is also in the nanosecond order, so in the scope of 10 ps order time difference it could be considered quasi-static. Another reason is the relatively large synchronization jitter between GEKKO XII and LFEX laser, which is 150 ps. When the time difference is even smaller than such jitter, it is not meaningful to talk about such an effect of time difference. However, such uncertainty no longer exists in this experiment because of only LFEX laser involved in the proton generation and magnetic field generation.

In this experiment, one beam of LFEX laser irradiated on the micro-coil target and another one beam irradiated on the proton backlighter target, both with energy 385 J. Because of the smaller laser energy on proton backlighter target, both number and maximum K.E. of the accelerated proton beam were lower than that in Chapter 4. In this measurement, proton K.E. in the range of $4.9 - 9.9$ MeV was measured by 4 layers of RCF, while the details of the complete RCF stack design could be referred to Appendix A. As the lifetime of the magnetic field was expected in ps order, the time of flight of protons is important. Time of flight of protons from proton backlighter to micro-coil target t_{TOF} is:

$$t_{TOF} = \frac{d}{v_p} \approx \frac{d}{\sqrt{2E_p/m_p}} \tag{5.3}$$

where v_p is proton velocity for proton K.E. E_p, $d = 3$ mm is the distance and m_p is the proton mass. The approximation holds in non-relativistic limit ($E_p \ll m_p c^2 = 938.2$ MeV).

For the highest $E_p = 9.9$ MeV, $v_p = 4.355 \times 10^7$ ms^{-1} and $t_{TOF} \sim 69$ ps. Without any adjustment, the two beams of LFEX laser entered the target chamber and focused on the TCC at the same time, because they shared the same set of amplifiers and most of the beamline in equal distances, and the protons would just probe the magnetic field already evolved for tens of ps. The capability of LFEX laser allowed inter-beam timing adjustment in tens of ps, so this effect of time-of-flight could be compensated.

For the inter-beam timing adjustment, an additional factor had to be considered. The proton backlighter was placed at a position that is closer to the laser entrance in the target chamber, which caused it being irradiated slightly earlier than the micro-coil target. The difference of the distance is $\delta d = 3\cos 30° = 2.598$ mm and the time difference is $\delta t = \delta d/c = 8.7$ ps. Considering these quantities, the inter-beam timing was set that the proton backlighter LFEX beam is 60 ps earlier than the micro-coil LFEX beam, so that the highest $E_p = 9.9$ MeV protons would probe the magnetic field at the timing close to the micro-coil laser irradiation.

Proton patterns measured by the RCF stack are shown in Figure 5.7. Figure 5.7 (a) is the undeflected proton beam pattern measured in this experiment as control, where the shadow of all bars on the grid target appeared clearly. This confirms the quality of the probing proton beam which is sufficient for radiography purposes. After confirming the quality of the proton beam, the magnetic field characterization shot was performed. The proton deflection patterns recorded by RCF under the magnetic field of the micro-coil target are shown in Figure 5.7 (b)-(e). These proton patterns were

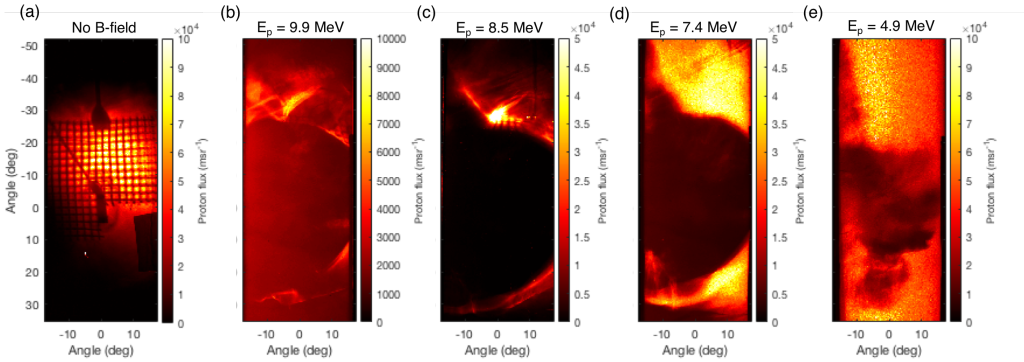

FIGURE 5.7: Proton patterns (a) without micro-coil irradiation and (b)-(e) under micro-coil irradiation. Proton patterns in (b)-(e) are measured in the same shot, in four different RCF layers corresponding to proton Bragg peak energies, indicated above each plot.

measured in a single laser shot, on four different RCF layers correspond to proton Bragg peak energies 9.9, 8.5, 7.4 and 4.9 MeV, respectively.

5.4.2 Experimental Measurement of Magnetic Field Boundary Orientation

Before the analysis of the proton deflection patterns, the measurement result by curved RCF stacks without proton backlighter irradiation is reported in this subsection.

Measurement result by curved RCF stack is shown in Figure 5.8. Figure 5.8 (a) and (b) shows the polar plot and the image of the signal of the proton flux on the curved RCF, on the RCF layer which corresponds to $E_p = 16.3$ MeV. This proton energy is higher than the maximum energy of TNSA accelerated proton beam 13.9 MeV. From $\theta = -60°$ to $-30°$ there is a region of RCF signal, which is likely the electron-induced signal by the TNSA acceleration, similar to Figure 4.12.

The important feature in this measurement is the highly collimated signal observed at $\theta = 145°$. Proton acceleration along this direction could not be explained by the TNSA mechanism and was investigated by further analysis of PIC simulation results in Chapter 5.1.2.1.

From the result of PIC simulation on micro-coil, the number of protons escaped from simulation box in $\pm x$ or $\pm y$ boundary is plotted in Figure 5.9 (a), in the same sense as Figure 5.8 (a). By plotting the slice of the in-plane magnetic field in the $x - y$ plane at different values of z in (b) and (c), it is observed that the peaks of the proton acceleration are aligned as the orientation of boundary between the regions of anti-parallel magnetic field components. Similar consistency is also found in the open-cylinder case.

Deduce from this consistency, the proton signal observed on the RCF stack reflects the magnetic field geometry. The single peak feature of the

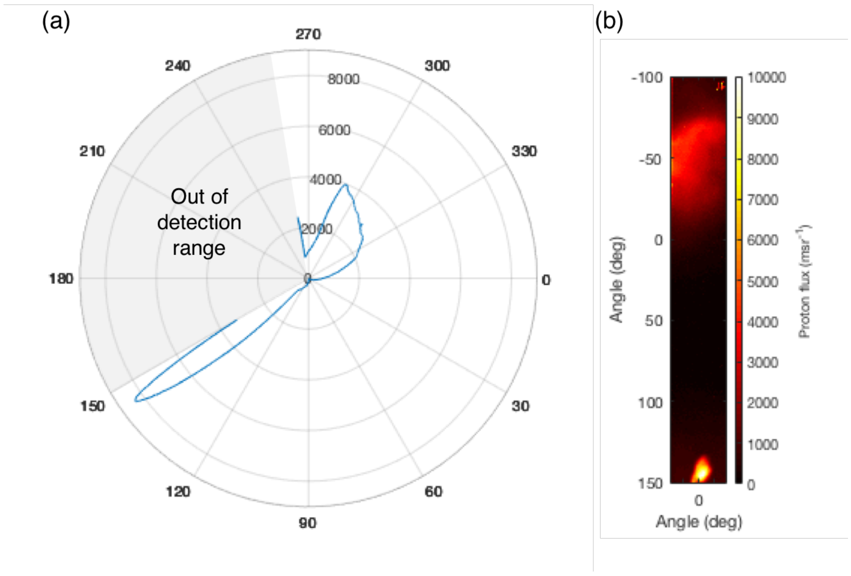

FIGURE 5.8: Angular distribution of proton accelerated from the micro-coil target, detected by curved RCF stack. (a) Polar plot of proton signal along with the curved RCF stack averaged within a transverse ($x - z$ direction in terms of PIC simulation) half-angle of $5°$ from the laser axis. (b) The RCF signal corresponds to $E_p = 16.3$ MeV, which is higher than the maximum energy of TNSA accelerated proton beam. In this laser shot, the laser was not irradiated on the proton backlighter target and therefore probing protons did not exist in this measurement.

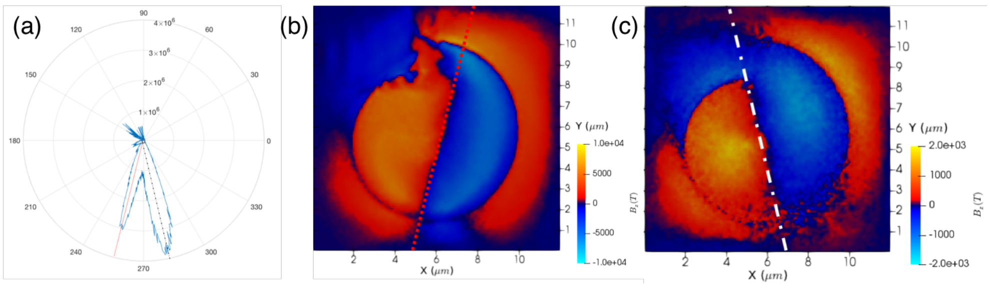

FIGURE 5.9: Angular distribution of proton accelerated from the micro-coil target and escaped from the simulation box in PIC simulation. (a) The plot of the angular distribution of proton momentum that escaped from the simulation box in $\pm x$ or $\pm y$ boundary. (b) A slice of magnetic field B_z at $t = 1.0$ ps, in $x - y$ plane at $z = 0$. (c) A slice of magnetic field B_z at $t = 1.0$ ps, in $x - y$ plane at $z = 8.3$ μm. To show the consistency between accelerated proton and magnetic field boundary, red dotted lines in (a) and (b) are plotted in the same orientation. Also, black broken line in (a) and a white broken line in (c) are in the same orientation.

proton signal indicates that the orientation of the magnetic field boundary was close to uniform along the axis of the micro-coil target.

5.4.3 Modelling of Magnetic Field Geometry

As previous work of proton deflectometry in Chapter 4.2.3.2, modeling of magnetic field geometry was necessary to perform particle tracing Monte-Carlo simulations under the magnetic field. The simulation results were then fitted to the experimental results and the magnetic field could finally be characterized.

In this experiment, the current generating magnetic field was not so straight forward, as the current flow in capacitor-coil, which was guided by the connecting wires. However, with studies by PIC simulation similar to Chapter 5.1.2.1, some key features of the system could be picked up and approximations could be made for modeling the magnetic field.

To simulate a larger spatial scale, here an additional two-dimensional PIC simulation was performed. The scale from the real target is $1/6$ instead of $1/30$, so all of the spatial scales were 5 times larger than the three-dimensional PIC simulation.

The charge density and current density sampled along with the micro-coil target in this two-dimensional PIC simulation is shown in Figure 5.10. From Figure 5.10 (a), multiple peaks in charge density are observed. The first peak is at $\theta = 30°$, which is the initial focus spot. Then the incident laser beam performs multiple reflections inside the micro-coil target and several minor electron vacancy sites appear. Although the charge distribution is localized at discrete sites, from Figure 5.10 (b) the macrostructure of the current distribution along the micro-coil target could still be observed, which is a trend of linearly decrease by increasing θ.

This feature is not only observed in a particular simulation. The same analysis was also performed on the three-dimensional PIC simulation mentioned in Chapter 5.1.2.1, with its result of current density distribution shown in Figure 5.11. These similarities show that it is appropriate to approximate the current density variation along the micro-coil as linear.

From this approximation, a magnetic field model for the characterization of the micro-coil target was constructed, as shown in Figure 5.12. It is a combination of two types of current flows, micro-coil current I_{coil} and current sheet I_{sheet}. I_{coil} represents the combination of surface acceleration electron current and return current or in other words $I_{coil} = I_s + I_r$. Although in reality they should be physically separated, their separation was negligible when considering the Lorentz force on the probing protons. I_{sheet} includes the effect of confined electron flow along the magnetic field boundary and the magnetic reconnection current sheet, which is in principle not distinguishable by proton deflectometry.

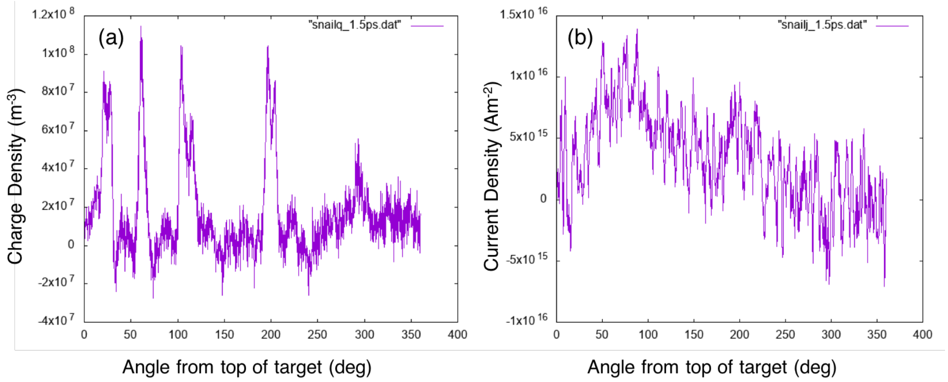

FIGURE 5.10: Distribution of charge density and tangential current density along with micro-coil target in two-dimensional PIC simulation at $t = 1.5$ ps. (a) A plot of charge density distribution along the θ direction of the micro-coil target. Multiple peaks in charge density are induced by multiple reflections of the incident laser beam which produce minor electron vacancy sites. (b) A plot of tangential current density $\boldsymbol{j} \cdot \hat{\boldsymbol{\theta}}$ along the θ direction of the micro-coil target. $\theta = 0$ is defined at the $+y$ direction, which is one end of the micro-coil target. The quantities are averaged over the initial thickness of the micro-coil target.

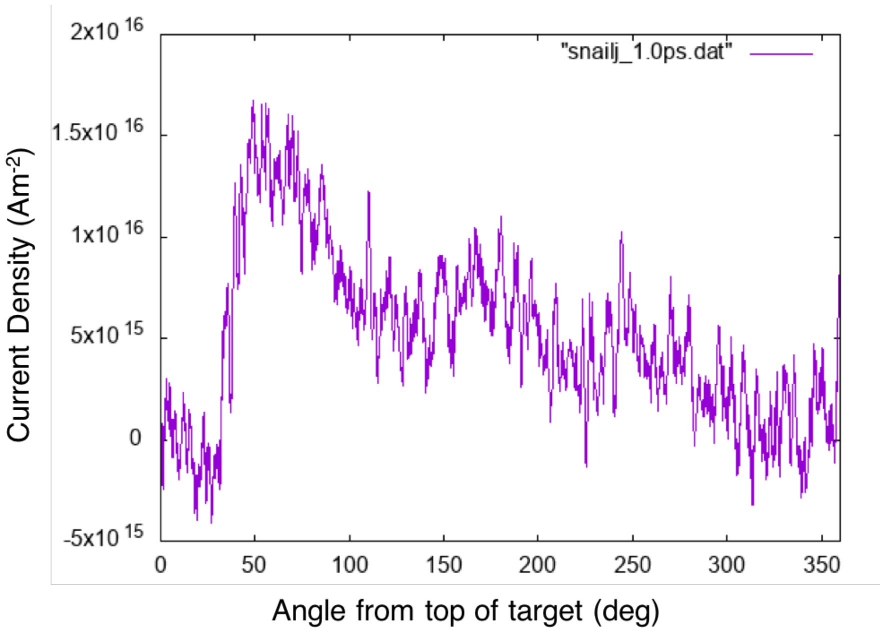

FIGURE 5.11: Distribution of tangential current density along with the micro-coil target in three-dimensional PIC simulation at $t = 1.0$ ps.

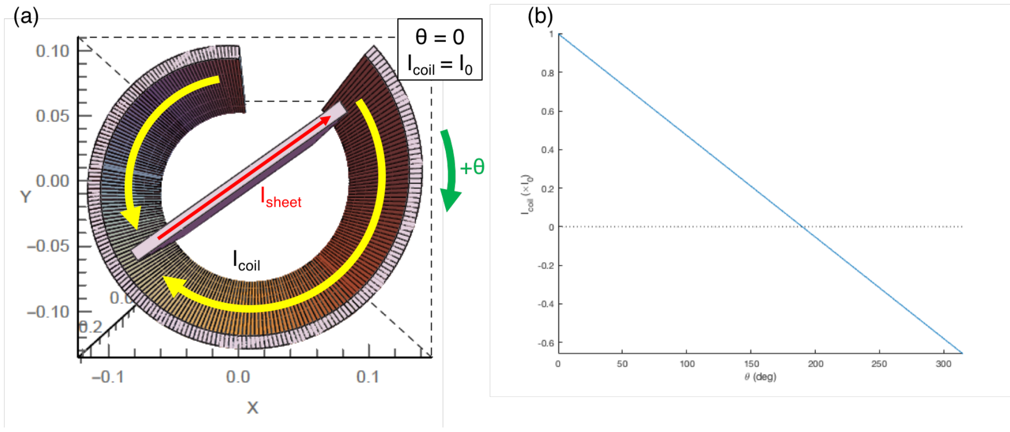

FIGURE 5.12: Schematic diagram of the current structure for modeling the magnetic field in the micro-coil target. (a) The geometry of the current structure, consisted of the micro-coil current I_{coil} and current sheet I_{sheet}. (b) A plot of the dependence of the I_{coil} on angle θ from the laser irradiation site. The current variation was approximated as linear, from value I_0 to $-0.66I_0$.

The shape of the current segments carrying I_{coil} was modeled as Equation 5.1, with $r_0 = 300\ \mu$m, $\delta r = 200\ \mu$m and length of micro-coil along axis direction as 500 μm, same as the dimension of real micro-coil targets. The distribution of the current within the micro-coil target was modeled as linear from one end to the other end, by the approximation based on the above PIC simulation results. In the two ends, the current was set I_0 and cI_0, while I_0 is the free parameter to be fitted and c is an arbitrary constant depends on the neutral point of the current flow. In this model, the current sheet was orientated such that it points to the neutral point of the micro-coil current flow ($I_{coil} = 0$). Therefore, the value of c depends on the current sheet I_{sheet} direction, which was experimentally determined as 145° from the direction of laser incidence, shown in Figure 5.8. In this analysis, $c = -0.66$.

Besides modeling the micro-coil current, the current sheet also had to be modeled. In this analysis, the current distribution was assumed constant along with the whole current sheet, in a value of aI_0 with an arbitrary constant a. It turns out that this degree of freedom of a was the major source of uncertainty in this analysis, because of the effect of I_{sheet} was opposite to the magnetic field outside of the micro-coil produced by I_{coil}.

5.4.4 Result of Magnetic Field Characterization

In this subsection, the analysis of proton deflectometry measurement is described. The procedure is similar to Chapter 4.2.3.2: Monte-Carlo simulation code combined with 3-D magnetostatic code RADIA [68] was used to simulate the proton pattern under different values of I_0, which is the free parameter of the magnetic field model that is practically a scaling factor of

TABLE 5.1: Time of flight of proton with K.E. correspond to RCF layers

RCF Layer #	Proton Energy (MeV)	Time of flight (ps)
2	2.9	69.5
3	7.4	74.9
4	8.5	80.1
5	9.9	98.3

the magnetic field. In this analysis, the value of the current sheet aI_0 also had its degree of freedom.

As shown in Figure 5.7, four RCF layers in the RCF stack measured different proton patterns for different proton energies E_p. Table A.4 in Appendix A could be referred for the full configuration of the RCF stack. Different E_p gives different time-of-flight t_{TOF} from Equation 5.3, listed in Table 5.1. Each of the proton patterns on different RCF layer probes the magnetic field around a specific timing t in ps:

$$t = t_{TOF} - 60 - 8.7 \tag{5.4}$$

where 60 ps is the time delay set between the two beams and 8.7 ps is the time difference originated from the different distance of the two laser focus spots from the target chamber laser entrance.

All of the four patterns were analyzed to obtain the value of I_0 at each corresponding t, in the same practice. For simplicity, the analysis of one proton pattern one RCF layer corresponding to $E_p = 9.9$ MeV, representing the earliest magnetic field during laser irradiation, is shown in the following.

Same as Chapter 4.2.3.2, Monte-Carlo simulations were launched to produce proton deflection patterns, scanned through a range of free parameters. In this analysis, the number of parameters to be scanned was two (I_0 and a), instead of only one in Chapter 4.2.3.2, because of the degree of freedom of the current sheet amplitude which varies the magnetic field geometry. The value of a is scanned from 0 to 1 in an increment of 0.1. For each value of a, the value of I_0 is scanned every 0.5 MA.

Simulation parameters are listed as follows: For each set of parameter, 10^5 particles are traced. Proton energy is 9.9 MeV. The initial divergence half-angle is set to 20° which was obtained in a proton characterization shot without applying a magnetic field, performed at the same experiment. Proton source radius was assumed as a point source.

A part of parameter scanning results is shown in Figure 5.13. Three rows represent different values of a from 0.1 to 0.3, while three columns represent different values of I_0 from 1.0 to 2.0 MA. From the first and second row,

$a = 0.1$ and $a = 0.2$, a void of the proton was created at the center of the proton beam, which increases in size with increasing current I_0 (thus magnetic field amplitude). However, the proton pattern was completely different for $a = 0.3$. At $a = 0.3$, the proton moving with a small angle ($< 5°$) around the proton beam center tends to collimate at the proton beam center, almost independent of the value of I_0. The simulated proton patterns were sensitive to the value of a because the magnetic field configuration outside of the micro-coil target depends on the value of a, which is the ratio between the micro-coil maximum current and the current sheet current. In the same sense, within the range $a \leq 0$ or $a \geq 0.3$, Monte-Carlo simulations showed similar results as $a = 0.3$. The experimental result, shown in Figure 5.7, with full angle $\sim 50°$ could only be reproduced within $0.1 \leq a \leq 0.2$.

Although the value of a cannot be further determined by the experiment data, one can observe that the difference between the two rows of $a = 0.1$ and $a = 0.2$ is not significant. Therefore in this work, the finite range of I_0 determined by different values of a is taken as measurement uncertainty.

To compare between simulation and experimental results, the void size is first defined in this analysis, as the FWHM of the number of proton, being averaged along half-angle $15°$ on the transverse direction (Horizontal direction on Figure 5.7 and 5.13).

From a parameter scan on I_0 at a single value of a, the relation between I_0 and void size θ_{void} (in degrees) could be fitted well by a quadratic relation:

$$\theta_{void} = c_1 I_0^2 + c_2 I_0 + c_3 \tag{5.5}$$

where c_1, c_2 and c_3 are fitting constants for every value of a.

For $a = 0.1$, the fitting parameters are $(c_1, c_2, c_3) = (-2.2, 21.46, 14.8)$. For $a = 0.2$, the fitting parameters are $(c_1, c_2, c_3) = (-1.93, 19.858, 13.945)$. From the experimental data, proton void size $\theta_{void} = 50.6°$ is obtained. By substitution and solving the quadratic equations, $I_0 = 2.14$ MA when $a = 0.1$, and $I_0 = 2.41$ MA when $a = 0.2$. As the result, the variation of I_0 is within 10% and is considered as one source of uncertainty.

The two magnetic field maps for $a = 0.1$ and $a = 0.2$ and their corresponding value of I_0 are plotted in Figure 5.14. The maximum magnetic field in these two cases is 1965 T and 2218 T respectively, where their mean value 2.09 kT is taken as the determined value in this analysis, with $< 10\%$ of uncertainty by the degree of freedom on a.

A similar analysis was done on all of the four proton patterns. The time evolution of the micro-coil magnetic field is shown in Figure 5.15, where the detail of error bars is provided in the next subsection. It should be noted that the magnetic field was weaker in later timing, despite the similar void

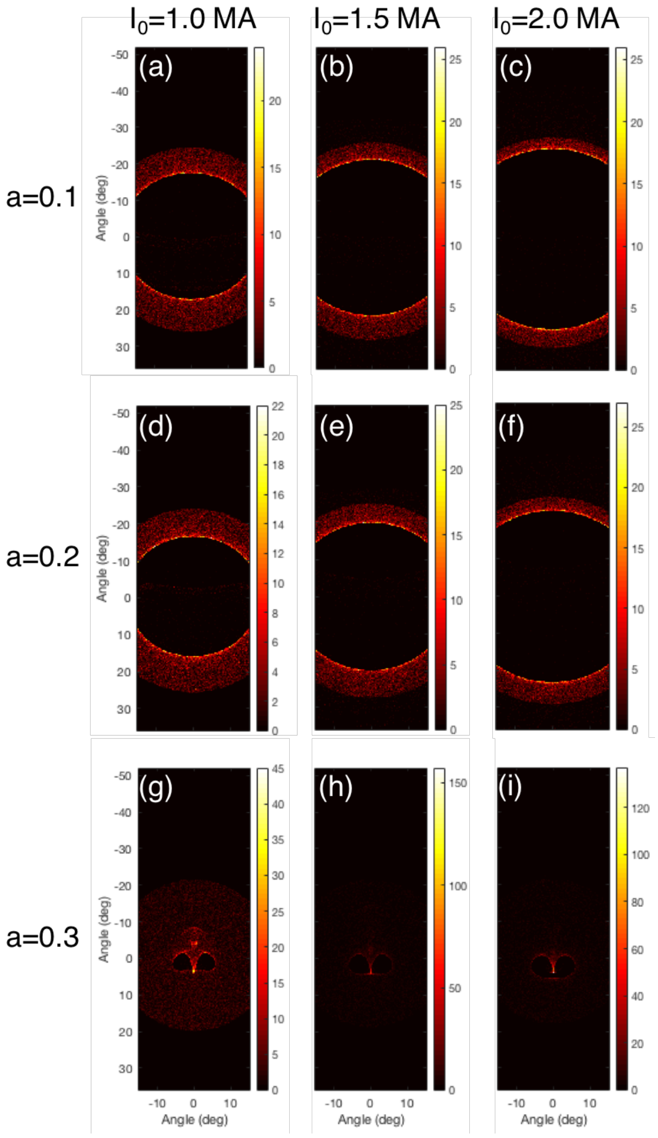

FIGURE 5.13: A selection of Monte-Carlo simulation results to show the trend of proton patterns. Three rows represent different values of a from 0.1 to 0.3, while three columns represent different values of I_0 from 1.0 to 2.0 MA.

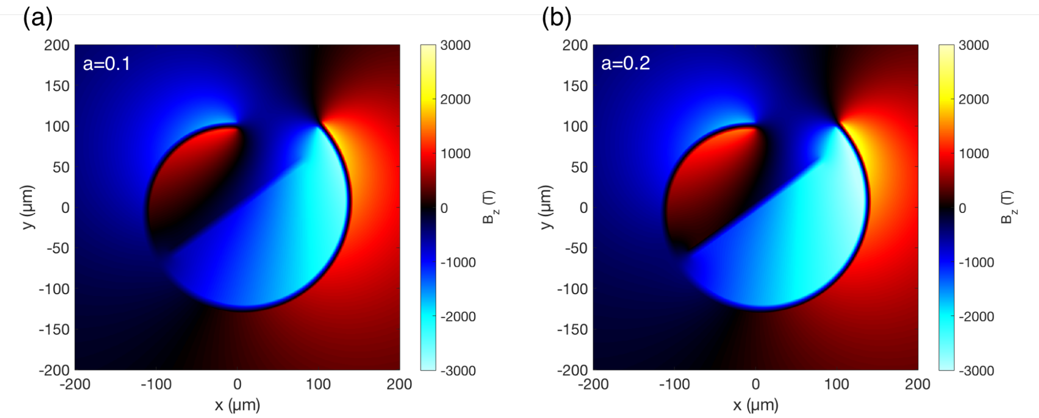

FIGURE 5.14: Modelled in-plane magnetic field B_z maps from the results of magnetic field measurement analysis, sliced at the center of micro-coil target. (a) Plot of B_z when $a = 0.1$, $I_0 = 2.14$ MA. (b) Plot of B_z when $a = 0.2$, $I_0 = 2.41$ MA.

size appeared in the proton beam. It is because, for the later time measurement, the K.E. of the proton is lower (larger t_{TOF} for approaching the micro-coil target later in time), which should be deflected in the same sense with a weaker magnetic field. The measured magnetic field was strongest at the first measurement of $t = 0.5$ ps, which is $2.09^{2.10}_{-0.13}$ kT. The magnetic field decayed into about a quarter, 536 ± 30 T at $t = 29.3$ ps.

5.4.5 Error Analysis of Magnetic Field Characterization

In this subsection, the evaluation of experimental uncertainty is described. As mentioned in the previous subsection, there was a degree of freedom for a which could not be determined, is a source of uncertainty. However, this was not the only source of uncertainty.

By simple estimation, when the velocity of the proton is in the order of $0.1c \sim 3 \times 10^7$ ms^{-1}, it requires a finite time to travel through the micro-coil target which is not negligible. As the diameter of the micro-coil target is about 300 μm, the total travel time through this distance is in 10 ps order. This requires an additional treatment on all data points of $t < 10$ ps, because of the nature of particle tracing simulation that the particle is assumed to be affected by the magnetic field from the beginning of the simulation, which is different from the reality. In the experiment, the 8.5 and 9.9 MeV protons already approached or even entered the micro-coil target when the magnetic field is generated by the current flows. Therefore the deflection effect should be experimentally smaller than simulation prediction, results in an underestimation of the magnetic field amplitude in this analysis. The uncertainty on the first two data points ($t = 0.5, 5.4$ ps) due to

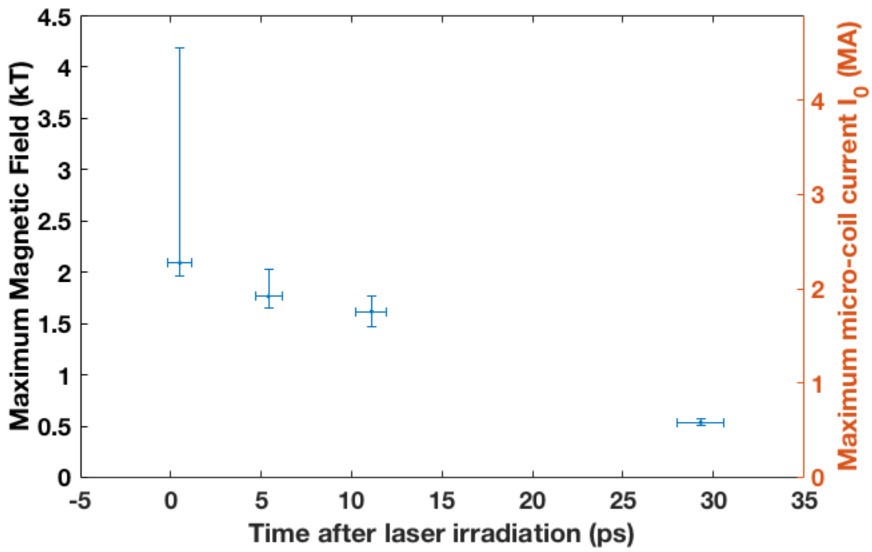

FIGURE 5.15: Modelled in-plane magnetic field B_z maps from the results of magnetic field measurement analysis, sliced at the center of micro-coil target. (a) Plot of B_z when $a = 0.1$, $I_0 = 2.14$ MA. (b) Plot of B_z when $a = 0.2$, $I_0 = 2.41$ MA.

this underestimation is estimated as 50% and 10% respectively leads to the larger upper uncertainty in the plot.

Temporal uncertainty is also indicated as error bars in the horizontal direction on the plot. During the calculation of proton energy that the Bragg peak locates at the RCF active layer, the value of uncertainty is typically 0.1 MeV. The uncertainty of t_{TOF} was calculated from this energy uncertainty, which is equivalent to the uncertainty of t.

5.5 Measurement of Magnetic Reconnection Outflow Jets

After the magnetic field characterization shots, laser shots were allocated for magnetic reconnection experiments. At the two directions of the magnetic reconnection outflow, RCF and particle spectrometers were positioned to measure the spatial distribution and particle energy spectrum of outflow jets. From RCF measurements, a pair of highly symmetric jets were accelerated along two sides of the micro-coil target are observed. From spectrometers, electron spectrum which has a significant non-thermal component was observed, which is consistent with a power-law distribution with a super-exponential cut-off. Also, the high-energy tail of the proton spectrum is observed, which follows a power-law.

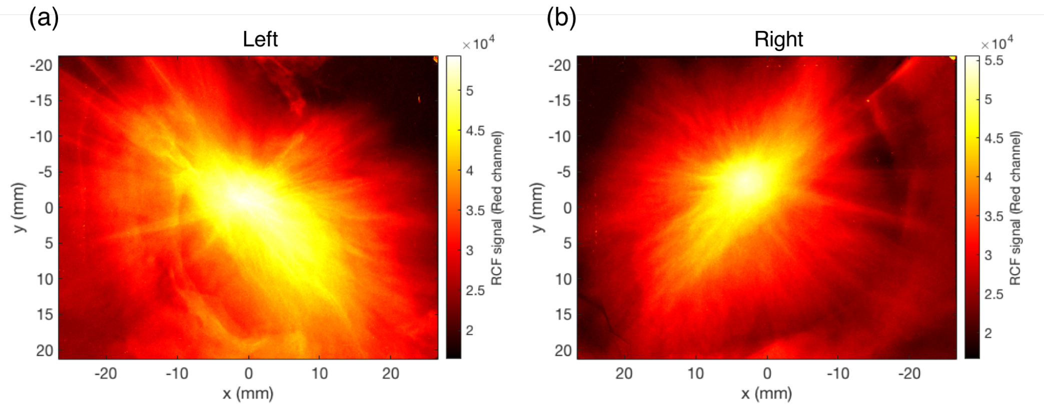

FIGURE 5.16: A plot of RCF signals which indicates reconnection outflow detected at both sides of the micro-coil target at a single shot. The RCF layer corresponds to $E_p = 4.7$ MeV is shown in this figure. (a) is recorded on the "left-hand side" and (b) is recorded on the "right-hand side" from the sight of incident laser direction, correspond to $-z$ and $+z$ direction respectively, in terms of the PIC simulation in this work. Both of the RCF signals are shown from the sight of the micro-coil target, so the x-axis direction is reversed in (b) for consistency with coordinates in PIC simulation.

5.5.1 Spatial Distribution Measurement Results by RCF

Under laser irradiation with energy 338 J on micro-coil target, from the two ends along its axis direction, RCF stacks detected a pair of symmetric proton jets as shown in Figure 5.16. Maximum K.E. of protons in the jets was 6.7 MeV, while in the figure 4.7 MeV protons are plotted. This symmetric and collimated feature was not observed in any previous thin foil radiation, from the sideway of the target. Therefore these jets were interpreted as a typical magnetic reconnection outflow. This interpretation was also verified by the comparison of simulation results shown in Figure 5.3 and 5.4, showed that the origin of the jets is particle acceleration from magnetic reconnection.

In another laser shot with energy 323 J on micro-coil target, magnetic reconnection outflow from the micro-coil target with a shorter length $l = 100$ μm (instead of $l = 500$ μm) was observed by RCF stack placed at one side. From the last penetrated RCF layer, the maximum energy of the proton in the outflow jet was about 19.6 MeV. The signal detected on RCF is shown at Figure 5.17. The outflow did not peak at the axial direction but instead, showed a ring-like structure.

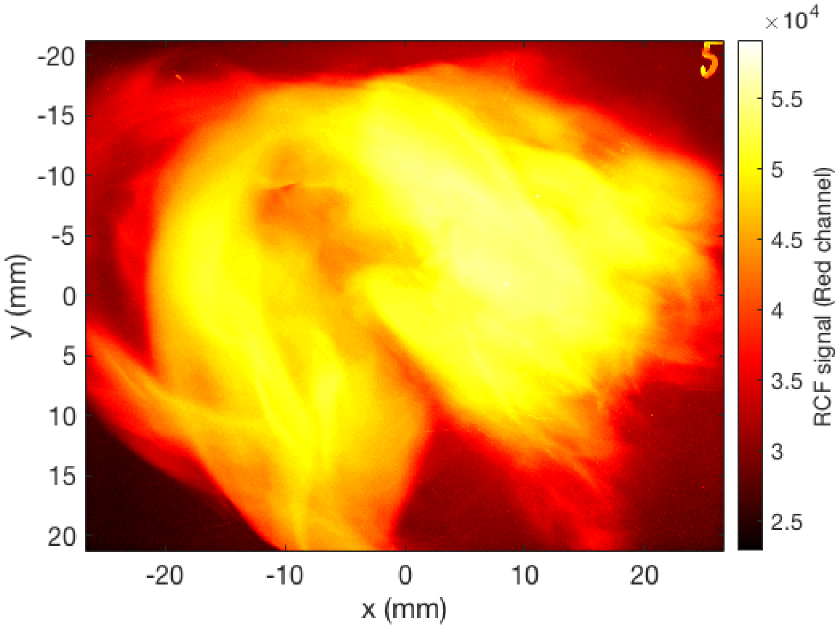

FIGURE 5.17: A plot of the spatial distribution of reconnection outflow by RCF stack, at one side of $l = 100\ \mu$m micro-coil target. RCF layer correspond to $E_p = 11.7$ MeV is shown in this figure.

5.5.2 Particle Energy Spectra Measurement Results by Spectrometers

In respect to the sight from the laser propagation direction, an electron spectrometer was positioned on the left-hand side and a Thomson parabola spectrometer was positioned on the right-hand side of the micro-coil target. In the experiment, when there was no RCF stack positioned between the spectrometer and the micro-coil target, accelerated particles entered these detectors and the electron/ion energy spectrum was measured. Compared to the RCF stack (about 2.4 sr), only particles within a very small solid angle were detected: 1.02 μsr for electron spectrometer and 0.155 μsr for Thomson parabola spectrometer.

For Thomson parabola spectrometer, there was a limitation that the lowest detectable proton energy was 6 MeV. According to the estimated maximum proton energy $E_p = 6.7$ MeV obtained in the previous section, the particle acceleration from $l = 500\ \mu$m could not be properly measured by this diagnostics. Therefore, in this section, the particle energy spectra were measured on shorter micro-coil targets that $l = 100\ \mu$m. It was observed from PIC simulations that, the maximum magnetic field inside the shorter micro-coil target is similar to the longer one, which should experimentally give a similar magnetization as measured from the longer micro-coil target.

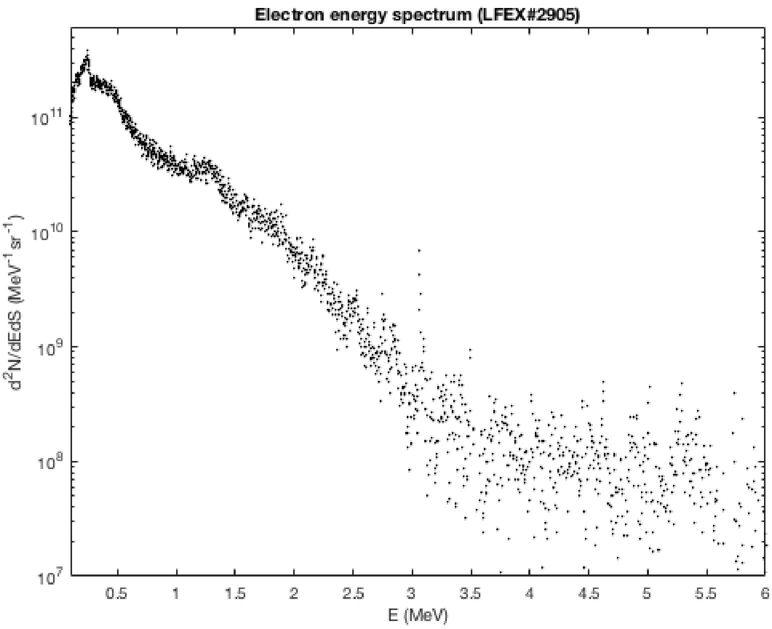

FIGURE 5.18: Electron energy spectrum in reconnection outflow jet measured by electron spectrometer.

Under a laser shot with energy 323 J, the measurement data of electron energy spectrum measured by electron spectrometer is shown in Figure 5.18, where the error bar is omitted for visibility.

Uncertainty of the electron spectrometer was already evaluated in previous studies[73]. There was a $\pm 4.5\%$ uncertainty on electron energy due to calibration uncertainty and a $\pm 5\%$ electron number uncertainty due to detector (Imaging plates) response uncertainty for electrons. With these uncertainties accounted, the electron spectrum was shown in Figure 5.19. Still, for visibility, only one of every ten data points is plotted.

Under a laser shot with energy 232 J, the measurement data of the proton energy spectrum measured by Thomson parabola spectrometer is shown in Figure 5.20. By plotting in the log-log scale, it could be observed that the proton spectrum distributed in power-law, which would appear linearly in such scale. Discussions about such power-law distributions on both electrons and protons follow in the next chapter.

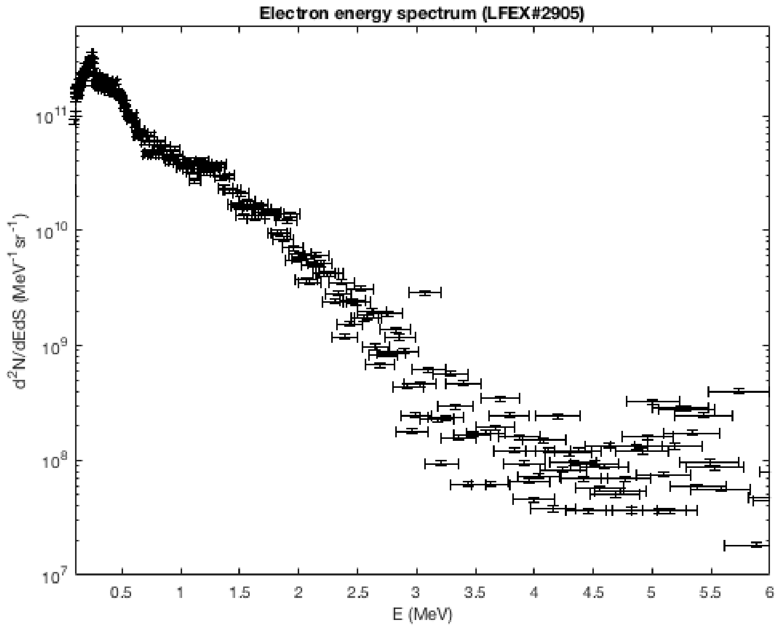

FIGURE 5.19: The electron energy spectrum in reconnection outflow jet measured by electron spectrometer plotted together with the uncertainties. For visibility, only one of every ten data points is plotted.

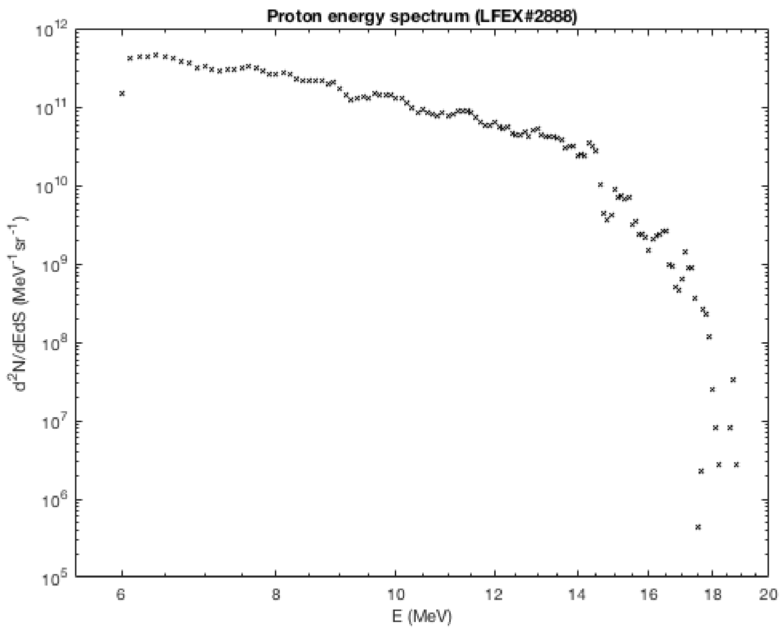

FIGURE 5.20: Proton energy spectrum in reconnection outflow jet measured by Thomson parabola spectrometer. The maximum energy of protons is about 18 MeV, consistent with the estimated maximum energy from RCF measurements.

Chapter 6

Discussions and Connection with Astrophysics

In Chapter 5, most of the details of the author's experimental work on a magnetic reconnection experiment are reported. In this chapter, the significance of the results in this experiment is presented: In the first section, the important physical parameters in the magnetic reconnection experiment would be discussed in detail. Despite some parameters were estimated by numerical study, it comes out that the magnetic reconnection observed should be in the semi-relativistic regime. Then, the outflow jet spectrum is discussed, especially on its high energy non-thermal component. Power-law distribution with different spectral slope agreed with both electron and proton spectrum, and the electron spectrum consistent well when including a super-exponential cutoff, theoretically predicted in a small system scale. Finally, the connection of the result with astrophysics is discussed. Discussions are focused on accretion disk corona of a black hole, as it shares a similar degree of magnetization which is in the semi-relativistic regime.

6.1 Physical Parameters in Micro-coil Magnetic Reconnection Experiment

By proton deflectometry measurement, the magnetic field produced in the micro-coil target was experimentally determined. Although it could not resolve the fine structure of the magnetic field around the reconnection region, the reconnection magnetic field was ensured to be in 10^3 T order. However, there were some other physical parameters not being measured, which have to be estimated in sufficient accuracy. For evaluating the particle species (electron or proton) magnetization, the number density of particle species is necessary. Also, the electron temperature is important to estimate the beta value and the dynamic effect on electron magnetization. Within the relativistic regime, the Alfv́en velocity could be calculated by the particle magnetization.

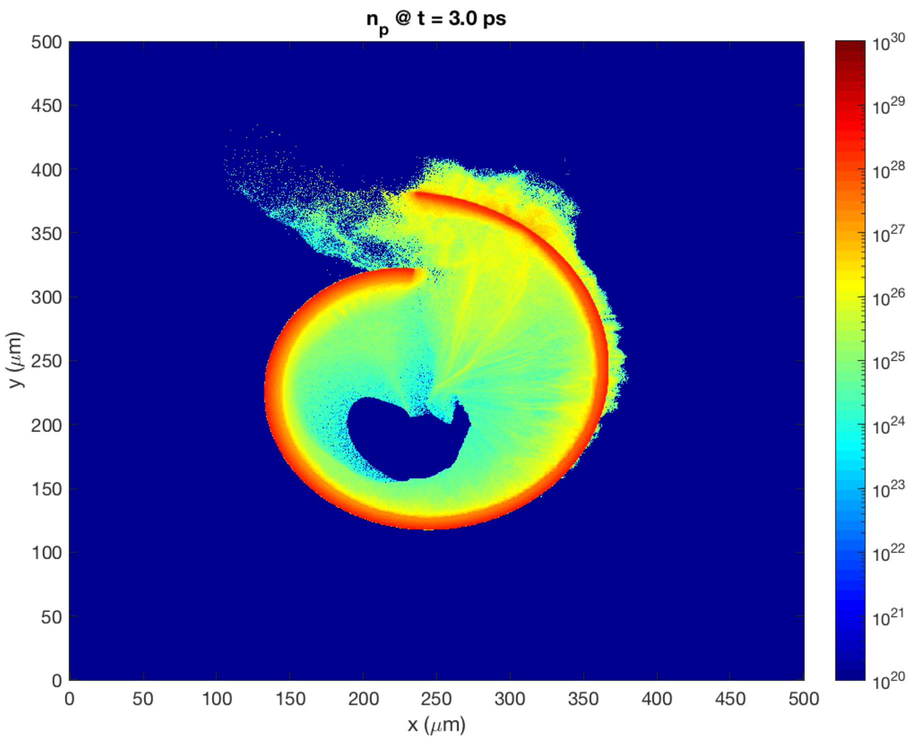

FIGURE 6.1: Proton density profile at $t = 3.0$ ps in real scale two-dimensional PIC simulation.

The particle number density was estimated from a two-dimensional PIC simulation, performed on a real scale. The simulation condition is the same with the three-dimensional PIC simulation, except all of the spatial scales are multiplied by 30. Without the z-direction, the magnetic reconnection could not produce an effective outflow and therefore particle will pile up at the interaction site. Therefore, particle number density is inspected at a time just before the plasma inflow collides. It is shown at Figure 6.1, where some region is filled with expanding plasma not yet performing any interactions with other parts of plasma. Plasma front of such plasma would initiate the magnetic reconnection in reality, and its density is in the range $(1-2) \times 10^{24}$ m^{-3}.

Then, another two-dimensional PIC simulation was performed on the same scale as the three-dimensional simulation, and the particle density inside the micro-coil in two cases was compared. In the two-dimensional simulation the average particle density is about 2×10^{27} m^{-3}, while it is about 1×10^{27} m^{-3} in three-dimensional simulation, at $t = 1.0$ ps. Therefore a factor of 2 should be included in the estimation, as the effect of dimensionality. As an order of estimation, the electron density and proton density in the experiment were estimated as $10^{23} - 10^{24}$ m^{-3}. (Assumed $n_e = n_p$.)

Recently an experimental study on similar targets, but irradiated by "long" nanosecond duration laser pulse was performed[74]. In that study, the electron density filled in the target ranged over $10^{24} - 10^{25}$ m^{-3}, which is one order denser than our estimation. However, it should be reasonable, when we consider the lower expansion velocity from the lower laser intensity in that case.

Also, from PIC simulation the electron temperature T_e is observed from $10^9 - 10^{10}$ K, or from 100 keV to 1 MeV. It is likely to be underestimated in a factor of 2 to 3, which is always observed from the difference between collisionless and collisional PIC simulations. Here we refer to the ponderomotive electron temperature, a typical scale of temperature in a high-energy-density plasma irradiated by intense laser: For laser intensity $I_L = 10^{19}$ W/cm^2, the ponderomotive electron temperature is 1.035 MeV, or $\sim 10^{10}$ K. Therefore we could say the estimation of electron temperature as $10^9 - 10^{10}$ K, with the higher limit 10^{10} K for the lowest density plasma expansion front, should be a reasonable estimation.

By Equation 3.8, $\sigma_e \sim 20 - 200$ and therefore $\sigma_p < 1$, when we take $B = 2.1 \times 10^3$ T. It is safe enough to say that the magnetic reconnection in this experiment is in semi-relativistic regime. Beta value of the system is $\beta = (nk_BT)/[B^2/(2\mu_0)] \sim 0.08$ for $n = 10^{24}$ m^{-3} and $T = 10^{10}$ K, which is magnetic dominant.

6.2 Power-law Non-thermal Particle Acceleration Observed in Experiment

The previous section showed that the magnetic reconnection in the experiment was in the semi-relativistic scheme. As mentioned in Chapter 3.2.3, recent studies theoretically showed that non-thermal component could be found even in reconnection outflow of the semi-relativistic scheme. In this section, the electron and proton energy spectra measurement results are revisited and inspected in terms of a power-law distribution.

The electron energy spectrum is plotted with different fitting in Figure 6.2. Since the lower limit of detection (~ 100 keV) is sufficient to cover the thermal component, the lower energy part of the electron spectrum is fitted by a Maxwell-Boltzmann distribution in blue dotted line, with $kT_e = 250$ keV. It is not possible to fit the whole electron spectrum with any single population of Maxwell-Boltzmann distribution.

The deviation of the higher energy component was attempted to be fitted by a single power-law distribution. For example, the red broken line represents the power-law distribution $d^2N/dEdS \propto E^{-1.535}$. Although it fits well within the range of 1 MeV$< E_e <$ 2 MeV, there is an extra cutoff for higher energy range.

In the theoretical study by Werner[53], relativistic magnetic reconnection produces a high-energy spectrum that can empirically be represented

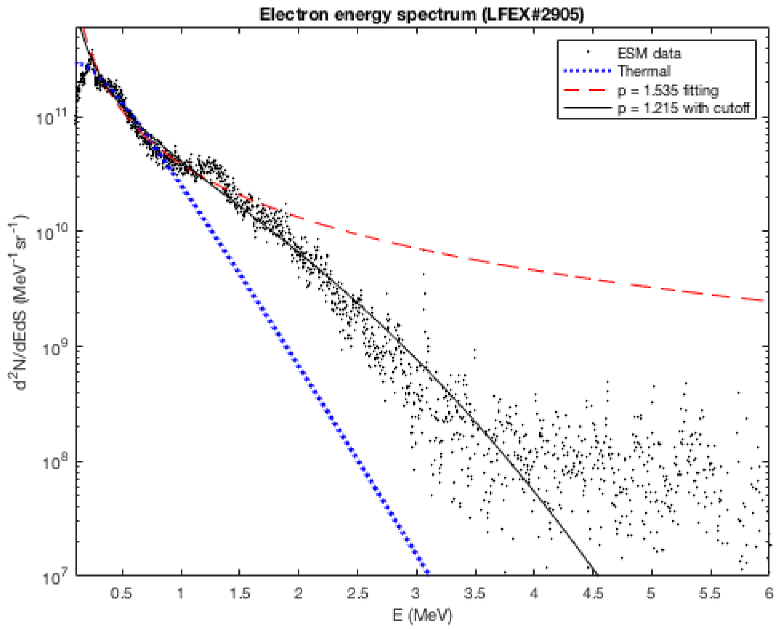

FIGURE 6.2: Electron energy spectrum in reconnection outflow jet measured by electron spectrometer, with the fitting of different distributions. Blue dotted line is the Maxwell-Boltzmann distribution ($kT_e = 250$ keV). The red broken line is power-law distribution ($p = 1.535$) fitted within the range of $1 < E_e < 2$ MeV, the lowest energy range which deviated from the thermal component. Black solid line is fitting of power-law with super-exponential cutoff included ($p = 1.215, E_{c2} = 1.742$).

by a combination of a power law, exponential cutoff, and super-exponential cutoff. Here a similar form is adopted:

$$f(E) \propto E^{-p} \exp(-E/E_{c1} - E^2/E_{c2}^2) \tag{6.1}$$

where here the γ is replaced by E.

Fitting of the experimental data was performed by the Curve Fitting Toolbox of MATLAB. Fitting range is $E_e > 300$ keV. During the fitting process, the value of E_{c1} was always too large and uncertain to measure, which is consistent with the work in [53]. The fitting process is therefore switched to the form that the $-E/E_{c1}$ term is omitted since it is negligible when E_{c1} is sufficiently large. As the result, the best fit was $p = 1.215$ and $E_{c2} = 1.742$, which is plotted in Figure 6.2 as black solid line.

Although the study in [53] focused on pair plasmas, it is worth to look at the physical meaning of what this best fit result corresponds to. The divergence of fitting and omission of E_{c1} was the case of small systems in Werner's work, which is also consistent with the situation in this experiment. It is because the system scale, if comparable to the micro-coil length, is only about 10^2 times of the electron nominal Lamour radius $\rho_0 = m_e c^2/eB$ (0.8 μm for $B = 2.1$ kT).

In the simulations on the pair plasmas, $\gamma_{c2} \sim 0.1L/\rho_0$ where L is the system size. From the ultrarelativistic limit $\gamma \approx 0.51E_e$, this could be further approximated as $E_{c2} \sim 0.051\rho_0$. From this relation, $E_{c2} = 1.742$ gives $L = 27.3$ μm, which is comparable to the length of the micro-coil target. It comes out that the empirical formula from numerical simulations on pair plasma might also valid in electron-ion plasma when the electron magnetization is considered.

The proton energy spectrum is plotted together with power-law fitting in Figure 6.3. The lower limit of detection for Thomson parabola spectrometer is 6 MeV, so only the high-energy non-thermal component could be measured. Blue dotted line indicated the fitting on the majority of the population, which is a power-law distribution with $p = 3.013$. This distribution is not hard as the non-thermal component in the electron energy spectrum, which is consistent with the Melzani's work [55]. For the cutoff-like population in $E_p > 14$ MeV, power-law with $p = 17.98$ best fits the spectral slope. Nevertheless, this is an extremely steep distribution.

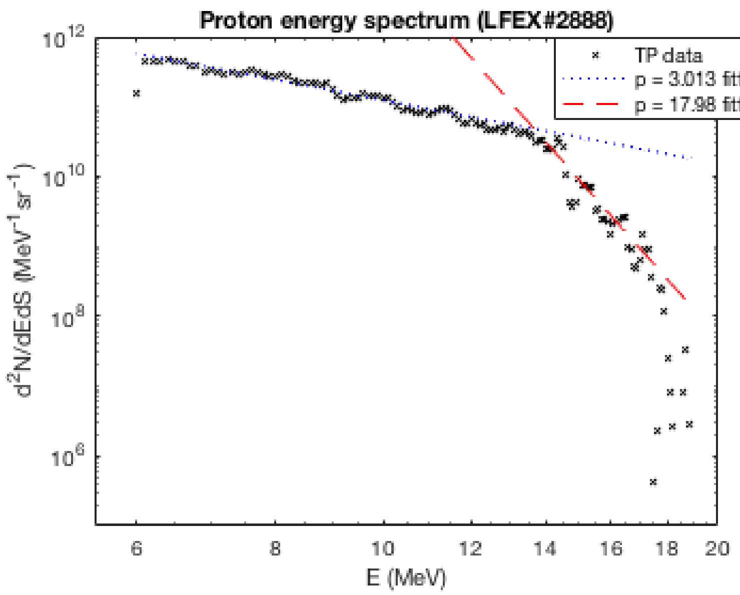

FIGURE 6.3: Proton energy spectrum in reconnection outflow jet measured by electron spectrometer, with the fitting of different distributions. Blue dotted line indicated the power-law fitting with $p = 3.013$, which is the majority of the population. Above 14 MeV, a cutoff like population is observed, which is fitted by a red broken line which is power-law fitting with $p = 17.98$, which is an extremely steep distribution.

6.3 Connection with Astrophysics: Magnetic Reconnection in Accretion Disk Black Hole System

The magnetic reconnection studied in this experiment is in electron-ion plasma, with magnetization in the semi-relativistic regime. Some examples of astrophysical plasmas that may perform magnetic reconnection are listed with the plasma produced in this work, in Table 6.1.

TABLE 6.1: Physical parameters in various environments, including the laser experiment in this work and potential candidates for astronomical plasma with the magnetic reconnection process. The relativistic Alfvén velocity $v_A/c = [\sigma/(1+\sigma)]^{-1/2}$ is also shown.

Magnetic reconnection plasma	B_0 (T)	$n_e(\mathrm{m}^{-3})$	T_e(K)	σ_e^{hot}	v_A/c
Laser-driven micro-coil	2.1×10^3	$10^{23}-10^{24}$	10^9-10^{10}	$20-100$	$0.22-0.58$
Cygnus X-1 accretion disk corona[75]	10^3	5×10^{24}	10^9	130	0.3
Microquasar coronae[55, 76]	10^1-10^3	$10^{19}-10^{22}$	10^9	$10^{-1}-10^5$	$0.003-1$
GRB jet[55, 77]	7×10^4	10^{16}	10^8	5×10^{12}	0.9

Cygnus X-1 is one specific example of black hole binary systems, which is relatively more understood. Emission of Cygnus X-1 was observed by different telescopes, so that a wide photon emission spectrum was obtained, from 10^{-6} to 10^{12} eV[78].

To explain the high energy component ($> 10^{11}$) of the photon emission spectrum, Zdziarski's work showed that a population of "hard" ($p < 2$) power-law electron spectrum is necessary to be in the astrophysical jets accelerated from the Cygnus X-1, supplied by any arbitrary acceleration mechanism. For instance, one would consider the possibility of magnetic reconnection, which is an efficient energy conversion process that is considered happening in such astronomical objects[79], as well as the ability to accelerate electrons into a power-law population in relativistic magnetic reconnection[54].

However, as Table 6.1 showed, magnetization σ_e in Cygnus X-1 accretion disk corona is about 130, lies in the semi-relativistic regime. It is not trivial that whether the electrons are still accelerated into such a hard power-law population, even the ions are not relativistically magnetized. Then, recent numerical works have shown that power-law could be built in the electron spectrum in a semi-relativistic regime[55, 56], but several limitations such as the ability to perform simulations in real ion-electron mass ratio still exist in these studies.

From Table 6.1, one could see that the micro-coil plasma and Cygnus X-1 accretion disk corona share many comparable physical parameters, including the magnetic field strength, electron density, and electron temperature. As a result, magnetization and Alfv́en velocity in these plasmas are also similar. In this work, the experimental result showed that the electron spectrum with power-law in $p = 1.215$, sufficiently hard, is accelerated by magnetic reconnection in the plasma parameter very close to that of Cygnus X-1 accretion disk corona.

As an astrophysical outlook, this should be an important experimental verification, showed that the environment in accretion disk black hole systems is possible to perform magnetic reconnection, as the source of energetic electron populations to power their high energy photon emission.

Chapter 7

Summary

This work is an experimental study on magnetic reconnection generated by intense laser irradiation on the micro-coil target. As the first step, magnetic field strength involved in the magnetic reconnection is experimentally characterized. Because of the 10^3 T order magnetic field strength and its extremely rapid ($\sim 10^{-12}$ s) rise-up time scale, the characterization of the magnetic field itself is not an easy task. Before getting into the magnetic reconnection experiment, efforts are made on the development of proton deflectometry, as an applicable magnetic field characterization method in such extreme conditions.

An important aspect of the development is to demonstrate the capability of proton deflectometry as a characterization of the magnetic field up to kilotesla order. A laser experiment was performed at ILE to measure the magnetic field strength generated by intense laser irradiated capacitor-coil target, which has a known current structure but unknown current amplitude. For the capacitor-coil target, a typical measurement method is available, by measuring the weaker magnetic field at a distant point using a differential magnetic probe coil and estimate the strongest magnetic field by extrapolation. Under the similar experimental condition, proton deflectometry measurement was performed, by directly passing a beam of probing protons (with energy in MeV order) through the region with the strongest magnetic field. The proton beam is deflected by the Lorentz force of the magnetic field and produced specific patterns in their momentum distribution, which was experimentally recorded by the RCF stack in this work.

As the result, the typical method estimated a peak magnetic field amplitude of 470 T, while the proton deflectometry estimated a magnetic field of 620 T at similar timing, with a larger ($\times 1.63$) laser energy irradiating on the capacitor-coil target because of the energy fluctuation. With this difference considered, the two results showed quite good consistency and therefore showed the capability of proton deflectometry on direct measurement of the kilotesla order magnetic field.

After that, an experiment on magnetic reconnection was performed at LFEX laser facility in ILE, by laser irradiation on micro-coil target. By modification of laser irradiation scheme, two opposite directions of current flowed inside a single target at the same time and created a magnetic field configuration for magnetic reconnection. Proton deflectometry measurement was performed to obtain the magnetic field strength in the reconnection, which directly relates to the degree of particle magnetization during the physical processes. By comparison between experimental and simulation reproduced proton deflection pattern, the magnetic field strength was determined 2.1 kT and the electron magnetization was $\sigma_e \sim 100$. This value of electron magnetization corresponds to the semi-relativistic regime of magnetic reconnection, where electrons were relativistic magnetized but not for ions.

Particle acceleration from semi-relativistic magnetic reconnection was then experimentally observed in this work. From the two sides of the microcoil target, which was the expected reconnection outflow directions, a pair of outflow jets in symmetric spatial patterns were detected by RCF stacks. Then, the electron and proton energy spectra were measured by spectrometers. Non-thermal populations were recognized in both spectra, which can be described by power-law distribution, one kind of energy distribution being predicted as the product of relativistic magnetic reconnection. Power-law distribution of electron high-energy component was hard ($p \sim 1.2$), while the distribution found in protons was not hard as electrons ($p \sim 3$). This is predicted by numerical simulations, but not yet verified experimentally from laboratory plasmas.

As an astrophysical outlook of this work, many of the physical parameters in this work is directly comparable to the accretion disk of black hole binary systems, which is currently impossible to access directly. In Cygnus X-1, an example of an accreting black hole binary system, its high-energy photon emission is predicted to be powered by hard ($p < 2$) power-law electron populations in its ejecting jets. The result of this work shows the possibility of magnetic reconnection in a similar physical condition that could produce such electron populations.

As presented in this work, by studying laboratory plasma that reproducing a similar physical environment as astronomical plasma, future studies on those astronomical objects could be explored also from the experiment in laboratories, but not solely on numerical or theoretical studies.

Appendix A

RCF Stack Configuration

There are two RCF stack configurations used in the capacitor-coil experiment: One for proton beam characterization and another one for proton deflectometry of magnetic field measurement. Also, there are two RCF stack configurations used in the magnetic reconnection experiment: One for proton deflectometry and another one for reconnection jet spatial distribution measurement.

A.1 RCF stack for proton beam characterization in capacitor-coil experiment

Design of this RCF stack is to prepare for an almost unknown proton beam spectrum, because of the lack of similar experiences.

The RCF layer number, filter materials and thickness, RCF type and corresponding proton energy (in MeV) are listed in Table A.1 and A.2.

For protons below 18 MeV, the proton flux is predicted to be very high and only HD-V2 is used. From 18 to 28 MeV, HD-V2 and MD-V3 are used in groups with a filter between groups. Above 28 MeV, HD-V2, MD-V3 and EBT3 are all used as groups with metal filter between groups. For above 40 MeV, aluminum filter is not enough in stopping power, so copper filters are used instead.

A.2 RCF stack for proton deflectometry in capacitor-coil experiment

By the proton beam pattern using RCF stack in previous section, the design of RCF stack for proton deflectometry is modified according to the proton characterization result.

The RCF layer number, filter materials and thickness, RCF type and corresponding proton energy (in MeV) are listed in Table A.3.

The concept of design is to ignore the low energy protons which even completely saturates the HD-V2 film, and to increase the energy resolution in the useful energy range between 18 and 29 MeV with HD-V2 and

TABLE A.1: RCF stack configuration for proton beam characterization (1/2)

RCF Layer #	Layer	Energy (MeV)
	300 μm Al	
1	HD-V2	6.6
	300 μm Al	
2	HD-V2	10.4
	100 μm Al	
3	HD-V2	11.9
	100 μm Al	
4	HD-V2	13.2
	100 μm Al	
5	HD-V2	14.4
	200 μm Al	
6	HD-V2	16.2
	200 μm Al	
7	HD-V2	17.9
	100 μm Al	
8	HD-V2	18.8
9	MD-V3	19.6
	100 μm Al	
10	HD-V2	20.6
11	MD-V3	21.4
	200 μm Al	
12	HD-V2	22.7
13	MD-V3	23.5
	200 μm Al	
14	HD-V2	24.8
15	MD-V3	25.4
	200 μm Al	
16	HD-V2	26.7
17	MD-V3	27.3
	200 μm Al	
18	HD-V2	28.4
19	MD-V3	29.0
20	EBT3	29.7

TABLE A.2: RCF stack configuration for proton beam characterization (2/2)

RCF Layer #	Layer	Energy (MeV)
	300 μm Al	
21	HD-V2	31.1
22	MD-V3	31.7
23	EBT3	32.5
	300 μm Al	
24	HD-V2	33.8
25	MD-V3	34.3
26	EBT3	34.9
	300 μm Al	
27	HD-V2	36.2
28	MD-V3	36.8
29	EBT3	37.4
	300 μm Al	
30	HD-V2	38.5
31	MD-V3	39.0
32	EBT3	39.6
	330 μm Cu	
33	HD-V2	42.2
34	MD-V3	42.9
35	EBT3	43.3
	300 μm Al	
36	EBT3	46.3

MD-V3. The EBT3 is not suitable for this measurement because of the large background signal. Since the maximum energy is found to be 34.3 MeV, energy up to 40 MeV is covered by this stack.

A.3 RCF stack for proton deflectometry in magnetic reconnection experiment

Design of this RCF stack is to prepare for an almost unknown proton beam spectrum, with a significantly lower maximum energy. HD-V2 and EBT3 are mixed in an alternative way to cover a wide range of possible proton flux.

The RCF layer number, filter materials and thickness, RCF type and corresponding proton energy (in MeV) are listed in Table A.4.

A.4 RCF stack for outflow jet measurement in magnetic reconnection experiment

The purpose of this RCF stack is to estimate the maximum energy of outflow jet from magnetic reconnection, as well as measuring the spatial distribution of outflow jet. Therefore, HD-V2 layers are placed in front of EBT3 layers.

The RCF layer number, filter materials and thickness, RCF type and corresponding proton energy (in MeV) are listed in Table A.5.

TABLE A.3: RCF stack configuration for proton deflectometry

RCF Layer #	Layer	Energy (MeV)
	900 μm Al	
1	HD-V2	12.3
	300 μm Al	
2	HD-V2	15.1
	300 μm Al	
3	HD-V2	17.4
4	HD-V2	17.8
5	MD-V3	18.7
6	HD-V2	19.2
7	MD-V3	20.0
8	HD-V2	20.4
9	MD-V3	21.1
10	HD-V2	21.5
11	MD-V3	22.3
12	HD-V2	22.7
13	MD-V3	23.4
14	HD-V2	23.8
15	MD-V3	24.5
16	HD-V2	24.9
17	MD-V3	25.5
18	HD-V2	25.9
19	MD-V3	26.6
20	HD-V2	26.8
21	MD-V3	27.5
22	HD-V2	27.8
23	MD-V3	28.5
	300μm Al	
24	HD-V2	30.0
25	MD-V3	30.6
	300μm Al	
26	HD-V2	32.0
27	MD-V3	32.5
	300μm Al	
28	HD-V2	33.9
29	MD-V3	34.4
	300μm Al	
30	HD-V2	35.7
31	MD-V3	36.2
	300μm Al	
32	HD-V2	37.5
33	MD-V3	37.9
	300μm Al	
34	HD-V2	39.2
35	MD-V3	39.6

TABLE A.4: RCF stack configuration for proton deflectometry in magnetic reconnection experiment

RCF Layer #	Layer	Energy (MeV)
	10 μm Al	
1	HD-V2	1.5
2	EBT3	4.9
3	EBT3	7.4
4	HD-V2	8.5
5	EBT3	9.9
6	HD-V2	10.8
7	EBT3	12.0

TABLE A.5: RCF stack configuration for outflow jet measurement in magnetic reconnection experiment

RCF Layer #	Layer	Energy (MeV)
	10 μm Al	
1	HD-V2	1.5
2	HD-V2	3.4
3	HD-V2	4.7
4	HD-V2	5.7
5	HD-V2	6.7
6	EBT3	8.4
7	EBT3	10.2
8	EBT3	11.7
9	EBT3	13.1
10	EBT3	14.3
11	EBT3	15.5
12	EBT3	16.6
13	EBT3	17.7
14	EBT3	18.7
15	EBT3	19.6
16	EBT3	20.5
17	EBT3	21.4
18	EBT3	22.3
19	EBT3	23.1
20	EBT3	23.9

Appendix B

RADIA code for magnetic field modeling in this work

In this section, the source codes for current modeling by RADIA are provided in Mathematica format.

B.1 Mathematica code for capacitor-coil modeling

```
<< Radia`;

ct = 0.05;  (*coil thickness in mm*)
cra = 0.25; (*coil radius in mm*)

crb = 0.25;
ww = 0.05; (*wire width in mm*)
wt = 0.05; (*wire thickness in mm*)

ic = -100*^3; (*current in A*)
op = 0.3;    (*coil open in mm*)
opaa = ArcSin[op/2/cra];  (*half open angle*)
opab = ArcSin[op/2/crb];
sla = 1.464;(*length of straight part in mm*)
slb = 1.464;
slf = 0.2;(*length of the foot in mm*)
dc = 0.5; (*distance between two coil in mm*)
dd = 0.68; (*distance between the disk in mm*)

c2 = {1, 1, 0}; c1 = {0, 1, 1}; thcn = 0.001;

jca = ic/ct^2; (* Current Densities in A/mm^2 in coil*)
jcb = jca;
jwa = ic/(wt*ww); (* Current Densities in A/mm^2 in wire*)
jwb = jwa;
```

```
x1a = -op/2;
x2a = op/2;
x3a = 0;
y0a = -cra*Cos[opaa];
y1a = y0a - sla/2;
y2a = y0a - (sla - slf)/2;
y3a = 0;
z1a = z2a = z3a = dc/2;

x1b = -op/2;
x2b = op/2;
x3b = 0;
y0b = -crb*Cos[opab];
y1b = y0b - slb/2;
y2b = y0b - (slb - slf)/2;
y3b = 0;
z1b = z2b = z3b = dc/2;

wx1 = wx2 = ww;
wy1a = sla;
wy1b = slb;
wy2a = sla - slf;
wy2b = slb - slf;
wz1 = wz2 = wt;

rmina = cra - ct/2;
rminb = crb - ct/2;
rmaxa = cra + ct/2;
rmaxb = crb + ct/2;
h = ct;
nseg = 200;

Rt1a = radObjRecCur[{x1a, y1a, z1a}, {wx1, wy1a, wz1}, {0, jwa, 0}];
radObjDrwAtr[Rt1a, c1, thcn];
Rt2a = radObjRecCur[{x2a, y2a, z2a}, {wx2, wy2a, wz2}, {0, -jwa, 0}];
radObjDrwAtr[Rt2a, c1, thcn];
Rt3a = radObjArcCur[{x3a, y3a, z3a}, {rmina, rmaxa}, {-1/2 Pi + opaa,
    3/2 Pi - opaa}, h, nseg, -jca];
radObjDrwAtr[Rt3a, c2, thcn];

Rt1b = radObjRecCur[{x1b, y1b, z1b}, {wx1, wy1b, wz1}, {0, -jwb, 0}];
```

```
radObjDrwAtr[Rt1b, c1, thcn];
Rt2b = radObjRecCur[{x2b, y2b, z2b}, {wx2, wy2b, wz2}, {0, jwb, 0}];
radObjDrwAtr[Rt2b, c1, thcn];
Rt3b = radObjArcCur[{x3b, y3b, z3b}, {rminb, rmaxb}, {-1/2 Pi + opab,
    3/2 Pi - opab}, h, nseg, jcb];
radObjDrwAtr[Rt3b, c2, thcn];

radTrfOrnt[Rt1b, radTrfRot[{0, 0, 0}, {0, 1, 0}, Pi]];
radTrfOrnt[Rt1b, radTrfRot[{0, 0, 0}, {0, 0, 1}, Pi]];
radTrfOrnt[Rt2b, radTrfRot[{0, 0, 0}, {0, 1, 0}, Pi]];
radTrfOrnt[Rt2b, radTrfRot[{0, 0, 0}, {0, 0, 1}, Pi]];
radTrfOrnt[Rt3b, radTrfRot[{0, 0, 0}, {0, 1, 0}, Pi]];
radTrfOrnt[Rt3b, radTrfRot[{0, 0, 0}, {0, 0, 1}, Pi]];

Coil = radObjCnt[{Rt1a, Rt1b, Rt2a, Rt2b, Rt3a, Rt3b}];
```

B.2 Mathematica code for micro-coil modeling

```
<< Radia`;

snailw = 0.5;   (*snail width in mm*)
snailr1 = 0.15;  (*snail radius in mm*)
snailr2 = 0.1;  (*snail radius in mm*)
snaili0 = 1*^5; (*max current in A*)
snaili1 = -0.66;
snailt = 0.01;
sheeti = snaili0*0.2;
thetai0 = 45 Degree;
thetai1 = 360 Degree;
sheetang = thetai0 + (thetai1 - thetai0)/(1 - snaili1);

c2 = {1, 1, 0}; c1 = {0, 1, 1}; thcn = 0.001;

snailj = snaili0/(snailt*snailw);
nseg = 10;
snailsegj[n_] :=
  snaili0*(1 + (snaili1 -
         1)*(n - thetai0)/(thetai1 - thetai0))/(snailt*snailw);
snailsegr[n_] := snailr1 + (snailr2 - snailr1)*(n/(360 Degree));

snailsegnum = 200;
snailsegdeg = (thetai1 - thetai0)/snailsegnum;
```

```
Snail = Table[0, {snailsegnum}];

For[i = 1, i <= snailsegnum, i++,
 Snail[[i]] =
   radObjArcCur[{0, 0,
     0}, {snailsegr[thetai0 + (i - 0.5)*snailsegdeg] - 0.5*snailt,
     snailsegr[thetai0 + (i - 0.5)*snailsegdeg] +
      0.5*snailt}, {thetai0 + (i - 1)*snailsegdeg,
     thetai0 + i*snailsegdeg}, snailw, nseg,
    snailsegj[thetai0 + (i - 0.5)*snailsegdeg], "man", "z"];
 ]

sheetj = sheeti/(0.01*snailw);
Sheet = radObjRecCur[{0, 0, 0}, {2.0*snailr2, 0.01, snailw}, {sheetj,
    0, 0}];
radTrfOrnt[Sheet,
  radTrfRot[{0, 0, 0}, {0, 0, 1}, -(1.5*Pi - sheetang)]];

SnailObj = radObjCnt[Snail];
radTrfOrnt[SnailObj, radTrfRot[{0, 0, 0}, {0, 0, 1}, -90 Degree]];

Whole = radObjCnt[{SnailObj, Sheet}];
radTrfOrnt[Whole, radTrfRot[{0, 0, 0}, {0, 0, 1}, 180 Degree]];
radTrfOrnt[Whole, radTrfRot[{0, 0, 0}, {0, 1, 0}, 180 Degree]];
```

Bibliography

1. Sweet, P. A. *14. The neutral point theory of solar flares* in *Symposium-International Astronomical Union* **6** (1958), 123–134.
2. Kulsrud, R. M. Magnetic reconnection in a magnetohydrodynamic plasma. *Physics of Plasmas* **5,** 1599–1606 (1998).
3. Biskamp, D. Magnetic reconnection in plasmas. *Astrophysics and Space Science* **242,** 165–207 (1996).
4. Drenkhahn, G & Spruit, H. Efficient acceleration and radiation in Poynting flux powered GRB outflows. *Astronomy & Astrophysics* **391,** 1141–1153 (2002).
5. Priest, E. & Forbes, T. Magnetic Reconnection: MHD Theory and Applications, Cambridge Univ. *Prees, Cambridge* (2000).
6. Taylor, J. Relaxation and magnetic reconnection in plasmas. *Reviews of Modern Physics* **58,** 741 (1986).
7. Yamada, M. Review of controlled laboratory experiments on physics of magnetic reconnection. *Journal of Geophysical Research: Space Physics* **104,** 14529–14541 (1999).
8. Ono, Y, Morita, A, Katsurai, M & Yamada, M. Experimental investigation of three-dimensional magnetic reconnection by use of two colliding spheromaks. *Physics of Fluids B: Plasma Physics* **5,** 3691–3701 (1993).
9. Ono, Y., Yamada, M., Akao, T., Tajima, T. & Matsumoto, R. Ion acceleration and direct ion heating in three-component magnetic reconnection. *Physical review letters* **76,** 3328 (1996).
10. Yamada, M. *et al.* Study of driven magnetic reconnection in a laboratory plasma. *Physics of Plasmas* **4,** 1936–1944 (1997).
11. Egedal, J. *et al.* Laboratory observations of spontaneous magnetic reconnection. *Physical review letters* **98,** 015003 (2007).
12. Olson, J *et al.* Experimental demonstration of the collisionless plasmoid instability below the ion kinetic scale during magnetic reconnection. *Physical review letters* **116,** 255001 (2016).
13. Zhong, J. *et al.* Modelling loop-top X-ray source and reconnection outflows in solar flares with intense lasers. *Nature Physics* **6,** 984–987 (2010).
14. Daido, H. *et al.* Generation of a Strong Magnetic Field by an Intense CO2 Laser Pulse. *Physical Review Letters* **56,** 846–851 (1986).

15. Pei, X. X. *et al.* Magnetic reconnection driven by Gekko XII lasers with a Helmholtz capacitor-coil target. *Physics of Plasmas* **23.** doi:10.1063/1.4944928 (2016).

16. <http://www.ile.osaka-u.ac.jp/jp/overview/facilities/gxii.html>.

17. <http://www.ile.osaka-u.ac.jp/jp/overview/facilities/lfex.html>.

18. <http://www.ashland.com/products/gafchromic-radiotherapy-films>.

19. Forslund, D., Kindel, J. & Lee, K. Theory of Hot-Electron Spectra at High Laser Intensity. *Physical Review Letters* **39,** 284–288 (1977).

20. Yates, M. A., Van Hulsteyn, D. B., Rutkowski, H., Kyrala, G. & Brackbill, J. U. Experimental evidence for self-generated magnetic fields and remote energy deposition in laser-irradiated targets. *Physical Review Letters* **49,** 1702–1704 (1982).

21. Terai, K. *et al.* Lateral transport of hot electrons on a spherical target by 10.6-μm CO2 laser irradiation. *Applied Physics Letters* **46,** 355 (1985).

22. Jarrott, L. C. *et al.* Visualizing fast electron energy transport into laser-compressed high-density fast-ignition targets. *Nature Physics* **12,** 499–504 (2016).

23. Santos, J. J. *et al.* Laser-driven platform for generation and characterization of strong quasi-static magnetic fields. *New Journal of Physics* **17,** 083051 (2015).

24. Korneev, P., D'Humières, E. & Tikhonchuk, V. Gigagauss-scale quasistatic magnetic field generation in a snail-shaped target. *Physical Review E* **91,** 043107 (2015).

25. Korneev, P. *et al.* Laser electron acceleration on curved surfaces. *arXiv preprint arXiv:1711.00971* (2017).

26. Yamada, M., Kulsrud, R. & Ji, H. Magnetic reconnection. *Reviews of Modern Physics* **82,** 603 (2010).

27. Hoyle, F. Magnetic storms and aurorae. *Some Recent Researches in Solar Physics,* 92–102 (1949).

28. Giovanelli, R. A theory of chromospheric flares. *Nature* **158,** 81 (1946).

29. Cohen, R. S., Spitzer Jr, L. & Routly, P. M. The electrical conductivity of an ionized gas. *Physical Review* **80,** 230 (1950).

30. Spitzer Jr, L. & Härm, R. Transport phenomena in a completely ionized gas. *Physical Review* **89,** 977 (1953).

31. Gingerich, O. & de Jager, C. in *The Structure of the Quiet Photosphere and the Low Chromosphere* 5–25 (Springer, 1968).

32. Hagenaar, H. J. Ephemeral regions on a sequence of full-disk Michelson Doppler Imager magnetograms. *The Astrophysical Journal* **555,** 448 (2001).

33. Parker, E. N. Sweet's mechanism for merging magnetic fields in conducting fluids. *Journal of Geophysical Research* **62,** 509–520 (1957).

34. Petschek, H. E. Magnetic field annihilation. *NASA Special Publication* **50,** 425 (1964).

35. Ugai, M. & Tsuda, T. Magnetic field-line reconnexion by localized enhancement of resistivity: Part 1. Evolution in a compressible MHD fluid. *Journal of Plasma Physics* **17,** 337–356 (1977).

36. Sato, T. & Hayashi, T. Externally driven magnetic reconnection and a powerful magnetic energy converter. *The Physics of Fluids* **22,** 1189–1202 (1979).

37. Priest, E. & Forbes, T. New models for fast steady state magnetic reconnection. *Journal of Geophysical Research: Space Physics* **91,** 5579–5588 (1986).

38. Biskamp, D. Magnetic reconnection via current sheets. *The Physics of fluids* **29,** 1520–1531 (1986).

39. Birn, J *et al.* Geospace Environmental Modeling (GEM) magnetic reconnection challenge. *Journal of Geophysical Research: Space Physics* **106,** 3715–3719 (2001).

40. Kulsrud, R. M. Magnetic reconnection: Sweet-parker versus petschek. *Earth, Planets and Space* **53,** 417–422 (2001).

41. Uzdensky, D. A. Petschek-like reconnection with current-driven anomalous resistivity and its application to solar flares. *The Astrophysical Journal* **587,** 450 (2003).

42. Lazarian, A & Vishniac, E. T. Reconnection in a weakly stochastic field. *The Astrophysical Journal* **517,** 700 (1999).

43. Kuritsyn, A, Ji, H., Gerhardt, S., Ren, Y & Yamada, M. Effects of global boundary and local collisionality on magnetic reconnection in a laboratory plasma. *Geophysical Research Letters* **34** (2007).

44. Mozer, F., Bale, S. & Phan, T. Evidence of diffusion regions at a subsolar magnetopause crossing. *Physical review letters* **89,** 015002 (2002).

45. Pritchett, P. Geospace Environment Modeling magnetic reconnection challenge: Simulations with a full particle electromagnetic code. *Journal of Geophysical Research: Space Physics* **106,** 3783–3798 (2001).

46. Coroniti, F. Magnetically striped relativistic magnetohydrodynamic winds-The Crab Nebula revisited. *The Astrophysical Journal* **349,** 538–545 (1990).
47. Lyubarsky, Y & Kirk, J. Reconnection in a striped pulsar wind. *The Astrophysical Journal* **547,** 437 (2001).
48. Giannios, D. & Spruit, H. C. The role of kink instability in Poynting-flux dominated jets. *Astronomy & Astrophysics* **450,** 887–898 (2006).
49. Nodes, C., Birk, G. T., Lesch, H. & Schopper, R. Particle acceleration in three-dimensional tearing configurations. *Physics of Plasmas* **10,** 835–844 (2003).
50. Onofri, M., Isliker, H. & Vlahos, L. Stochastic acceleration in turbulent electric fields generated by 3D reconnection. *Physical Review Letters* **96,** 151102 (2006).
51. Sironi, L. & Spitkovsky, A. Relativistic reconnection: an efficient source of non-thermal particles. *The Astrophysical Journal Letters* **783,** L21 (2014).
52. Guo, F., Liu, Y.-H., Daughton, W. & Li, H. Particle acceleration and plasma dynamics during magnetic reconnection in the magnetically dominated regime. *The Astrophysical Journal* **806,** 167 (2015).
53. Werner, G., Uzdensky, D., Cerutti, B, Nalewajko, K & Begelman, M. The extent of power-law energy spectra in collisionless relativistic magnetic reconnection in pair plasmas. *The Astrophysical Journal Letters* **816,** L8 (2015).
54. Guo, F. *et al.* Efficient production of high-energy nonthermal particles during magnetic reconnection in a magnetically dominated ion–electron plasma. *The Astrophysical Journal Letters* **818,** L9 (2016).
55. Melzani, M., Walder, R., Folini, D., Winisdoerffer, C. & Favre, J. M. The energetics of relativistic magnetic reconnection: ion-electron repartition and particle distribution hardness. *Astronomy & Astrophysics* **570,** A112 (2014).
56. Werner, G., Uzdensky, D., Begelman, M., Cerutti, B & Nalewajko, K. Non-thermal particle acceleration in collisionless relativistic electron–proton reconnection. *Monthly Notices of the Royal Astronomical Society* **473,** 4840–4861 (2017).
57. Piel, A. *Plasma Physics: An Introduction to Laboratory, Spac, and Fusion Plasmas* chap. 6.6.2 (Springer Berlin Heidelberg, 2010).
58. Fujioka, S. *et al.* Kilotesla Magnetic Field due to a Capacitor-Coil Target Driven by High Power Laser. *Scientific Reports* **3,** 1–7 (2013).
59. Cobble, J. A., Johnson, R. P., Cowan, T. E., Renard-Le Galloudec, N. & Allen, M. High resolution laser-driven proton radiography. *Journal of Applied Physics* **92,** 1775–1779 (2002).

60. Mackinnon, A. J. *et al.* Proton Radiography of a Laser-Driven Implosion. *Physical Review Letters* **97,** 045001 (2006).

61. Li, C. K. *et al.* Measuring E and B fields in laser-produced plasmas with monoenergetic proton radiography. *Physical Review Letters* **97,** 3–6 (2006).

62. Li, C. K. *et al.* Observations of electromagnetic fields and plasma flow in hohlraums with proton radiography. *Physical Review Letters* **102,** 1–4 (2009).

63. Li, C. K. *et al.* Proton radiography of dynamic electric and magnetic fields in laser-produced high-energy-density plasmas. *Physics of Plasmas* **16** (2009).

64. Wilks, S. C. *et al.* Energetic proton generation in ultra-intense laser-solid interactions. *Physics of Plasmas* **8,** 542. ISSN: 1070664X (2001).

65. Passoni, M., Bertagna, L. & Zani, A. Target normal sheath acceleration: theory, comparison with experiments and future perspectives. *New Journal of Physics* **12,** 045012 (2010).

66. Zylstra, a. B. *et al.* Using high-intensity laser-generated energetic protons to radiograph directly driven implosions. *Review of Scientific Instruments* **83** (2012).

67. Law, K. F. F. *et al.* Direct measurement of kilo-tesla level magnetic field generated with laser-driven capacitor-coil target by proton deflectometry. *Applied Physics Letters* **108,** 9–14 (2016).

68. <http://www.esrf.eu/Accelerators/Groups/InsertionDevices/Software/Radia>.

69. Arber, T. *et al.* Contemporary particle-in-cell approach to laser-plasma modelling. *Plasma Physics and Controlled Fusion* **57,** 113001 (2015).

70. Zenitani, S., Hesse, M., Klimas, A. & Kuznetsova, M. New measure of the dissipation region in collisionless magnetic reconnection. *Physical review letters* **106,** 195003 (2011).

71. Xu, Z *et al.* Characterization of magnetic reconnection in the high-energy-density regime. *Physical Review E* **93,** 033206 (2016).

72. Tosaki, S *et al.* Evaluation of laser-driven ion energies for fusion fast-ignition research. *Progress of Theoretical and Experimental Physics* **2017,** 103J01 (2017).

73. Fujioka, S. *et al.* Heating efficiency evaluation with mimicking plasma conditions of integrated fast-ignition experiment. *Physical Review E* **91,** 063102 (2015).

74. Pisarczyk, T *et al.* Magnetized plasma implosion in a snail target driven by a moderate-intensity laser pulse. *Scientific reports* **8,** 17895 (2018).

75. Del Santo, M., Malzac, J., Belmont, R., Bouchet, L. & De Cesare, G. The magnetic field in the X-ray corona of Cygnus X-1. *Monthly Notices of the Royal Astronomical Society* **430,** 209–220 (2013).

76. Reis, R. & Miller, J. On the size and location of the X-ray emitting coronae around black holes. *The Astrophysical Journal Letters* **769,** L7 (2013).

77. McKinney, J. C. & Uzdensky, D. A. A reconnection switch to trigger gamma-ray burst jet dissipation. *Monthly Notices of the Royal Astronomical Society* **419,** 573–607 (2011).

78. Zdziarski, A. A., Stawarz, L., Pjanka, P. & Sikora, M. Jet models for black hole binaries in the hard spectral state. *Monthly Notices of the Royal Astronomical Society* **440,** 2238–2254 (2014).

79. De Gouveia Dal Pino, E. M. *et al. Magnetic Reconnection on Jet-Accretion disk Systems* tech. rep. (SISSA, 2016).